Dissertation

学位請求論文

Ultra-high Strain Resolution Optical Fiber Sensors for Geophysical Applications

地球物理研究用超高歪分解能光ファイバセンサ

Supervisor: **Prof. Zuyuan He**

指導教員：何 祖源 特任教授

Submitted on December 5, 2011

平成 23 年 12 月 5 日提出

Department of Electrical Engineering and Information Systems

Graduate School of Engineering, The University of Tokyo

東京大学大学院工学系研究科電気系工学専攻

37 - 097111

Qingwen Liu

劉 慶文

Abstract

Geophysical research requires monitoring the earth's deformation continuously at locations as many as possible with nano-strain (nε) order resolution and large dynamic range in the static to low frequency domain. Currently sensors for this purpose include the borehole strain meter, extension meter, and free-space laser interferometers. Those types of sensors provide sufficient strain resolution; however, their large length of tens to hundreds of meters and high cost restrict the wide adoption of those sensors, especially in the deep underground. On the other hand, optical fiber strain sensors have the well-known advantages such as light weight, small size, low cost, ability of remote and multiplexed sensing, etc. They are very attractive for geophysical research if they can provide the required strain resolution. Although strain resolution even better than nε have been reported in dynamic strain sensing with optical fiber sensors, the resolution in the quasi-static frequency domain the resolution is limited to the order of micro-strain (με) for most of sensors. It is generally satisfactory for applications such as smart material and structure health monitoring. But it has to be improved by about 3 orders of magnitude for the sensors to be utilized in the geophysical applications.

The strain resolution is one of the most important parameters to evaluate the performance of strain sensors. It is defined as the smallest change in strain that produces a distinguished response in the measurement. The resolution of a sensor is limited by the random noise level in the system and by the ambient interference. Two factors relate to high resolution. First, the sensor must have high strain sensitivity, which is defined as the induced variation in the output of the sensor for a given change of strain. The other factor is to effectively suppress the random noise level and the effect of ambient

interference. This does not only involve choosing high precision instruments which will significantly increase the cost of the sensor; more importantly, the mechanism of the sensor has to been studied sufficiently to find the main noise sources and then suppress them by certain methods. At the beginning of this thesis, we theoretically analyzed the performance of a static strain optical fiber sensor interrogated by a tunable laser, and deduced the expression of the strain resolution for this type of sensors. Following on the analysis, a series of optical fiber sensors were developed with ultra-high strain resolution. Further attempt on multiplexed sensing is also presented in the later part of this thesis.

Optical fiber strain sensors have already achieved ultra-high resolution in dynamic strain sensing field; however, the strain sensing in the quasi-static domain is not so successful yet. Those facts are a direct consequence of an essential difference between the dynamic and static strain sensing. The dynamic sensing deals with the periodical strain signal, and thus it is self-referenced; but the static strain sensing measures arbitrary (usually slowly varying) signals, and an extra reference is required, which is usually a frequency-stabilized component or an additional sensor head identical to the strain sensor but free of strain. In our research, the proposed quasi-static strain sensors have two identical sensor heads. One is for strain sensing and the other is strain-free working as a reference for compensation of the fluctuation of both the laser source and the sensor heads. The key for ultra-high resolution static strain sensing credits to the precise measurement of the output difference between the two sensor heads. Two types of sensor heads are presented in this thesis, and different technologies are proposed for the interrogation of the sensor heads.

The structure of the thesis is stated below.

In chapter 2, we designed an ultra-high strain-resolution fiber Bragg grating (FBG) sensor which is interrogated by a narrow linewidth tunable laser. The sensor consists of a pair of FBGs for strain sensing and reference, respectively. The wavelength of the

laser source sweeps to obtain the spectra of FBGs. The difference in the Bragg wavelength of the FBGs is calculated utilizing a cross-correlation algorithm. The performance of the sensor is theoretically studied. First, the main noise sources in the sensor are discussed. Then, the expression of the resolution is deduced with a Gaussian-curve model for the FBG's spectrum. The theoretical prediction agrees well with numerical simulation, and is further verified by experimental results. With the expression, the guidelines to optimize this type of the sensor are revealed in detail, providing a firm base for the construction of practical nε resolution FBG sensors.

In chapter 3, we built a FBG strain sensor based on the analysis. With the sensor a wavelength resolution of 3.1 fm was obtained in laboratory without strain applied, corresponding to a static strain resolution down to 2.6 nε. This is the first demonstration that a nε-order static strain resolution is achied with a simple sensor configuration. With a variable strain applied by a piezo-stage, a strain resolution of 17.6 nε was demonstrated, which is mainly limited by the precision of the testing stage. Later, the sensor is put into field test to measure the crustal deformation induced by oceanic tide at Aburatsubo Bay, Japan, which is currently monitored by 38m-long extension-meters. Wavelength division multiplexing (WDM) technique is used for interrogation of two sets of FBG strain sensors. The deformation induced by oceanic tide is clearly recorded with resolution about 10 nε, and the strain staggers around earthquakes are also observed. Compared with the extension-meters, our FBG sensor has a comparable resolution with a much smaller size and lower cost, providing a powerful tool for geophysical measurements.

In chapter 4, we developed an optical fiber static strain sensor by using a pair of fiber Fabry-Perot interferometer (FFPI) sensor heads, to overcome the wavelength repeatability problem which limits further improvement on the resolution of FBG sensors. A frequency modulation (FM) technology is used to dither the laser frequency, and then a digitalized demodulation configuration is employed to extract the detuning

information between the laser source and the resonance frequency of the FFPIs. A cross-correlation algorithm is used to calculate the resonance difference from the extracted signals with high precision. An ultra-high static wavelength resolution corresponding to strain resolution down to 5.8 nε was demonstrated in experiment, with dynamic range large than 100 με. Together with the small laser sweeping range (5 pm) and the short measuring period, this research provides a high resolution, large dynamic, short measuring period and low cost strain sensor for the geophysical applications.

Then we invented a novel sideband interrogation technology to interrogate FFPI sensors for even higher strain resolution in chapter 5. This technology avoids the wavelength nonlinearity problem of the tunable laser during large-range sweeping in the typical FM configuration. A special designed radio frequency signal is used to drive an intensity modulator (IM) to generate a sideband. The sideband is used to interrogate the sensing FFPI, while the laser carrier is used to interrogate the reference FFPI with typical FM configuration. Experiment of static strain sensing is carried out using a tunable laser, and a cross-correlation algorithm is employed to calculate the resonance difference. With a sweeping rang of only 0.1 pm and measuring period of a few seconds, a standard deviation of measured resonance difference of 29 kHz was obtained, corresponding to a strain resolution of 0.3 nε. This is the first time that a sub-nε static strain resolution was demonstrated with optical fiber sensors. Real-time sensing is achieved by locking the laser carrier and sideband to the reference and sensing FFPIs, respectively. Furthermore, real-time sensing is achieved by locking the laser carrier and the sideband to the reference and the sensing FFPIs, respectively. With a specially designed radio frequency modulator to drive the IM, a strain resolution down to 0.05 nε is realized in real-time srain sensor, and the measuring rate is 7 Hz. With the ultra-high strain resolution and the ability of real-time sensing, the proposed sensor meets the strictest standard for geophysical research, especially, for earthquake measurements.

In chapter 6, we designed a multiplexing technology with identical FFPI sensor heads based on a dual-modulation configuration. The modulation method is presented after a thorough analysis on the FM modulation technique, and a modulator for the dual-modulation is designed using a commercially available differential quadrature phase shift keying (DQPSK) modulator. Numerical simulation results prove that, the strain and the position can be measured simultaneously in the multiplexed sensor with two identical FFPIs.

The last chapter concludes the research. The developed ultra-high strain resolution sensors are compared, and the direction for choosing suitable sensor is given.

Index

List of Figures

List of Tables

Chapter 1.

Introduction

1.1 Strain and strain sensor

1.1.1 Deformation and strain

Strain is a type of deformation of object. As shown in Fig. 1-1, for a line object with one end fixed, there are several types of deformation, such as torsion, bending and strain. The nominal strain of a material line element or fiber axially loaded is expressed as the change in length ΔL per unit of the original length L of the line element or fibers [1]. It is labeled as ε, anditt is positive if the material fibers are stretched or negative if they are compressed

$$\varepsilon = \frac{\Delta L}{L} = \frac{L' - L}{L}, \tag{1.1}$$

where L is the original length of the fiber, and L' is the final length of the fiber.

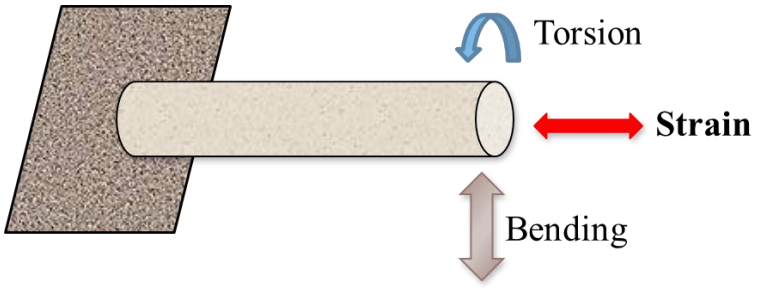

Fig. 1-1 Deformation and strain of a material body.

1.1.2 Strain sensor

Strain sensor is the device that can tell the value of strain. Several parameters are used to evaluate the performance of the strain sensor.

1.1.2.1 Resolution

Resolution is one of the most important parameter of the sensors. It is defined as the smallest distinguishable change in the underlying strain to the object that produces a response in the measurement. It is related to the precision, which is the degree to which repeated measurements under unchanged conditions show the same results.

The resolution is often confused with accuracy. Accuracy of a measurement system is the degree of closeness of measurements of a quantity to that quantity's actual (true) value. It is induced by systematic errors in the sensing system, and can sometimes be compensated for by means of some kinds of calibration strategy. The resolution is attributed to the random noise and the ambient interference, and can be reduced by proper signal processing usually at the expense of the dynamic behavior of the sensor.

1.1.2.2 Sensitivity

Sensitivity is defined as the induced variation in the output of the sensor compared with the change of strain that contributes. Generally the sensitivity of the sensor is determined by the physical mechanics of the sensor. For example, most of the the optical fiber Bragg grating based strain sensors have a sensitivity of approximate 1.2 pm/με [2]. The resolution of a sensor can be obtained by divided the precision by the sensitivity of the sensor.

1.1.2.3 Dynamic range

The output of a sensor is linear to the measurand only when the measurand changes within a certain range. The ratio between the largest possible values (measurement range) and smallest changeable quantity (resolution) is defined as the dynamic range. For the strain sensors in geophysical measurements, large measurement range up to tens

of με is required with resolution on the order of nε strain. Thus a dynamic range up to 10^4 or 40 dB is necessary.

1.1.2.4 Frequency response

According to the response time of the sensor, the strain sensors are usually catalogeted into two types: dynamic sensors and static (also called quasi-static) sensors. The former type can detect quick varying signals, while the latter one are used to track the change of slow varing signals. Although currently the dynamic and static sensors are defined according to the response frequency with boundary of 10 Hz, there is an essential difference between the methods for strain measurement. The dynamic sensing deals with the periodical strain signal, thus it is self-referenced, and the strain signal is evaluated in frequency domain; but the static strain sensing measures slowly varying (sometimes arbitrary) signals, and an extra reference is required, which is usually a frequency-stabilized component or an additional sensor head identical to the strain sensor but free of strain. The retrived strain is usually expressed in time domain. The static strain sensor involves the comparison between the sensor head and reference, and is more complicated to achieve high performance.

In the thesis, a new type of strain sensors – real-time strain sensor is discussed and developed. It obtaines the strain information between the sensing sensor head and the reference as the static sensor does, but it is also able to response to high frequency strain signals like the dynamic strain sensor. In chapter 5, the configuration of a real-time strain sensor with ultra-high strain resolution up to 0.05 nε is presented.

1.2 Strain sensors for geophysical applications

Risk of seismic and volcanic event prevention is one of the most important issues for the life quality improvement in highly populated areas. Those large-scale natural phenomena, however, cannot be simply studied with physical models. Geologic studies of past eruptions and empirical analysis of precursory events are the only applicable

approaches to these complex phenomena [3]. The most important parameters to describe the evolution of these processes are stress and strain variations. Risk mitigation, related to catastrophic events such as earthquakes, eruptions and landslides, is based upon an accurate monitoring on the deformation of the earth with a strain resolution on the order of nε in the static to low frequency regions.

To monitor the small strains of the earth crustal and avoid the contamination of the record with near-surface disturbances, the strain meters should be installed underground in competent rock, sometimes at depths of hundreds meters. Several types of sensors have been used for the monitoring of the strain. Borehole strain meters have been in operation of monitoring the deforming of earth for over four decades, which can provide a strain resolution of 30 pε [4]. Extension meter with length of tens meters long are also used for the measurement of tiny strain. At Aburatsubo Bay, Kanagawa, Japan, 3 sets of crystal extension meter have been used for the measurement of strain induced by oceanic tide and the seismic observation [5]. Laser interferometers are another powerful tool for the geophysical measurement and have a long history for the monitoring the strain of earth. Michelson laser interferometers with length of hundreds of meters long have been set up soon after the appearance of laser [6]. For example, there are two sets of laser interferometers installed in the 1 km deep underground at Kamioka, Japan, both having arm length of 100 meters [7]. Those types of sensors provide a theoretical strain resolution on ther order of 0.1 pε.

The above types of sensors, however, are qlarge in size and expensive. Besides, in order to monitor the small strains of the earth crustal and avoid the contamination of the record with near-surface disturbances, the strain meters often have to be installed underground in competent rock, sometimes at depths of hundreds meters. The large size of the sensors, from tens to hundreds of meters long, makes them very difficult to mount. New types of sensors with ultra-high strain resolution in the static to low frequency region, low cost and small size are desired for the geophysical measurements.

1.3 Ultra-high resolution strain sensors

The ultra-high strain resolution sensors, according to the physics mechanism, can be cataloged into three types: Electronic strain sensor, free-space laser interferometers and optical fiber sensors.

1.3.1 Electronic strain sensors

The electrical strain sensors using the electrical property change of material when it is strained. Most of the high resolution electrical strain sensors belong to the capacitive sensors, as shown in Fig. 1-2.

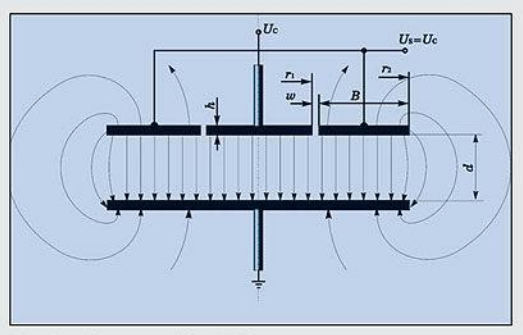

Fig. 1-2 Capacitive strain sensor

Capacitance is a property that exists between any two conductive surfaces within some reasonable proximity. Capacitive sensors use the electrical property of capacitance to make measurements. The capacitance is expressed as

$$C = \frac{A\varepsilon_r}{d}, \tag{1.2}$$

where C is the resistance, A is the effective area of the plates, ε_r is the permittivity of the space, and d is the distance between the two plates. A change in the distance or the effective permittivity between the surfaces changes the capacitance of the capacitor.

The proportionality referred to is based on the homogeneity of the electric field. To eliminate boundary effects, high performance capacitive sensors have a guard-ring electrode that surrounds the active sensor area and is actively kept at the same potential

(see Fig. 1-2) [8]. This design shields the active sensor area and provides for excellent containment of the measurement zone. Thus optimum measuring linearity over the full range is achieved within the specified accuracy. A distance resolution of 0.1 nm within a range of 500 μm is achievable with this design. Strain sensing is achieved indirectly by the measurement of distance change.

The electrical strain sensors have relative poor resolution, but they are low cost, small in size, and they can be integrated with MEMS techniques [9]. They will be mainly used in the industrial applications where low cost plays an important role.

1.3.2 Free space laser interferometers

Laser interferometry is a technique in which laser light-waves are superimposed in order to extract information about the waves. The Michelson interferometer is a typical high performance interferometer and it is also used for the strain sensing in geophysical applications. Although the free space Fabry-Perot interferometer could have higher performance, its application is limited due to the much higher cost.

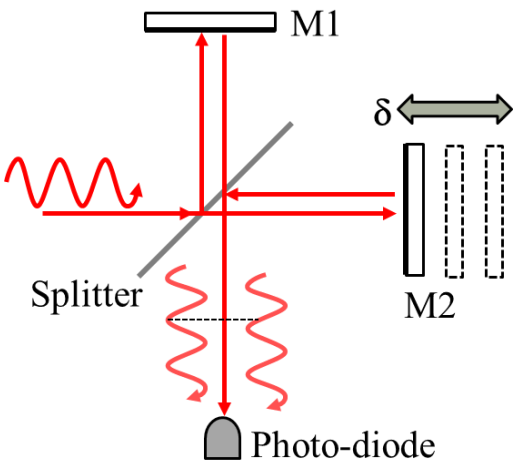

Fig. 1-3 Structure of Michelson interferometer

The Michelson interferometer is invented by Albert Abraham Michelson. Its structure is shown in Fig. 1-3. A Michelson interferometer consists of two highly

polished mirrors, M1 and M2. A laser source emits monochromatic light $E = E_0\cos(kx)$, where k is a factor refers to the laser frequency, hits a splitter which is partially reflective. So part of beam is transmitted through the splitter while the remaining is reflected. Both beams are reflected by mirrors respectively and recombine at photo-diode. So there are two paths from the light source to the detector. One reflects off the semi-transparent mirror, goes to the top mirror and then reflects back, goes through the semi-transparent mirror, to the detector. The other first goes through the semi-transparent mirror, to the mirror on the right, reflects back to the semi-transparent mirror, then reflects from the semi-transparent mirror into the detector. The two beams are coherent, thus the re-combined power of light is a function of the phase difference between the two beams

$$I = |E'|^2 = E_0^2\left(1+\cos\phi\right), \tag{1.3}$$

here φ is phase difference between the two reflected light-waves. This phase difference is determined by the traveled paths difference between the two beams.

If these two paths differ by an integer number n (including 0) of wavelengths, $\varphi = 2n\pi$, there is constructive interference and a strong signal at the detector. If they differ by an integer number and a half wavelengths (e.g., n=0.5, 1.5, 2.5 ...) there is destructive interference and a weak signal. Thus the beam path information is obtained from the intensity of the signal at detector.

There are several sets of laser interferometers in the world. Among them two sets are mounted at Kamioka, Japan. They are used for the measurement of the free vibration of the earth, earth quick, slip of layer, and so on. One of the laser interferometers is the absolute distance measurement in the direction of NS, while the other interferometer is to measure the shear strain in the direction of NS against EW. Both of the interferometers have arm lengths of 100 m. The interferometers can measure the

displacement of the mirror with resolution of 0.01 nm. A strain resolution of 0.1 pε is achieved in the recent experiments.

The Michelson interferometers have large dynamic range and ultra-high strain resolution down to sub-pε, but their large size and high cost determine that they are mainly used in the scientific research field.

1.3.3 Optical fiber strain sensor

It was over 40 years ago that the idea that optical fibers could be a useful approach to sensing and measurement first emerged [10]. Since then optical fiber sensor developed rapidly with the growth of the optoelectronic and fiber communications industries. An optical sensor uses optical fiber as the sensing element. Compared with other type of sensors, the optical fiber sensors have the advantages such as light weight, compact size, immune to electromagnetic interference, excellent resolution and measure range, and ease in implementing multiplexed and distributed sensors.

Due to their unique advantages, optical fiber sensors have been adopted in both scientific research and industrial applications such as smart materials and structure health monitoring, and they are also attractive for the field of geophysical research if they can provide high strain resolution at static to low frequency region. In the field of dynamic sensing at high frequency, optical fiber sensors have realized even better than pε resolution [11-15], their applications in the field of static strain sensing, however, are not successful up to date. Currently, the optical strain sensor has a strain resolution on the order of 1 με, which is generally satisfactory for most applications such as smart material and structure health monitoring [16], but not enough for certain applications such as the geophysical research.

The optical fiber sensors could realize comparable resolution as the free space laser interferometers in principle with much lower cost. They have already achieved high dynamic strain resolution, and their poor performance in the static to low frequency

domain is restricted by the interferometer technologies. They are very attractive for geophysical applications if proper interrogation technology is developed.

1.4 Purpose and constitution of this thesis

The purpose of our research is to develop practical optical fiber strain sensors with ultra-high strain resolution aiming the geophysical measurements. The sensors should have ultra-high resolution down to nε-order in the static to low frequency region. A serious of optical fiber sensors have been designed towards to this target.

In chapter 2, we designed an ultra-high resolution fiber Bragg grating (FBG) strain sensor for static strain measurement, interrogated by a narrow linewidth tunable laser. The sensor consists of a pair of FBGs, one for strain sensing and the other for temperature compensation. The Bragg wavelength difference between the two FBGs is evaluated utilizing a cross-correlation algorithm. We theoretically studied the performance of the sensor. The main noise sources are analyzed, and the expression of resolution is presented. The theoretical prediction agrees well with our experimental result, and well describes the numerical simulations. With the expression of resolution, the guidelines for the optimization of the sensor are revealed in detail.

In the chapter 3, we developed a practical multiplexed FBG strain sensor based on the analysis. A wavelength resolution of 3.1 fm was obtained without strain applied, corresponding to a static strain resolution up to 2.6 nε. This is the first demonstration that a nε-order static strain and large dynamic range was obtained with simple sensor configuration. With a variable strain applied by a piezo-stage, strain resolution of 17.6 nε was demonstrated, mainly limited by the precision of the testing stage. Then the sensor is put into practice to measure the crustal deformation induced by oceanic tide at Aburatsubo Bay, kanagawa, Japan, which is also monitored by 38m-long extension-meters. The crustal deformation is clearly recorded by the FBG sensor with a resolution of 10 nε. Compared with the extension-meters, the developed FBG sensor

has a comparable resolution but much smaller size (1m) and lower cost, providing a powerful tool for geophysical measurements.

In chapter 4, we developed a fiber optic static strain sensor by using a pair of Fabry-Perot interferometer (FFPI) sensor heads, to overcome the wavelength repeatability which limits the resolution of FBG sensors. Digitalized frequency modulation (FM) technology is employed to extract the detuning between the laser frequency and the resonance of FFPI. A cross-correlation algorithm is used to calculate the resonance difference from the extracted signals with high precision. An ultra-high static wavelength resolution corresponding to strain resolution down to 5.8 nε was demonstrated in experiment, with measurement range larger than 100 με. This FFPI sensor provides a comparable strain resolution and dynamic range compared with FBG sensor; with a much smaller laser sweeping rang reducing the cost of the laser.

In chapter 5 we proposed a sideband interrogation technology, for the simultaneous interrogation of the sensing and reference FFPIs. A special radio frequency (RF) signal is used to drive an intensity modulator (IM) to generate the sideband. The sideband is used to interrogate the sensing FFPI, while the laser carrier is used to interrogate the reference FFPI with typical FM technology. Experiments of static strain sensing were carried out using a tunable laser, and a cross-correlation algorithm is employed to calculate the resonance difference. With a sweeping rang of only 0.1 pm and measuring period of a few seconds, a standard deviation of measured resonance difference of 29 kHz was obtained, corresponding to a strain resolution of 0.3 nε. This is the first time that a static strain better than nε was demonstrated with optical fiber sensors. Realtime sensing is also achieved by locking the laser carrier and sideband to the two FFPIs, respectively. A RF modulator for the generation of signal to drive the IM was designed. With two proportional–integral–derivative (PID) locking loops, strain resolution down to 0.05 nε is realized, and the measuring rate is about 7 Hz. With the ultra-high strain

resolution, the proposed real-time sensor meets the strictest standard for geophysical research.

In chapter 6, we proposed a multiplexed sensing technique with identical FFPIs using a dual-modulation technology. The principle and configuration of the dual-modulation technology are introduced, and a modulation design is given based on a commercial available differential quadrature phase shift keying (DQPSK) modulator. Numerical simulation results proved that, the strain and the position of FFPI sensors could be measured simultaneously with the dual-modulation configuration.

Finally, a conclusion is given in chapter 7, with a comparison on the developed sensors.

The flowchart that summarizes the configuration of the thesis is shown in Fig. 1-4.

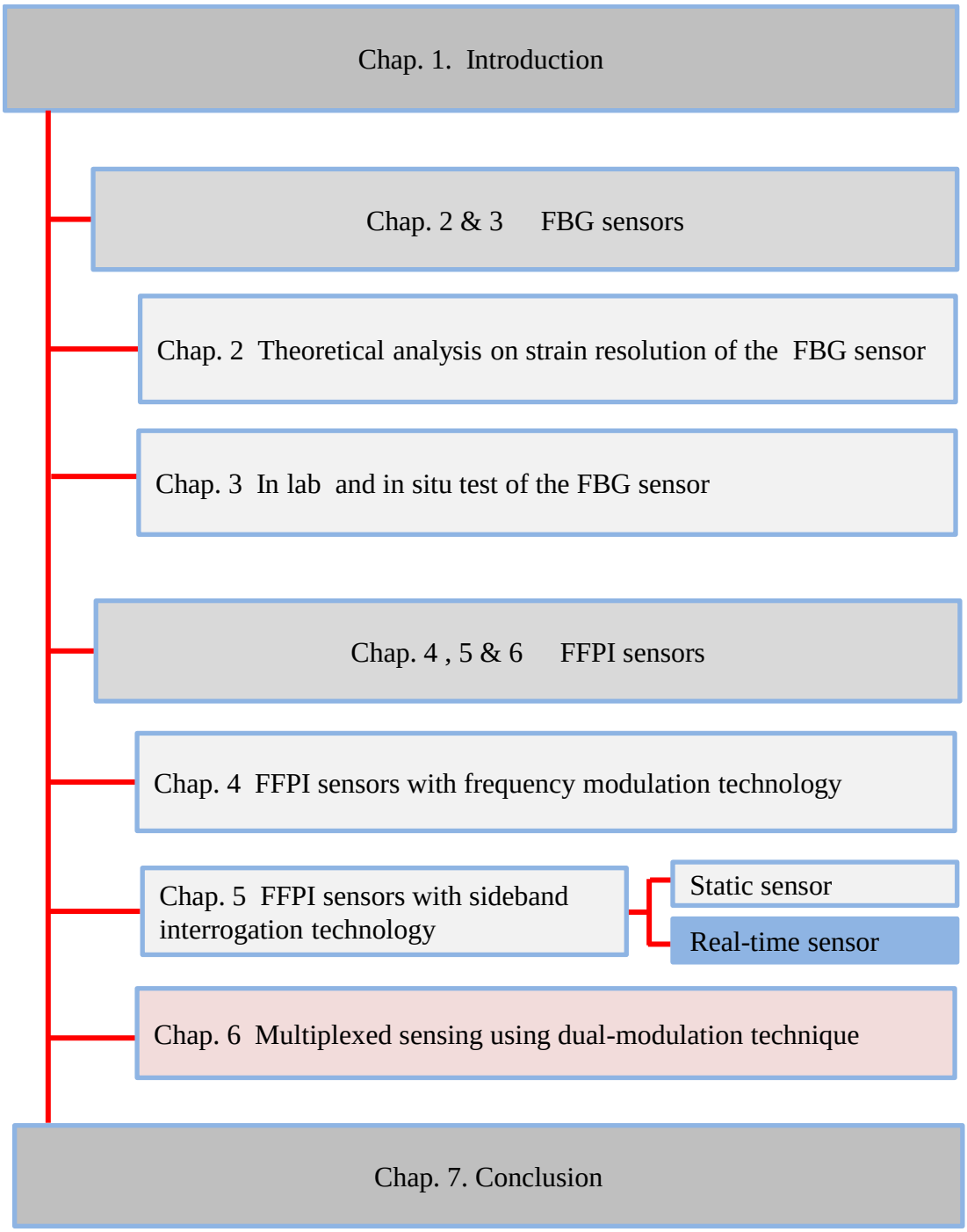

Fig. 1-4 Configuration of the thesis.

Chapter 2.
Analysis on static strain FBG sensors interrogated by a narrow linewidth tunable laser

The fiber Bragg gratings (FBGs), as one of the most widely utilized type of optical fiber sensors, have many advantages such as light weight, small size, low cost, fast response, and perfect linearity over a large range. According to the responsing time, FBG strain sensors are generally cataloged into dynamic and static sensors. High dynamic strain resolution have been already been reported in literature, while the static strain resolution is not so successful, limited to the order of με. For applications such as smart materials and smart structures, a static strain resolution of 1 με is already satisfactory, while the resolution has to been improved to nε orders for the sensors to be adopted in geophysical applications. In this chapter, we proposed a FBG sensor interrogated by a narrow linewidth tunable laser for static strain sensing. The performance of the sensor is theoretically analyzed, and the guidelines for optimization are revealed.

2.1 Introduction of FBG

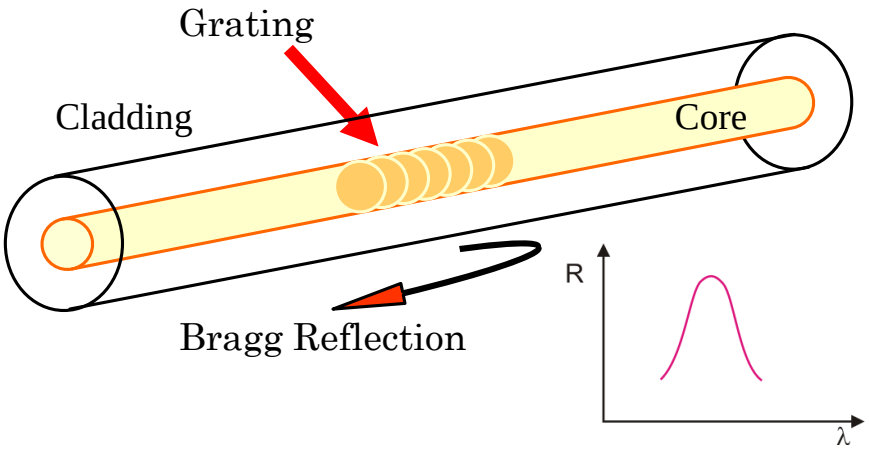

Fig. 2-1 The structure of FBG. Inset: Spectrum of FBG

FBGs are fabricated by creating periodic variations in the refractive index of the core of an optical fiber [17]. Fig. 2-1 shows the internal structure of an optical fiber with Bragg grating written inside. When light propagates through the grating, at a particular wavelength named the Bragg wavelength, the lightwave reflected (the inset in Fig. 2-1) by the varying zones of refractive indices will be in phase and amplified. The Bragg wavelength λ_B is given as

$$\lambda_B = 2n_{eff}\Lambda, \tag{2.1}$$

where n_{eff} is the effective index of the FBG, and Λ is the grating period.

2.2 FBG sensor

The Bragg wavelength of FBG varies as the FBG experiences strain or temperature change. This characteristic is used to measure strain and / or temperature using FBG by measurement of the Bragg wavelength.

From Eq. (2.1), we know that the Bragg wavelength is determined by the grating period Λ and the effective index n_{eff}. Any disturb on the two parameters will result in Bragg wavelength drift of FBG, which is

$$\Delta\lambda_B = 2n_{eff} \cdot \Delta\Lambda + 2\Delta n_{eff} \cdot \Lambda, \tag{2.2}$$

where $\Delta\Lambda$ is the grating period change of the FBG, and Δn_{eff} is the effective index change.

2.2.1 Strain sensitivity of FBG

Mechanical act on the FBG will not only change the grating period, but also the effective index due to the strain-optic coefficient. So the most direct application of this property is the FBG strain sensor. In the case that the mechanic deformation is strain along the fiber,

$$\frac{\Delta\lambda_B}{\lambda_B} = \frac{\partial\Lambda}{\partial L} \cdot \frac{\Delta L}{\Lambda} + \frac{\partial n_{eff}}{\partial L} \cdot \frac{\Delta L}{n_{eff}}, \tag{2.3}$$

where ΔL is the length change of the fiber, $\varepsilon = \Delta L/L$ is the applied strain to the fiber, $\partial n_{eff} / \partial L$ is the strain-optic coefficient of FBG.

For the uniform strain, $\frac{\partial\Lambda}{\partial L} \cdot \frac{\Delta L}{\Lambda} = \varepsilon$, and $\frac{\partial n_{eff}}{\partial L} \cdot \frac{\Delta L}{n_{eff}} = -p_e\varepsilon$, where p_e is a coefficient calculated from the strain-optic effect of the material of FBG. So the strain sensitivity of FBG is

$$\frac{\Delta\lambda_B}{\lambda_B} = (1 - p_e)\varepsilon. \tag{2.4}$$

For optical fiber made by fused quartz, p_e is calculated to be 0.216 at 1550 nm [18]. Thus the strain sensitivity is approximately 1.2 pm/με, and is slight different according to the material and structure of the fiber.

In the case the fiber is applied a uniform pressure, e.g., the fiber is immerged into water to measure the press, the grating period will also change following the Poisson's ratio, and the strain-optic effect also takes place. The strain sensitivity of FBG at 1550 nm is about 2.7 pm/με in this case. Although this value is larger than the axial strain sensitivity, the deformation on radius is much smaller than the axial strain with the same pressure. So generally speaking, the FBG is more sensitivity to the axial pressure.

2.2.2 Temperature sensitivity of FBG

Similar to the mechanics strain, the change of temperature will also result in drift of the Bragg wavelength of FBG. This drift mainly attributes to three mechanisms: the thermal index change, the index change due to thermal expansion, and the axial thermal expansion of fiber. From Eq. (2.2), we get the Bragg wavelength shift when the temperature of FBG changes

$$\frac{\Delta\lambda_B}{\lambda_B} = \left[\frac{\partial n_{eff}}{\partial T} + \frac{\partial n_{ep}}{\partial T}\right]\cdot\frac{\Delta T}{n_{eff}} + \frac{\partial\Lambda}{\partial T}\cdot\frac{\Delta T}{\Lambda}, \tag{2.5}$$

where ΔT is the temperature change, $\partial n_{eff}/\partial T$ is the thermal-index coefficient of fiber, $\partial n_{ep}/\partial T$ is the thermal expansion induced index coefficient, and $\partial\Lambda/\partial T$ is the thermal axial expansion coefficient of fiber.

For the fused quartz based FBG, the temperature sensitivity of FBG is express as

$$\begin{aligned}\frac{\Delta\lambda_B}{\lambda_B} &= \left(6.8\times10^{-6} - 3.85\times10^{-7}\right)\cdot\Delta T + 5.5\times10^{-7}\cdot\Delta T \\ &= 6.965\times10^{-6}\cdot\Delta T\end{aligned} \tag{2.6}$$

where ΔT is the temperature change, and the three parameters are the coefficient for the thermal index change, the index change due to thermal expansion, and the axial thermal expansion of fiber. The thermal index effect is the dominating factor. For FBG at 1550 nm, the temperature sensitivity is approximately 10.3 pm/℃ [2].

2.2.3 Temperature compensation for strain sensor

As the FBG is sensitive to both strain and temperature, temperature compensation is necessary for the high performance strain sensors. A lot of methods have been proposed for the temperature compensation.

A simple solution is to add a reference FBG which is strain-isolated and placed close to the sensing FBG. The strain information is obtained by measurement of the Bragg wavelength difference between the sensing and reference FBGs. This configuration is simple and have good compensation result, suitable for high performance strain sensing where a strain-isolated reference FBG is possible [19].

Other temperature compensation methods mainly focus on the simultaneous measurement of strain and temperature with single fiber configuration. In ref [20], two individual FBGs with different Bragg wavelengths are written in the same fiber. The strain and temperature coefficient of the two FBGs is slightly different. So by measuring the two independent Bragg wavelengths, both strain and temperature can be obtained. Another paper reported a simultaneous measurement configuration by measuring the first and second diffraction of a long period FBG [21]. When two FBGs in series are etched to different diameters, the two FBG have the same temperature coefficient but different strain expansion ratio due to different diameter. Thus the strain information can be calculated from the Bragg wavelength difference [22]. A further improvement is to etch the FBG to tapered section diameter, and a broadband source is used for interrogation. The reflected power is a linear function of strain and insensitive to temperature [23]. Dual interferometer configuration realized using photonics crystal fiber was also reported for simultaneous measurement of strain and temperature [24].

Among those compensation methods, the single fiber configuration has the advance of simple installation but suffers from the cross-talk between temperature and strain. For the geophysical applications, ultra-high resolution is required, and there is enough space

for the reference FBG. So in our configuration we use a strain-isolated reference FBG for temperature compensation.

The temperature sensitivity of FBG is influenced by the package of the FBG. From Eq. (2.6) we know that it also involves the thermal axial expansion of the FBG. For a packaged FBG, the thermal expansion coefficient is determined by the package material instead of the naked fiber, and the temperature sensitivity of FBG will change accordingly. Special attention should be paid to this issue.

2.3 Interrogation for FBG sensor

According to optics source for interrogation, FBG sensors are cataloged into two types. The first type uses broadband source to interrogate the FBG sensor, as shown in Fig. 2-2. The FBG has high reflection at the Bragg wavelength, and the reflected beam is demodulated using optical spectrum analyzer (OSA), filter, etc [25-27]. This method is simple, but difficult to achieve high resolution. Accuracy wavelength demodulation requires a narrow bandwidth FBG, which has low reflected power and increases noise in the wavelength demodulation, as shown in Fig. 2-2.

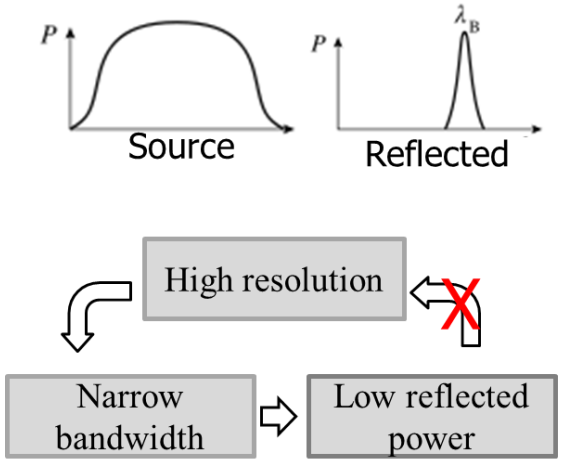

Fig. 2-2 Interrogation of FBG with broadband optical sources.

Feasible high resolution sensors use narrow linewidth sources for interrogation. One common configuration for interrogation of FBG is shown in Fig. 2-3. The laser wavelength is set to the middle reflection of FBG, and the reflected power is monitored. When the FBG is strained, the Bragg wavelength will shift accordingly, so the reflected power will also change. For the static strain sensing, a frequency-locked laser is used for interrogation. Strain resolution up to 1.2 nε/√Hz was reported with a molecular absorption cell [28]. For the dynamic strain sensing, the wavelength is locked to the middle reflection of the FBG with a servo-loop. Strain resolution up to 45 pε/√Hz was reported [11]. Those types of sensors are simple and high sensitive. The main drawback is the small measuring range, limited by the linear range of the spectrum of FBG. For applications such as geophysical research where both high resolution and large range are required, other interrogation methods are required.

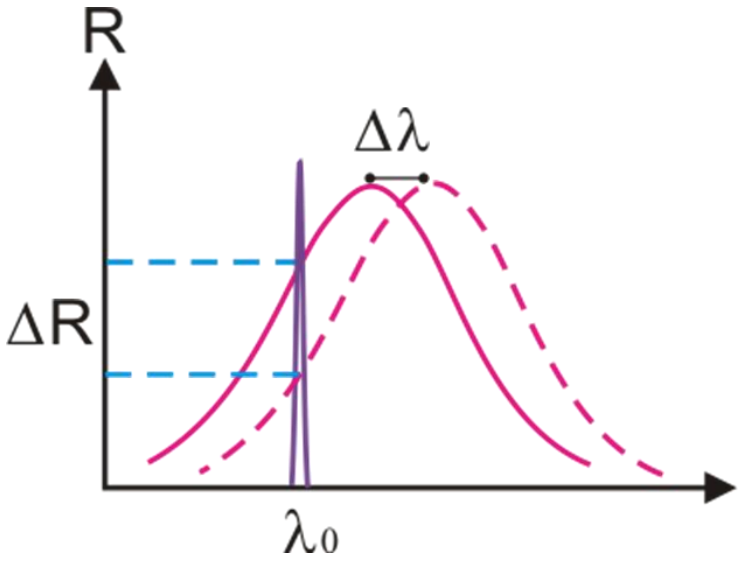

Fig. 2-3 Interrogation of FBG sensor with a narrow linewidth source

2.4 Narrow linewidth tunable laser based sensors

Thanks to the development of the laser techniques, the narrow linewidth tunable laser is now commercial available at reasonable price. The output power of narrow linewidth tunable laser is high enough to measure the FBG's spectrum with high

signal-to-noise ratio. In our research, a multiplexed static strain FBG sensor based on a narrow linewidth tunable laser was proposed, capability of static sensing with ultra-high strain resolution and large dynamic range for the purpose of geophysics applications [29].

2.4.1 Sensor configuration

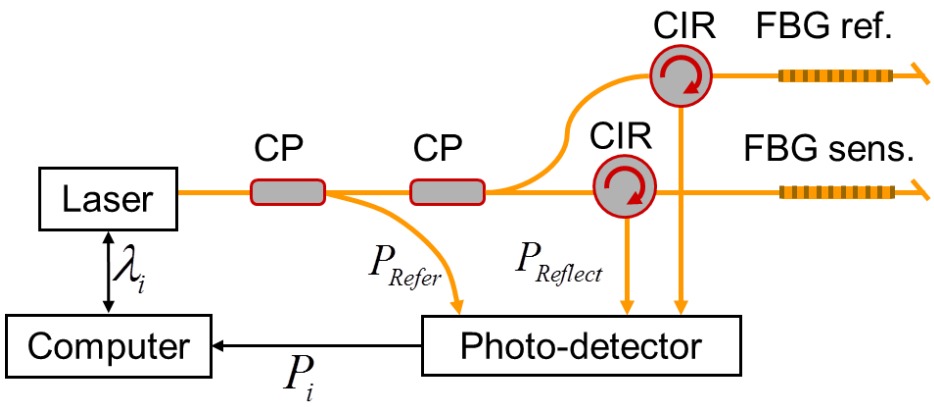

Fig. 2-4 Configuration of narrow linewidth tunable laser based FBG static strain sensor. CP, coupler; CIR, circulator; FBG ref., FBG for referencing; FBG sens., FBG for sensing.

The configuration of the FBG sensor is shown in Fig. 2-4. The system consists of a pair of identical FBGs; one is for the sensing of strain and the other is strain-free working as a reference. The two FBGs are mounted close, supposed to have the same temperature change. As a result, the relative Bragg wavelength difference indicates the strain of the sensing FBG. A narrow linewidth tunable laser is used to interrogate the FBGs, and the lightwaves reflected from the FBGs are detected by photo-detectors. While the wavelength of the tunable laser sweeps over the principal peaks of the FBGs' reflective spectra, their reflectivity are sampled at a discrete sequence of wavelengths λ_i with a step of $d\lambda$. The reflectivity of the sensing FBG is labeled as $R(\lambda_i)$, while the reflectivity of the reference FBG is labeled as $R_R(\lambda_i)$. Assuming the two FBGs have the

same spectra shape when the sensing FBG experiences strain variation, the reflectivity satisfies

$$R_R(\lambda_i) = R(\lambda_i + \Delta\lambda) = R(\lambda_{i+\varepsilon}), \tag{2.7}$$

here $\Delta\lambda$ is the wavelength shift caused by strain. $\varepsilon = \Delta\lambda/d\lambda$ is the corresponding index shift. Certain algorithm is then employed to demodulate the wavelength shift $\Delta\lambda$ by comparing the two spectra.

2.4.2 Noise analysis

Generally, the measured reflectivity of an FBG suffers from the intensity noise of the laser and the photo-detector, and from the wavelength inaccuracy of the tunable laser. These errors are the origins of the strain resolution of the sensor.

2.4.2.1 Relative intensity noise

The calculated reflectivity is the ratio of the reflected power from the FBG and the incident optical power. The intensity noise in the measurement of optical power includes the shot noise of the light, the electronic noise of the photo-detector, and the quantization noise in the analog-to-digital (A/D) convert processing. Furthermore, the wavelength sweep processing of the tunable laser is often companied with respectable intensity variation. All above noises except the quantization noise are influenced by the integration time. For example, Fig. 2-5 illustrates the intensity noise level of a photo-detector (Agilent 81635A) as a function of the integration time. Longer integration time can reduce the intensity noise level, but the sensing speed slows down simultaneously. In this paper, the divergence of the measured reflectivity caused by above intensity noises is labeled as ΔR_{elec}.

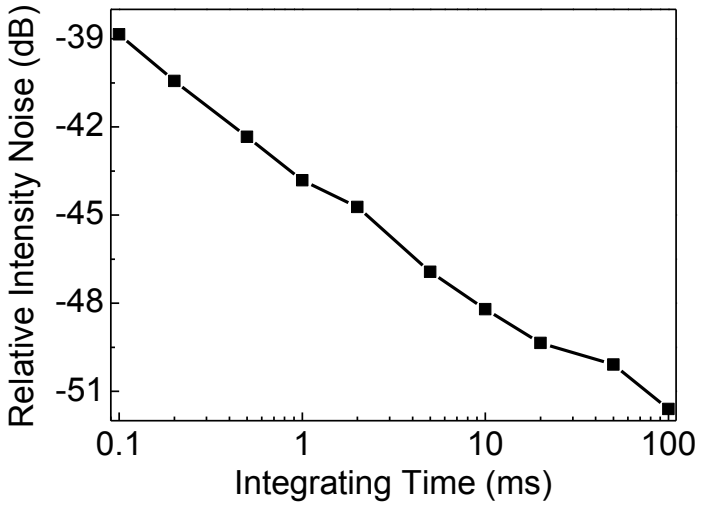

Fig. 2-5 Relative intensity noise level vs. integration time of a photo-detector (Agilent 81635A)

2.4.2.2 The wavelength repeatability of the tunable laser

The definition of the wavelength repeatability is the random uncertainty of the logged wavelength of the tunable laser source in repeat sweeps. This random uncertainty is noted as $\delta_1\lambda$ here. Since the reflectivity of the FBG is a function of the wavelength, the uncertainty of the logged wavelength is converted into error in reflectivity. The convert coefficient is the differential of the FBG's spectrum, as shown in Fig. 2-6. This error in reflectivity is expressed by $R'(\lambda)\cdot\delta_1\lambda$, where $R'(\lambda)$ is the differential coefficient of the FBG's spectrum. Generally, the repeatability $\delta_1\lambda$ is much smaller than the absolute wavelength inaccuracy of the laser. Because the Bragg wavelength is figured out by comparison between logged spectra, the absolute wavelength inaccuracy is of less importance here.

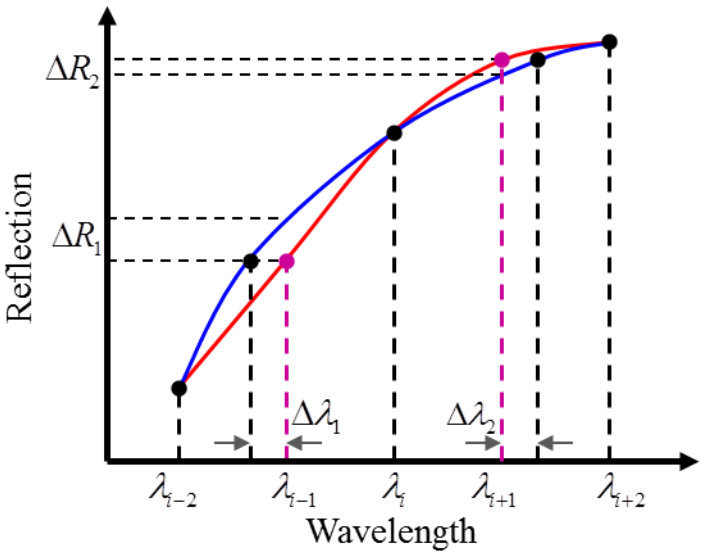

Fig. 2-6 Wavelength repeatability induced reflectivity error in measurement. Blue and Red line: two measured spectra with wavelength fluctuation, where $\delta\lambda_1$ and $\delta\lambda_2$ are the wavelength differences between two repeated measurements.

2.4.2.3 Linewidth of the tunable laser

The linewidth of the tunable laser $\delta_2\lambda$ describes the deviation range of quick frequency jitter of the laser. Similar to the wavelength repeatability, the quick frequency jitter is also converted into the error in the measured reflectivity. The amplitude is no larger than $R'(\lambda)\cdot\delta_2\lambda$, as it is averaged during the integration time.

2.4.2.4 Wavelength stability of the tunable laser

The wavelength stability of the tunable laser describes the slow wavelength drift of the laser over long term. This drift causes large error if it is not appropriately compensated. In the proposed static strain sensor, the strain information is calculated from the spectral difference between two identical FBGs. This configuration compensates the temperature induced Bragg wavelength shift and the influence from the slow wavelength drift of the laser source at the same time.

In summary, the total noise in the measured reflectivity of the FBG can be expressed as:

$$N(\lambda) = \Delta R_{elec} + R'(\lambda) \cdot \delta\lambda, \tag{2.8}$$

where $\delta\lambda = [(\delta_1\lambda)^2 + (\delta_2\lambda)^2]^{1/2}$ is the total wavelength inaccuracy.

2.4.3 Cross-correlation algorithm

In our analysis a cross-correlation algorithm is employed to demodulate the wavelength shift $\Delta\lambda$ from the measured spectra, because this algorithm is proved to have very good resolution compared with other algorithms such as the centroid detection algorithm (CDA) and the least square fitting algorithm (LSA) [30-32]. Once the spectrum of the reference FBG and that of the FBG under strain are recorded, the cross-correlation product is calculated to determine the Bragg wavelength difference between the two spectra

$$C(j) = \sum_{i=-N}^{N} R(\lambda_{i+j}) R(\lambda_{i+\varepsilon}). \tag{2.9}$$

In Eq.(2.9), it is assumed that both $R(\lambda_i)$ and $R_R(\lambda_i)$ are equal to zero if the indices lie outside their ranges. This assumption is acceptable as long as the sampling range covers the whole principal peaks of both FBGs. $C(j)$ has the maximum at $j = \varepsilon$, where the two spectra overlap completely and ε is demodulated from the index when $C(j)$ is at its maximum. Due to the random errors in the measured reflectivity, the retrieved ε deviates from $\Delta\lambda/d\lambda$, and the deviation range is the resolution of the sensor. It should be mentioned that although the index of maximum $C(j)$ falls into an integer which is the nearest to ε, ε can be precisely calculated either by interpolation or by curve-fitting around the maximum.

Because of the random errors described above, the measured spectrum is the sum of real spectra and the random error. The correlation product is then modified as

$$C'(j) = \sum_{i=-N}^{N} R(\lambda_{i+j}) R(\lambda_i) + \sqrt{2} \sum_{i=-N}^{N} R(\lambda_{i+j}) N(\lambda_i) = C_R(j) + C_N(j). \tag{2.10}$$

Here the sum of random error is written as $\sqrt{2}N(\lambda)$ because they are independent; $\varepsilon = 0$ is assumed to simplify the analysis without any influence on the resolution.

The first term $C_R(j)$ in Eq. (2.10) is the auto-correlation curve of the real spectrum without noise, as shown in Fig. 2-7 (the black dashed line). It has a peak (labeled P) at $j = 0$ and declines when j diverges from 0. The second term $C_N(j)$ is the cross-correlation of the real spectrum and the random error. It makes the actual cross-correlation curve $C'(j)$ fluctuate, as shown as the red line in Fig. 2-7. Because only the relative amplitude is concerned with the position of the maximum, we shift $C'(j)$ to pass through point P, the peak of $C_R(j)$, as shown as the dashed red line in Fig. 2-7. The random error makes the shifted curve fluctuate around the autocorrelation curve. The deviation is a function of the index j

$$\begin{aligned}\Delta_N(j) &= \sum_{i=-N}^{N}\sqrt{2}R(\lambda_i)N(\lambda_i) - \sum_{i=-N}^{N}\sqrt{2}R(\lambda_{i-j})N(\lambda_i)\\ &= \sqrt{2}j\cdot d\lambda\cdot\left(\sum_{i=-N}^{N}R'(\lambda_{i-j/2})\cdot\Delta R_{elec} + \sum_{i=-N}^{N}R'(\lambda_{i-j/2})R'(\lambda_i)\cdot\delta\lambda\right)\\ &= \Delta_{N,elec}(j) + \Delta_{N,\lambda}(j).\end{aligned} \tag{2.11}$$

Here $\Delta_{N,elec}$ and $\Delta_{N,\lambda}$ are the noises caused by the relative intensity noise and the wavelength inaccuracy, respectively. Δ_N has a mean of zero and a standard deviation as

$$\sigma(\Delta_N) = \sqrt{\sigma^2(\Delta_{N,elec}) + \sigma^2(\Delta_{N,\lambda})}. \tag{2.12}$$

The gray zone in Fig. 2-7 shows the fluctuation range of the shifted cross-correlation curve. The peak of $C'(j)$ appears in the region satisfying

$$C_R(j) + \frac{\sigma(\Delta_N(j))}{2} \geq C_R(0). \tag{2.13}$$

The factor of 1/2 in Eq. (2.13) is because only the positive $\Delta_N(j)$ causes the peak deviating from $j = 0$ while the negative value does not. Once the expressions of $C_R(j)$ and $\sigma(\Delta_N(j))$ are obtained, the wavelength resolution can be calculated from Eq. (2.13).

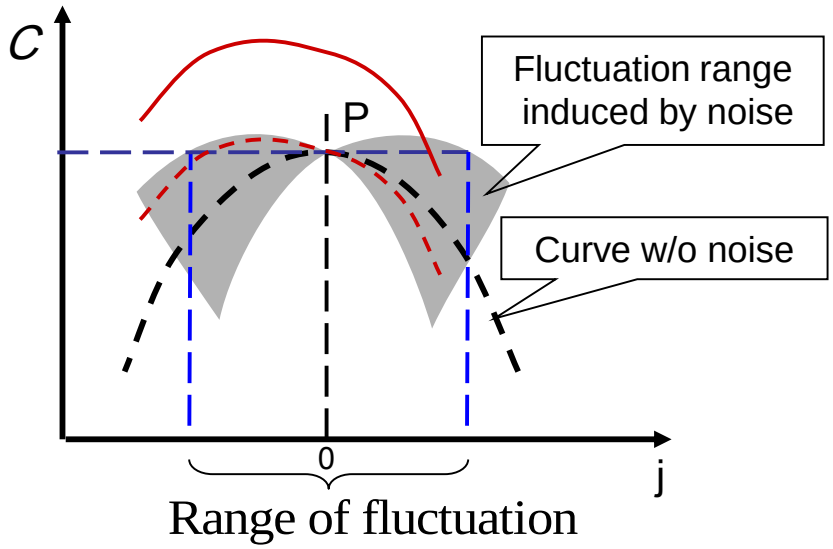

Fig. 2-7 The cross-correlation curve around the peak. Black dashed line: cross-correlation product without noise; Red line: original correlation product with noise; Dashed red line: shifted correlation product with noise. Gray zone: the region of cross-correlation curve fluctuates with noise.

2.4.4 Model of FBG's spectrum

N-order Gaussian curve is employed as the model of the FBG's spectrum for quantitative analysis

$$R(\lambda) = \exp\left(-\left(\frac{2(\lambda-\lambda_0)}{\lambda_{width}}\right)^{2n}\right) = \exp\left(-\left(\frac{2i}{w}\right)^{2n}\right). \quad (2.14)$$

where $\lambda = \lambda_0 + i \cdot d\lambda$, $d\lambda$ is the wavelength sweep step and $\lambda_{width} = w \cdot d\lambda$ is the full width at 1/*e* maximum of the FBG's spectrum. *n* is the order of Gaussian function, working as a shape parameter in the model. For FBGs with smooth spectra (maximum reflectivity less than 80%), *n* is 1; for a high reflectivity FBG with a spectrum of a flat peak and sharp slopes, *n* is a large integer.

2.4.5 Deduction of strain resolution

With the above expression of FBG's spectrum, we obtain following expressions around $j = 0$

$$C_R(0)-C_R(j)\approx\frac{(0.972n+0.28)}{w}\cdot j^2, \tag{2.15}$$

$$\sigma\left(\Delta_{N,elec}\right)\approx 2j\cdot\sqrt[4]{\frac{n^2+0.26n+0.3}{w^2}}\cdot\sigma\left(\Delta R_{elec}\right), \tag{2.16}$$

$$\sigma\left(\Delta_{N,\lambda}\right)\approx j\cdot\sqrt{\frac{20n^2-9}{w}}\cdot\frac{\sigma(\delta\lambda)}{w\cdot d\lambda}. \tag{2.17}$$

As long as the sampling range covers the whole principal peak of the FBG, which is usually satisfied in experiments, above approximations describe the expression with good precision. While w varies from 16 to 1024, and n varies from 1 to 5, the approximation of Eqs. (2.15) and (2.16) has an error less than 1%. For Eq.(2.17), the error is less than 5% for n = 1 and a little larger when $n \geq 2$. With above approximations we calculate the resolution with Eq. (2.13) as

$$\lambda_R=\sqrt{d\lambda}\cdot\sqrt{\frac{\sqrt{n^2+0.26n+0.3}}{(0.972n+0.28)^2}\cdot\lambda_{width}\cdot\sigma^2\left(\Delta R_{elec}\right)+\frac{20n^2-9}{(1.944n+0.56)^2}\cdot\frac{\sigma^2(\delta\lambda)}{\lambda_{width}}}, \tag{2.18}$$

where λ_R is the wavelength resolution of the sensor, $d\lambda$ the wavelength sweep step of the laser, $\sigma(\Delta R)$ the standard deviation of the relative intensity noise, $\sigma(\delta\lambda)$ the standard deviation of wavelength inaccuracy. From the wavelength resolution, the strain resolution can be simply deduced by the strain-wavelength coefficient of 1.2 pm/με.

2.4.6 Verification of resolution expression

The analysis is verified by numerical simulation using a LabVIEW program. First, we generated the spectrum of FBG. Then we add wavelength noise of $\delta\lambda$ and the reflection noise of ΔR to simulate the measured spectrum with noise. Cross-correlation is used to calculate the wavelength difference between the two spectra. Two sets of noises levels are used as simulation conditions as shown in Fig. 2-8. Under each condition, the Bragg wavelength is calculated for 1000 times, and then the standard deviation (i.e., the resolution) is obtained and compared with that calculated from

Eq.(2.18). The resolution by simulation is well predicted by the analytical result, proving that Eq. (2.18) is proper in describing the resolution of the sensor.

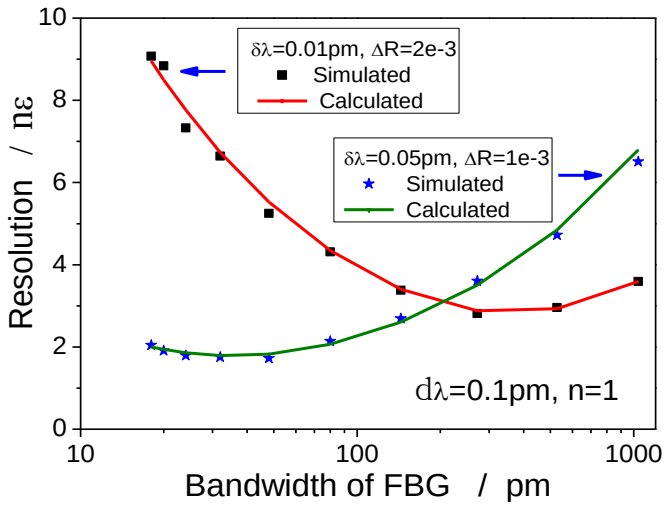

Fig. 2-8 Calculated resolution vs. simulated resolution.

In chapter 3, a static strain resolution of 2.6 nε was demonstrated using the same configuration mentioned [32]. The experimental parameters are listed in Table 1. With these parameters, the strain resolution of the sensor is theoretically calculated to be 2.3 nε using Eq.(2.18). This value is very close to the experimental result of 2.6 nε, showing the effectiveness of the theoretical analysis.

Table 1 Parameters of sensor

Parameter	$\delta\lambda$	Re_{lic}	$d\lambda$	w_{idth}	n
Value	0.05 pm	-40 dB	0.1 pm	56 pm	1

2.5 Optimization of narrow linewidth tunable laser based FBG sensors

Based on the above analytical result of the resolution given by Eq.(2.18), we discuss the guidelines for the sensor design and optimization, that is, how to design the system

and choose the FBG, the tunable laser, the photo-detector, and the system configuration to realize nano order strain resolution.

2.5.1 FBG spectrum

The first important issue is to select the FBG with suitable spectrum, including the shape of profile and the bandwidth. According to Eq. (2.18), the resolution of FBG sensors with different shape parameter *n* is shown in Fig. 2-9. The 1st order Gaussian shape FBG has better resolution with narrower bandwidth, which is more preferable in practice because it requires smaller wavelength tunable range, and can achieve higher measurement speed. We can see from Fig. 2-9 that, with the given $d\lambda$, $\delta\lambda$, and ΔR, which are practical values for commercially available devices, nε-order resolution is achievable with a proper FBG.

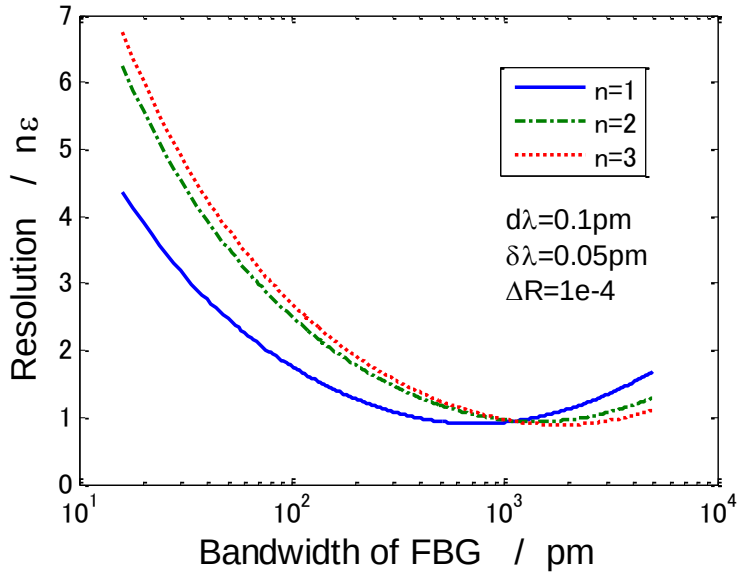

Fig. 2-9 Strain resolution vs. bandwidth of FBG with different shapes

From Fig. 2-9 we also find that an optimized bandwidth exists to have best resolution. From Eq.(2.18), the optimized bandwidth is calculated when $n = 1$

$$\lambda_{width} = \frac{1.48\sigma(\delta\lambda)}{\sigma(\Delta R_{elec})}. \tag{2.19}$$

And the corresponding wavelength resolution of the sensor is

$$\lambda_{R,best} = 1.54\sqrt{d\lambda \cdot \sigma(\Delta R_{elec}) \cdot \sigma(\delta\lambda)}. \tag{2.20}$$

Eqs (2.19) and (2.20) show the achievable resolution of the sensor at given laser source and photo-detectors.

In practice, the optimized bandwidth of FBG may not be usable due to the limitation of the tunable range of the laser source or due to the limitation on measurement speed. We compared the resolution with FBGs of different bandwidths at fixed intensity noise level and wavelength inaccuracy, respectively. As shown in Fig. 2-10, narrower bandwidth FBG is preferred to achieve higher resolution when using a laser source with good wavelength inaccuracy. On the other hand, a broad bandwidth FBG is suitable to make full use of the low-intensity-noise photo-detectors as shown in Fig. 2-11.

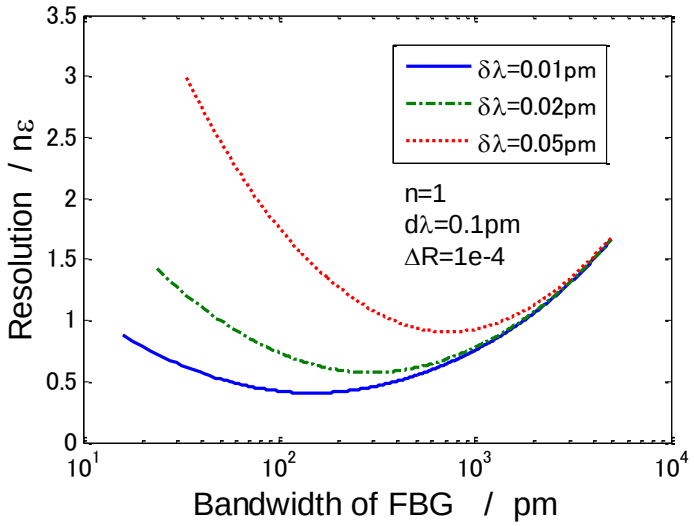

Fig. 2-10 Strain resolution vs. FBG bandwidth under different wavelength inaccuracy of the laser sources

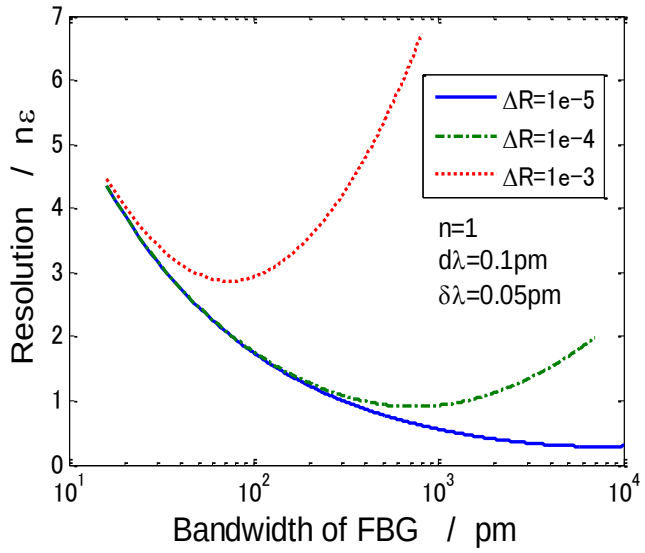

Fig. 2-11 Strain resolution vs. FBG bandwidth under different intensity-noise levels.

2.5.2 Sweep step of the laser

From Eq. (2.18) we know that the sweep step $d\lambda$ plays an important role in the resolution. The resolution is proportional to the square root of $d\lambda$ at a fixed noise level. Using a shorter sweep step (a smaller $d\lambda$) while keeping the integration time of the photo-detector constant produces the best resolution. It consumes, however, longer time to complete the sweep. If the sweep speed remains constant and but use a shorter sweep step, the integration time at the photo-detector is reduced, which enhances the intensity noise level. As a result, the resolution is not necessarily improved. Therefore, the most suitable sets of parameters depend on a specific application's requirements on the measurement speed and the resolution.

2.5.3 Wavelength repeatability and linewidth of the tunable laser

The total wavelength inaccuracy of the sensor is the sum of the linewidth and the wavelength repeatability of the tunable laser. For most tunable lasers, the wavelength repeatability is much larger than their linewidth, and thus plays the dominant role in this

type of sensors. As a result, the linewidth of the laser source is of less importance here compared with in wavelength-fixed laser based dynamic FBG strain sensors, because the Bragg wavelength is obtained from all of the sampled points of the FBG reflection spectrum integrally and the quick frequency jitter is averaged. In choosing a tunable laser source, more attention should be paid to higher wavelength repeatability instead of narrower linewidth, as long as using a single mode laser source normally with a linewidth of ~MHz.

2.6 Discussion on the proposed sensor

Alghough the laser sweeps with relative large step (0.1 pm in our experiments) and wavelength repeatability (0.05 pm), the proposed sensor could detect the Bragg wavelength with much better resolution up to fm, corresponding to a strain resolution of nε order. The capability of high strain resolution is attributed to two main factors. First, the Bragg wavelength is calculated from a spectrum curve of the FBG, which is formed by a serious independent measurement of the FBG's reflection. Both the intensity noise and the wavelength repeatability of the laser is averaged and suppressed during the calculation. Second, the cross-correlation algorithm is employed to detect the Bragg wavelength difference between the two FBGs. The cross-correlation calculation is weighted average in nature, where the high reflection part of spectrum has larger weight in the detection of wavelength difference, and the low reflection part has smaller weight. As a result, the cross-correlation algorithm achieves good balance between utilizing all the sampling data and suppressing the accompanied noises. For comparison, in either centroid detection algorithm or the least square fitting algorithm, all of the measured data has the same contribution to the final result, and is less stable against random error.

Although the proposed sensor can only realize ultra-high static strain resolution at a relative long measuring period limited by the wavelength sweeping speed of the laser, it has the unique merit of simultanelus measurement of two or more FBG's spectra, and

the measurement range is large to achieve high dynamic range. Together with the ultra-high resolution, the sensor configuration is simple and robust, suitable for the in situ strain sensing under harsh environment.

2.7 Conclusion

In this chapter, we proposed a static strain sensor using a pair of identical FBGs, one for strain sensing and the other for compensation. A narrow linewidth tunable laser is used for the interrogation of the FBGs. After a discussion on the noise sources, the expression of strain resolution is deduced with a cross-correlation algorithm. The resolution calculated by using the expression is in good agreement with numerical simulation, and is further verified by experimental result. Based on the analysis, the guidelines are revealed for designing and optimizing this type of sensors to realize nano order strain resolution for static strain sensing. This theoretical analysis provides a firm base for the development of practical ultra-high resolution FBG static strain sensor.

Chapter 3.
Ultra-high static strain resoltuion FBG sensors for crustal deformation measurements

Based on the analysis on the FBG sensors interrogated by linewidth tunable laser, we built a practical FBG strain sensor for the geophysical applications, which is successfully adopted to measure the crustal deformation induced by oceanic tide at Aburatsubo Bay, Kanagawa, Japan. Before the in situ experiments, a series of experiments were carried out at laboratory to verify the performance of the sensor.

The principle of the FBG sensor is already introduced in chapter 2, while the configuration is slight different in each experiments. In this chapter, the system configuration of the sensor and the experimental results are introduced in detail.

3.1 In lab experiments without strain applied

The strain resolution of a sensor is determined by the noise level of the sensor, which can be valued without strain applied. At the beginning of research, experiments were carried out without strain applied to ascertain the ultimate performance of the sensor in laboratory.

3.1.1 System configuration

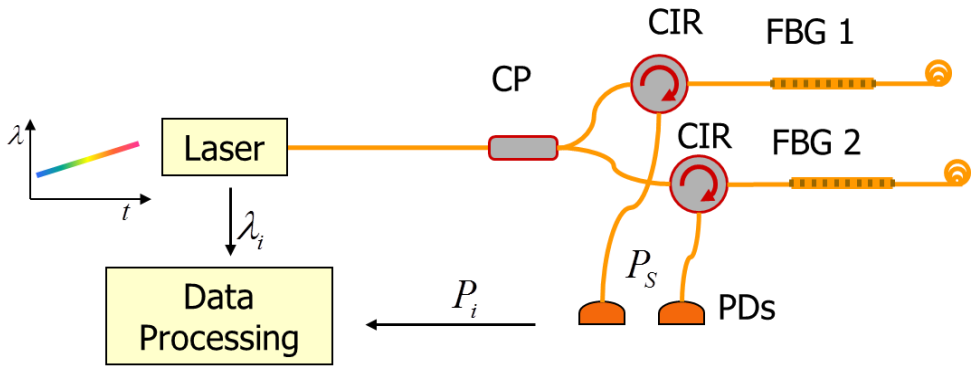

Fig. 3-1 Configuration of initial FBG strain sensor without strain applied.

The configuration of the sensor is shown in Fig. 3-1. The hardware of the system is designed with small number of parts for working under harsh environment with high reliability. A narrow linewidth tunable laser (Agilent 81680A, linewidth 100 kHz) is used to interrogate a pair of FBGs via a 3-dB coupler. The reflected light beams from FBGs are detected by a pair of photo-detectors (Agilent 81634B). The two FBGs (fabricated by Fujikura Ltd.) work as the strain sensor and the reference, respectively. In the experiments they are both free of strain. They have almost the same parameters in order to get better temperature compensation effect. The Bragg wavelengths are near 1550 nm with bandwidth of 56 pm, as shown in Fig. 3-2. The maximum reflection around 60% is chosen considering both high reflected power and bell-shaped curve for peak detection. The whole measurement is controlled by LabVIEW program running on a personal computer. The system can easily be extended for multiplexed sensing by cascading additional pairs of FBGs with wavelength division multiplexing (WDM) technology.

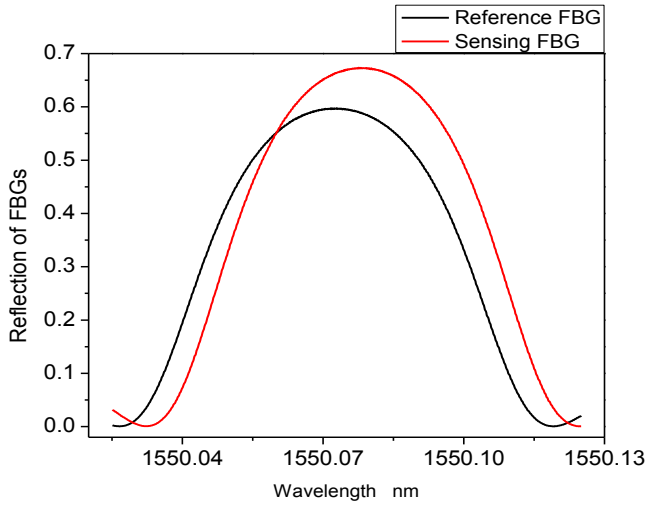

Fig. 3-2 Spectra of FBGs in the sensor configuration

In the experiments, the wavelength of laser is tunable in a step sweep mode with step of 0.1 pm. At each step, the reflected power for both FBGs and the corresponding wavelength is recorded. The sweep range is 0.9 nm, covers the principal peak of the spectra of both FBGs. Fig. 3-2 is an example of scanned spectra of the FBGs after one complete sweep. The two spectra are similar in shape, but stagger in horizontal axis. A cross-correlation algorithm is employed to calculate how much the two spectra stagger in wavelength. Gaussian fitting was implemented around the cross-correlation peak for higher resolution in determination of the correlation curve peak position.

3.1.2 Experimental results

In the configuration of sensor, the two FBGs have similar parameters, and they are placed close to each other to experience the same temperature. When temperature changes, both the Bragg wavelengths will shift according to Eq. (2.6). As a result, their Bragg wavelength difference is immune to temperature fluctuation, and only determined by the applied strain difference. In this experiment, because both of the FBGs are free of strain, the expected Bragg wavelength difference remains constant in repeat measurements. However, due to the random noises in the system and the ambient interference, the measured wavelength difference will fluctuate within a certain range.

This fluctuation limits the wavelength resolution in the measurement of Bragg wavelength difference, and thus determines the strain resolution of the sensor.

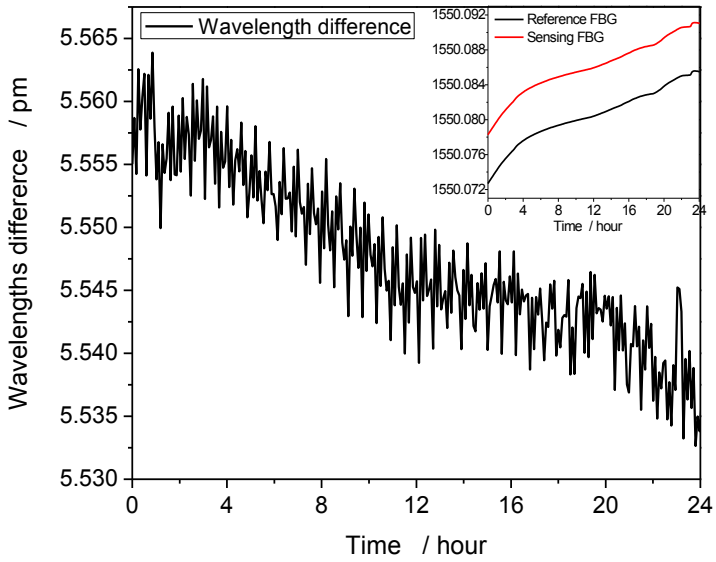

Fig. 3-3 Measured wavelength difference between the FBGs. Inset: Bragg wavelength drift of the FBGs

The measured Bragg wavelength between the FBGs over 24 hours is shown in Fig. 3-3. The standard deviation of the difference is 6.7 fm. At the meantime, the drifts of the Bragg wavelengths of the 2 FBGs during the experiments are also shown in the inset figure of Fig. 3-3.

If the two FBGs have identical temperature-wavelength coefficient, their Bragg wavelength difference is absolutely independent with temperature change. However, if the two FBGs have slightly different temperature-wavelength coefficient, the wavelength difference will have dependence with temperature. However, because the temperature-wavelength coefficient is a constant for either FBG, this dependence can be removed once the temperature-wavelength coefficients for both FBGs are measured.

The Bragg wavelengths of both 2 FBGs monotonically increased with range of about 13 pm during the experiments (24 hours). This drift of wavelength is obviously caused

by the environmental temperature change. Meanwhile, the wavelength difference between the two FBGs monotonically decreased. This is probably caused by the tiny different temperature-wavelength coefficient of the FBGs, and can be completely removed if the temperature-wavelength coefficients are measured for both FBGs. But limited by the experimental conditions, we use another method to remove the temperature compensation dependence.

We regard the measured Bragg wavelength difference between the two FBGs as a vector with a dimension of 286 (the length of the data) labeled as $\vec{\lambda}_{diff}$. This vector is the sum of two 286-dimension sub-vectors

$$\vec{\lambda}_{diff} = \vec{\lambda}_{tem} + \vec{\lambda}_{str}. \tag{2.21}$$

$\vec{\lambda}_{tep}$ is caused by the temperature change, and it is a linear function of the temperature which is obtained by the center Bragg wavelength of the reference FBG $\vec{\lambda}_{ref}$

$$\vec{\lambda}_{tem} = k \cdot \vec{\lambda}_{str}, \tag{2.22}$$

where *k* is a constant. $\vec{\lambda}_{str}$ is caused by strain (the random noise of the sensor in this case, which determines the resolution of the sensor). The two sub-vectors are independent with each other, so their inner product should be zero,

$$\left\langle \vec{\lambda}_{tem} \cdot \vec{\lambda}_{str} \right\rangle = 0. \tag{2.23}$$

From the above equations we get the following equations after some linear algebra operation

$$\vec{\lambda}_{Str} = \vec{\lambda}_{diff} - \frac{\left\langle \vec{\lambda}_{diff}, \vec{\lambda}_{ref} \right\rangle \vec{\lambda}_{ref}}{\left\| \vec{\lambda}_{ref} \right\|^2}. \tag{2.24}$$

Then the strain resolution is obtained by calculation of the standard deviation of the calculated $\vec{\lambda}_{str}$. The method gives a simple way to remove the temperature dependence from the measured Bragg wavelength difference, and has better effect when the dimension of data increases.

Fig. 3-4 shows the Bragg wavelength difference between FBGs after removing the temperature dependence. The standard deviation is improved to 3.1 fm. Consider a strain sensitivity of FBG of approximately 1.2 pm/με, a corresponding strain resolution of 2.6 nε is achievable if the sensor head is properly designed.

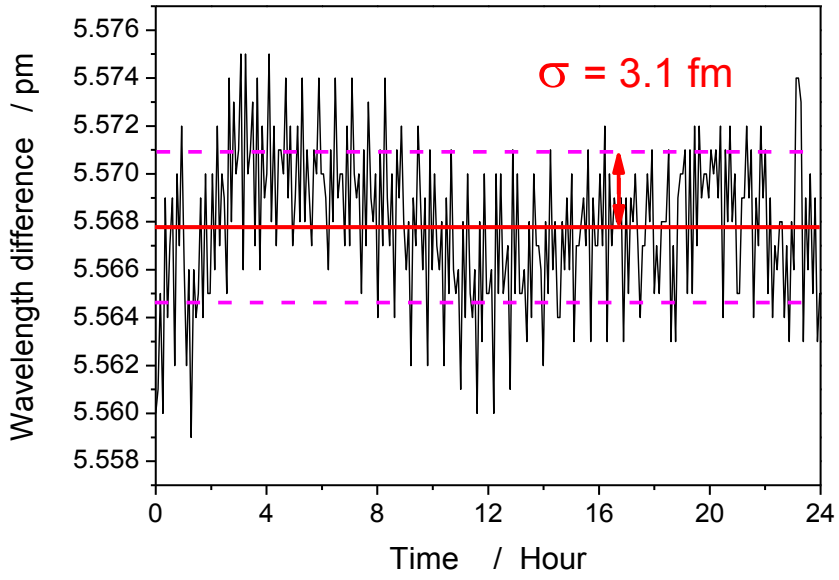

Fig. 3-4 Bragg wavelength difference after further temperature compensation

We also compare the results using other data algorithms for calculation of Bragg wavelength between the FBGs, including CDA and LSQ curve fitting algorithm. The calculated Bragg wavelength difference with the the two algorithms are shown in Fig. 3-5. The tepmperature dependence has been removed in the curves of Fig. 3-5.

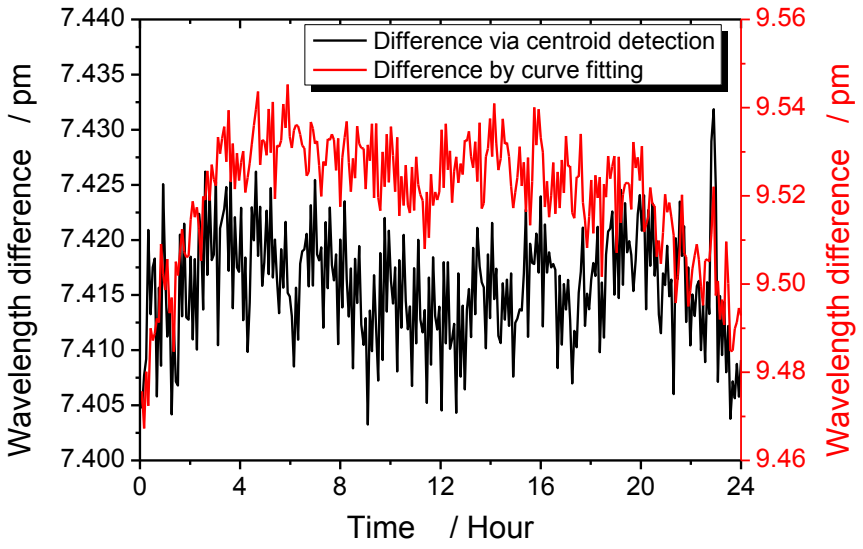

Fig. 3-5 Calcuated wavelength difference with different data processing algothrims.

The mean wavelength of different algorithms is slight different. This is not a problem as long as all of the data is processed using the same algorithms. Instead, the fluctuation range is important because it determintes the resolution of the algorithm. The wavelength standard deviation of different algorithms is shown in Table 2. The result indicts that the cross-correlation algorithm provides the best resolution.

Table 2 Calculated wavelength resolutions of different demodulation algorithms

Algorithm	Cross-correlation	CDA	LSQ fitting (Gaussian)
Standard deviation (nε)	2.6	4.3	11.7

3.1.3 Discussion and improvements

Acceding to the analysis in chapter 2, the resolution of this sensor is caused by the intensity noise in the measured reflection and the wavelength repeatability of laser. According to the parameters in Table 1, the contribution of intensity noise and wavelength repeatability is 0.18 nε and 2.3 nε, respectively. Obviously the wavelength

repeatability is the dominant noise in the sensor. According to the analysis, broader bandwidth FBGs can achieve better resolutions with the current laser and power-detectors. The optimized bandwidth of FBG is calculated to be 0.7 nm using Eq. (2.19). The bandwidth is too large to be fabricated in practices. In our following research FBGs with broader bandwidth of 0.23 nm are employed. Meanwhile, as the wavelength repeatability plays the dominant role in the resolution of sensor, even the intensity noise increase by 10 dB, its contribution to resolution is still smaller thant that caused by the wavelength repeatability. In the following experiments, a continuous sweep mode is used instead of the step sweep mode for the tunable laser. The influence of intensity noise level is still less than that of the wavelength repeability, but the measuring period is greatly reduced from 5 minutes to several seconds.

3.2 Lab experiment with strain applied

A piezo stage is employed to apply a variable strain to the sensing FBG in laboratory, and the performance of the sensor is verified with this stage..

3.2.1 Modification of configuration

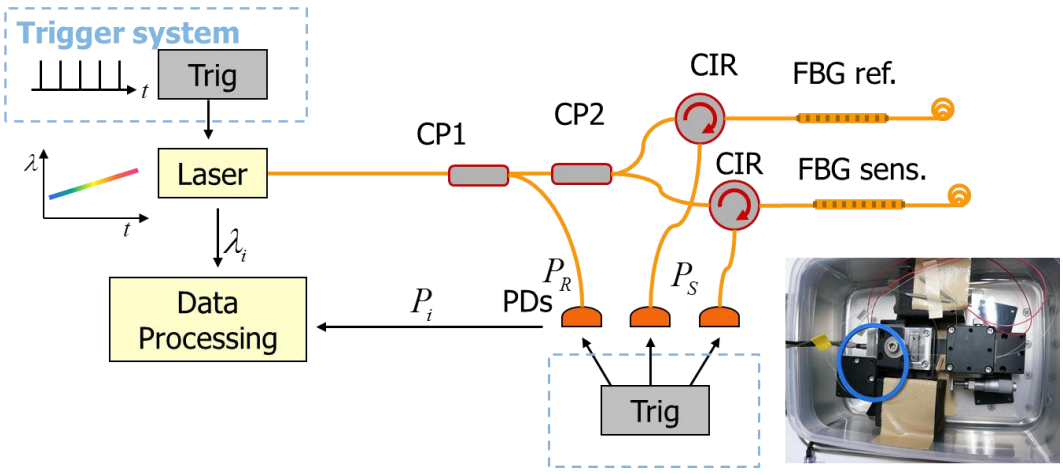

Fig. 3-6 Configuration of FBG interrogation. Inset: FBG and piezo-stage.

The system configuration is based on the initial experiments with increased sensing speed, as shown in Fig. 3-6. The laser works in continuous sweep mode with speed of 500 pm/s. As the laser suffers from power fluctuation during the relative high sweep speed, a coupler (CP1) is employed to couple part of the laser to a third power-detector for ratio power detection. During the laser wavelength sweeping, a trigger system produces a serious of trigger signal for the tunable laser and power-detectors. At each trigger, the corresponding wavelength of tunable laser and the measured power of photo-detectors are recorded. After the sweep of laser completes, cross-correlation algorithm is used to calculate the Bragg wavelength difference. The data processing is shown in Fig. 3-7. After a certain number of sweeps, the laser will carried out a wavelength calibration. The whole processing is realized using LabVIEW program running on a personal computer.

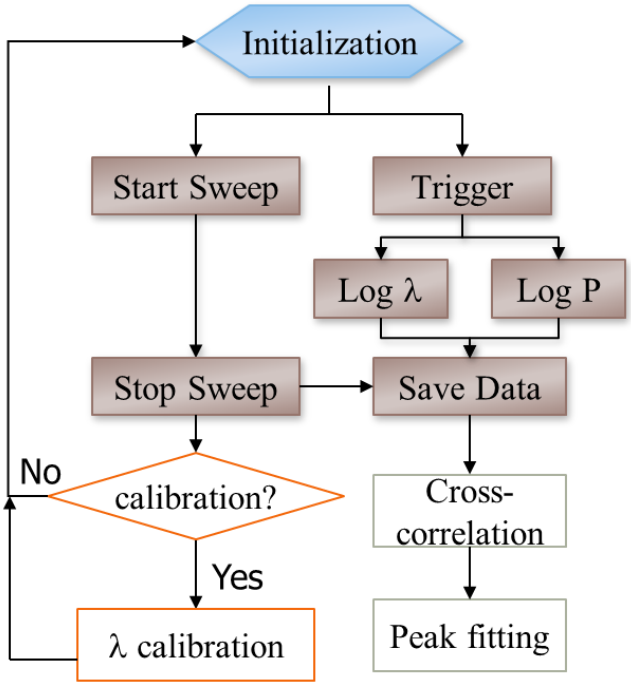

Fig. 3-7 Processed of experiment

The testing stage is shown as the inset in Fig. 3-6. The sensing FBG is mounted between a piezo-stage (PI, 752) and a manual stage, while the reference FBG is

mounted between a fixed stage and the same manual stage. The piezo-stage is controlled by computer directly via a piezo-driver (PI, E625). The applied strain by piezo-stage switched between 0 and 100 nε every five measurements (20-second interval between two measurements). The measurement was repeated for 1000 times lasting 5 hours.

3.2.2 Experimental results and discussion

The typical measured data is shown in Fig. 3-8. The blue line is the applied strain by piezo-stage, and the black line is the measured Bragg wavelength shift caused by strain. The measured wavelength shift followed well the variation of applied strain. According to the experimental data, a strain resolution of 17.6 $n\varepsilon$ is demonstrated.

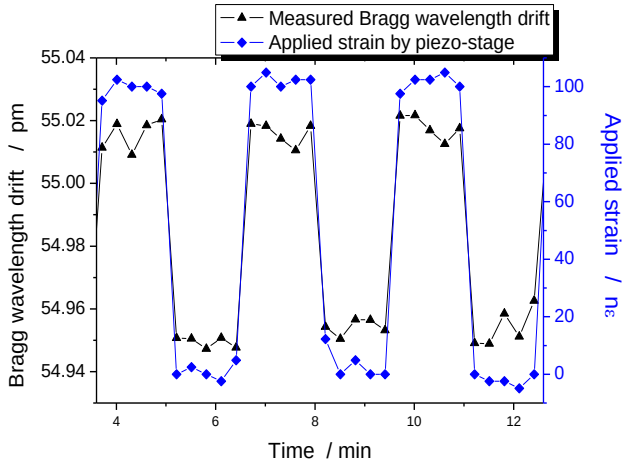

Fig. 3-8 Measured wavelength shift vs. Applied strain

Compared with the resolution when no strain applied, the strain resolution in Fig. 3-8 degraded from 2.6 nε to 17.6 nε. The resolution is believed mainly affected by the precision of the piezo-stage, which is not stable enough during experiments. Better resolution is expectable with a more precise strain supplied. This is the first time that a real static strain resolution on 10 nε order was experimentally demonstrated.

3.3 In-door verification of the FBG sensor

With the proposed FBG sensor, strain resolution down to 17.6 nε was demonstrated at laboratory, which meets the required strain resolution for some geophysical applications. Before the sensor was put into practices, it was tested by in-door experiments to verify its performances under field experiments.

3.3.1 Experimental setup

3.3.1.1 Design of testing stage

The schematic diagram of the experiment is shown in Fig. 3-9 Setup of testing stage for in-door experimentsFig. 3-9. A concrete cube with side length of 60 cm is built to model the crock of the earth. The cube is placed in a firm steel frame. Two pairs of oil expanded beds connected with hydraulic circuits are installed between the concrete cube and the steel frame, providing independent variable pressure in two directions, respectively. On the up surface of the concrete cube, two types of FBG sensors are mounted. Several strain gauges are adhered on the surface of the cube for reference. Thermal sensors are also used to measure the temperature fluctuation of environment. The pressures of the oil expanded beds are monitored by pressure meters.

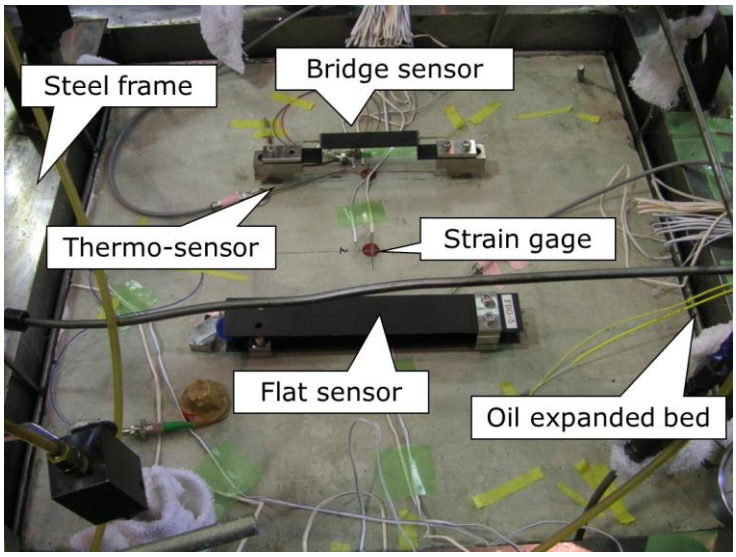

Fig. 3-9 Setup of testing stage for in-door experiments

3.3.1.2 FBG sensors packaged with CFRP

The package of the sensing fiber is an important issue for the practical sensors. In the experiments, carbon fiber reinforced plastics (CFRP) is used for the package of FBGs. CFRP has the advantages such as light weight, strong, easy of shape, similar thermal expansion coefficient with glass [33], so it is a potential material for fiber sensor head with the ability of easily embed fiber inside. In the experiments two types of sensor heads are tested. The first type is flat CFRP plate with one FBG embedded in side, as shown inFig. 3-9. Both ends of one flat CFRP working for strain sensing is fixed on the concrete by two steel sticks, which is inserted until the middle of the concrete cubic, while another CFRP plate is mounted above it and with one end free working for reference.

The other type of sensor heads is a bridge-shaped CFRP structure with two FBGs embedded inside, as shown in Fig. 3-10. The two FBGs are symmetrical placed in the beam of the bridge, and the two piers of the bridge are fixed on the concrete cube. When the concrete is pressed / strained, the beam will bend accordingly, the above FBG will be stretched / compressed, and the lower FBG will be the opposite. Thus the Bragg wavelength difference reflects the direction and amplitude of the deformation. This structure is expected to measure strain of both stretching and compressing.

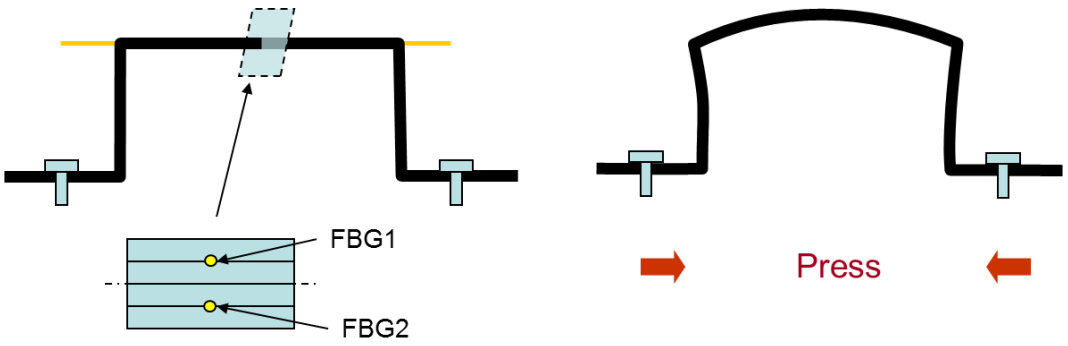

Fig. 3-10 Structure of bridge-shaped CFRP FBG sensor

3.3.2 Experimental results and discussion

The target of the experiments is to check the performance of the sensing system under field environment. However, the experimental results are not satisfaction due to some failures in the modeling of environments, as analyzed in the following sections.

3.3.2.1 Quick fluctuation of ambient temperature

The geophysical sensors are mounted underground in an enclosed space with a very stable temperature, varying less than 0.5 ℃ over a year. But in the in-door experiments, the temperature fluctuation range is larger than 1 ℃ within a day. The quick change of temperature produces a temperature gradation in the concrete cube, which results in nonlinear additional deformation into the FBG sensors due to the thermal-expansion of the concrete.

3.3.2.2 Nonlinear thermo parameters of CFRP

The FBGs have perfect thermal-wavelength linearity within a large temperature range. However, in the in-door experiments the CFRP-packaged FBG sensors exhibits hysteresis loop in the thermal-wavelength response. As the CFRP is a new-developed synthetic material, its properties under extreme conditions are not proved yet. In our following research the FBGs are packaged using traditional methods.

Although the testing stage and the packages of the FBGs meets some problems, the interrogation system for the sensor shows expected performance. Part of the measured data from bridge-shaped CFRP sensor is shown in Fig. 3-11 (a). The concrete cube is compressed by the oil expanded beds, and its strain is measured simultaneously by the CFRP sensor and strain gages. The insert in Fig. 3-11 (a) is the pressure of the oil. Obviously the wavelength shift varied in the same pattern as the measured data of strain gage. The slight difference is supposed to be caused by the different mounting methods. By comparison of the two data, the sensitivity of the FBG in CFRP sensor head is 0.043 pm/με, which is much smaller than that of unpackaged FBG (approximately 1.2 pm/με).

This type of sensor head is suitable for applications that a very large measurement range is required.

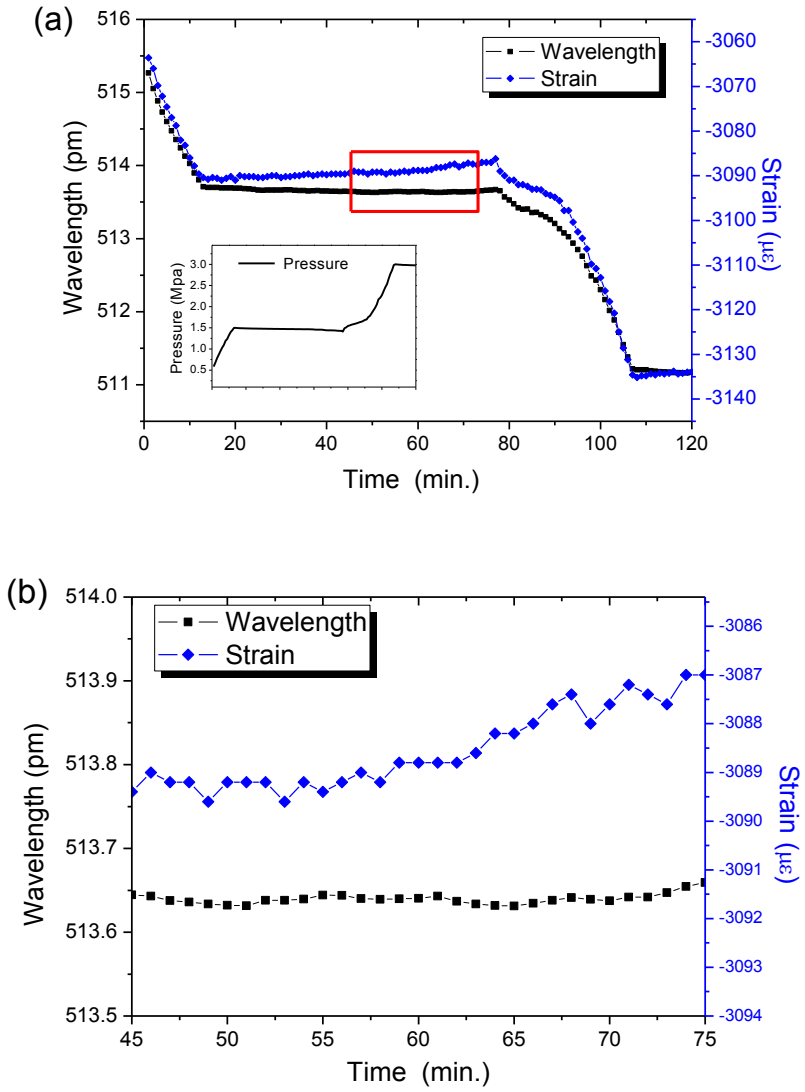

Fig. 3-11 Experimental results of in-door experiments. (a) Measured wavelength shift of FBG and data of strain gage. (b). Part of the data in (a).

Fig. 3-11 (b) shows a comparison of part of the measured data of the FBG sensor and the strain gage, which is within the red rectangle in Fig. 3-11 (a). The FBG sensor shows much better resolution than that of the strain gage. Notice that this is achieved with a sensor head that has strain transmission coefficient of only 0.036. The

wavelength resolution of FBG sensor is calculated to be better than 10 fm, which indicts a strain resolution on the order of 10-nε is achievable with a common sensor head design, just as we have demonstrated in Lab experiments.

3.4 In situ experiments

Finally the sensor was put into practices to measure the crustal deformation induced by oceanic tide at Aburatsubo Bay, Kanagawa, Japan.

3.4.1 Background of the experiments

The crustal deformation induced by oceanic tide provides important information for geophysical research. Geophysical sensors are set for the measurement of coastal deformation at Aburatsubo Bay, Japan, which is located in the southwestern part of Miura Peninsula about 60 km southwest of Tokyo and is surrounded by sea except on its northern side, as shown in Fig. 3-12. Vaults with several sections is built 1.5 m above the sea level and situated under a cliff about 10 m high. As the oceanic tide level varies, the pressure of sea to the coast changes accordingly, resulting in deformation to the crust of earth. Silica cube extensometers with length of 38 m are installed in Vault A for the strain measurement. This type of sensors has good performance, but also has some drawbacks. First, the adoption of the extensometer is very expensive. This cost includes not only the price of the extensometer itself, but also the engineering for its installation. A huge vault is necessary to accommodate such a long extensometer. Second, the measured strain of the extensometer is the accumulated strain over its length. The special resolution is limited by its length. They are not able to provide the distribution of strain with better special resolution. New strain sensor with low cost, small size and ultra-high strain resolution is desired for the such applications. For this reason, we started a project to measure the deformation of the coastal using FBG sensors. We mounted two sets of FBG strain sensors inside the vault, label as No. 1 and No. 2 in Fig. 3-12, to measure the same strain information.

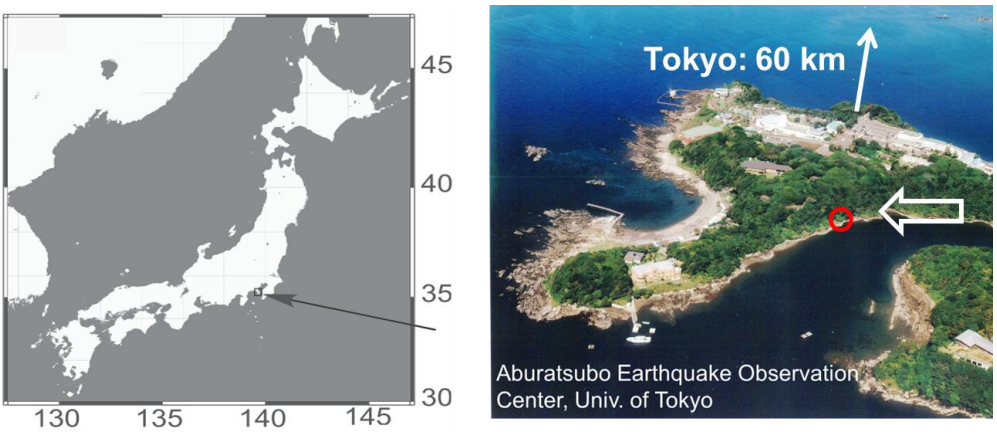

(a)

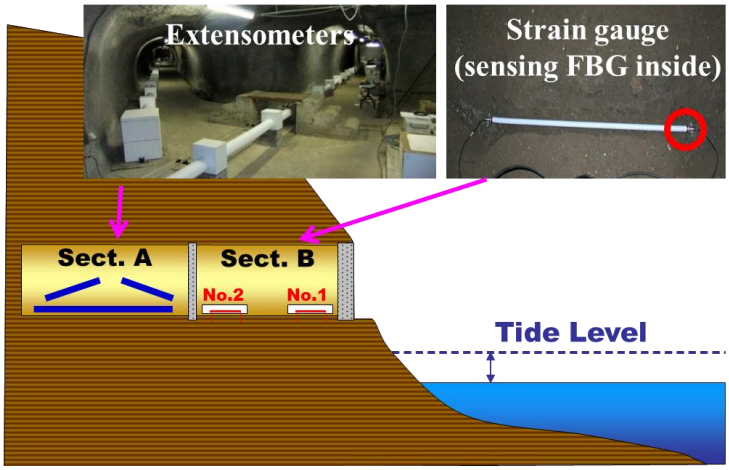

(b)

(c)

Fig. 3-12 The configuration for measurement of crustal deformation induced by oceanic tide. (a), position of the Aburatsubo Bay; (b), the configuration of the valult with extensomters and FBG sensors insides; (c), the installation of the FBG sensors. The sensing FBG is integrated in strain gauge (Micron optics, os3600), and the reference is strain free close to the strain gauge under the same cover.

3.4.2 Configuration of FBG strain sensor

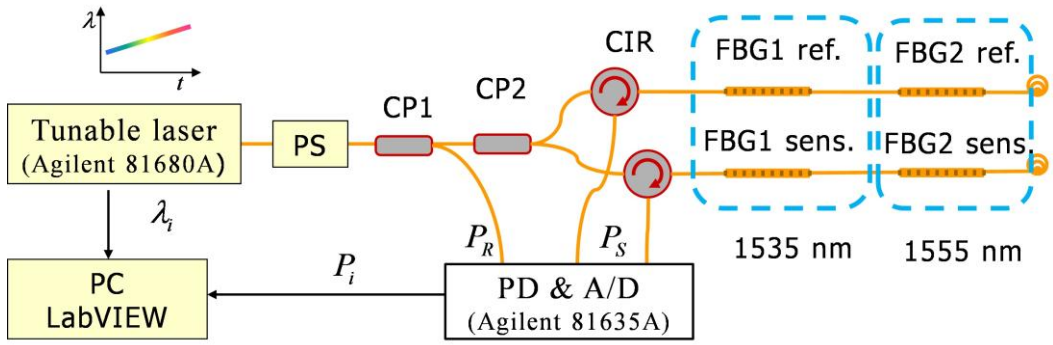

Fig. 3-13 Schematic of multiplexed FBG sensor for in situ experiments. PS, polarization scrambler.

The system configuration is shown in Fig. 3-13. Compared with the lab experiments, a polarization controller (PS) was employed to eliminate the influence of the polarization unstable. The center wavelengths of the two sets of FBG are 1535 nm and 1555 nm, respectively. Wavelength division multiplexing (WDM) technology is used to interrogate the FBGs with one tunable laser and one set of power-detectors. The whole processing is controlled by a LabVIEW program running on a laptop computer. The sensor could work for months without maintaining.

3.4.3 Experimental results

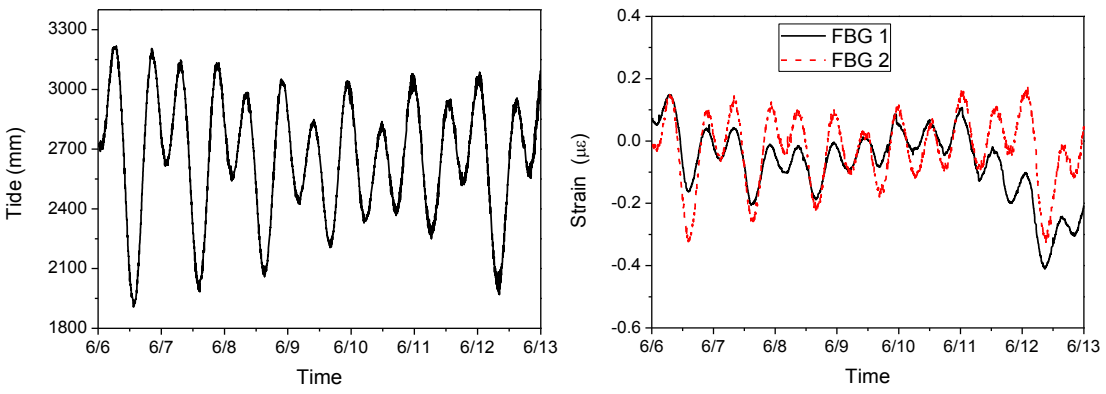

(a) (b)

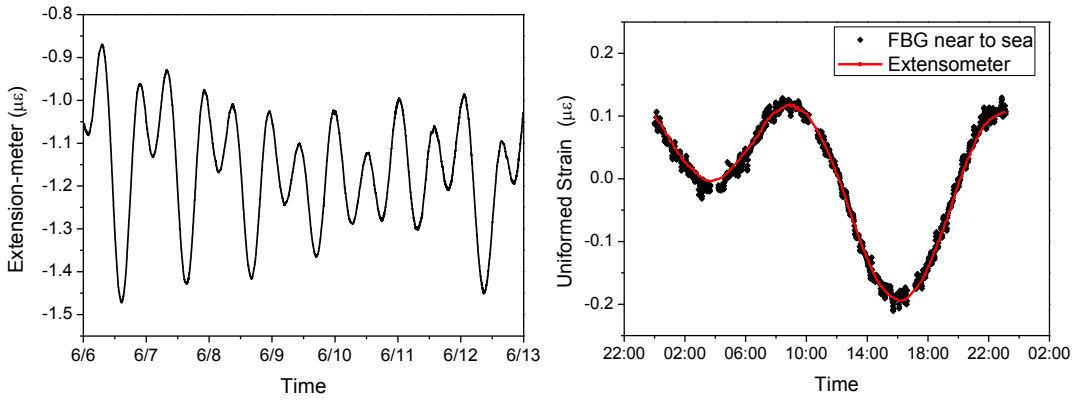

(c) (d)

Fig. 3-14 In situ experimental results. (a) Oceanic tide level; (b) Measured strain of FBG sensors; (c) Measured strain of one extensometer; (d) Comparison of measured strain of extensometer and FBG No.2 on Jun. 8, 2011..

Fig. 3-14 (a) and (b) illustrate part of the oceanic tide level and the measured strain of FBGs, respectively. The measured strain of FBGs have similar shape as the oceanic tide level, indicts that the deformation induced by oceanic tide is clearly observed with strain amplitude less than 1 με. The different amplitude between the two FBG sensors in Fig. 3-14 (b) is possibly caused by their different distance from the coastline, reflecting the feasibility of measuring the deformation distribution with high spatial resolution and low cost. Fig. 3-14 (c) is the data from the 38 m long extensometer, which works as the standard of the strain signal. Although the measured strain information is slightly different for the extensometer and FBG sensors due to the different mounting method and position, the extensometer is effective to evaluate the resolution of the FBG sensors. Fig. 3-14 (d) plots the comparison of strain signals between the FBG 2 and the extensometer, which amplitude is zoomed by a factor of 0.76. The measured strain of FBG sensor fluctuates around that of the extensometer with a standard deviation of 9.8 nε, indicts that a 10 nε strain resolution of the FBG sensor is obtained with this sensor. This is the first in situ demodulation of 10 nε order static strain resolution with FBG sensors.

Compared with extension-meters, FBG sensors have comparable strain resolution, but the much smaller size. The small size not only reduces the difficulty and cost for mounting, but also making the quasi-distributed static strain measurement possible. t And the FBG sensor system is robust and could work for months without maintenance. The above characteristics make our FBG sensor a powerful tool for the geophysical applications

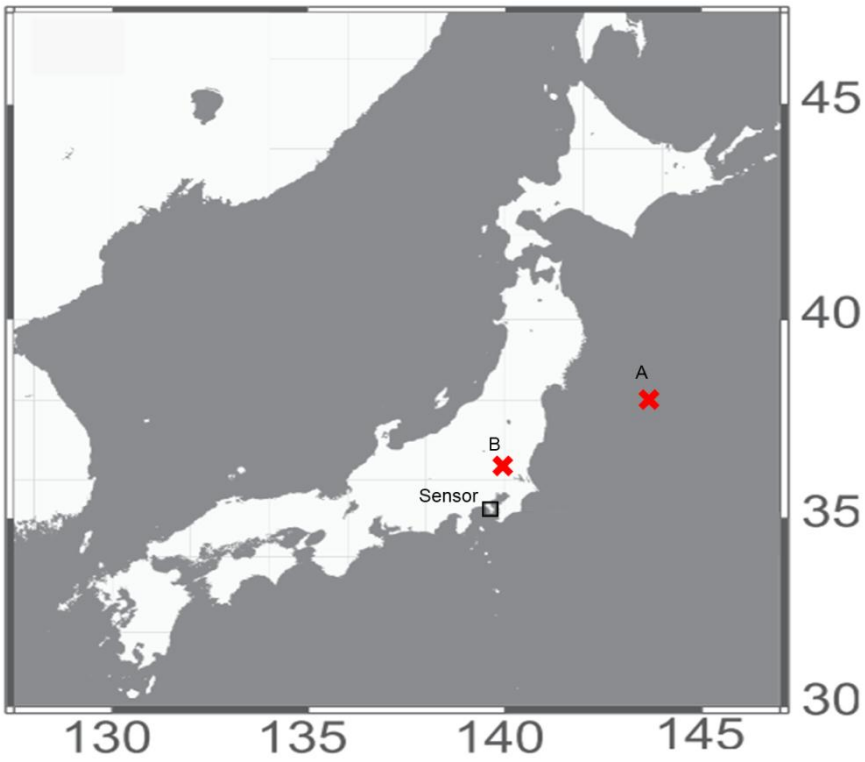

Fig. 3-15 Spot of earthquake and sensor. Sensor is at Aburatsubo Bay;

During the measurements, strain changes deduced by earthquake are also recorded. On Jul. 10, 2011, an earthquake of M7.1 occurred at Sanriku coast (N38°, E143.5°), about 500 km from Aburatsubo Bay, as the x mark labeled A in Fig. 3-15. The Japan Meteorological Agency (JMA) seismic intensity scale at Aburatsubo is 2, corresponding to a ground quake that most people indoors can feel [34]. The measured strain around the earthquake is shown in Fig. 3-16 (a). Another earthquake of M5.5 happens on Jul. 15, 2011, an earthquake occurred at Ibaraki (N36.3°, E140.1°), about 150 km from the

sensor, as the x mark labeld B in Fig. 3-15. The data of the FBG sensor is shown in Fig. 3-16 (b). During the earthquakes, both the disturbance during earthquake and the permanent strain shift are observed, providing meaningful data for geophysical research.

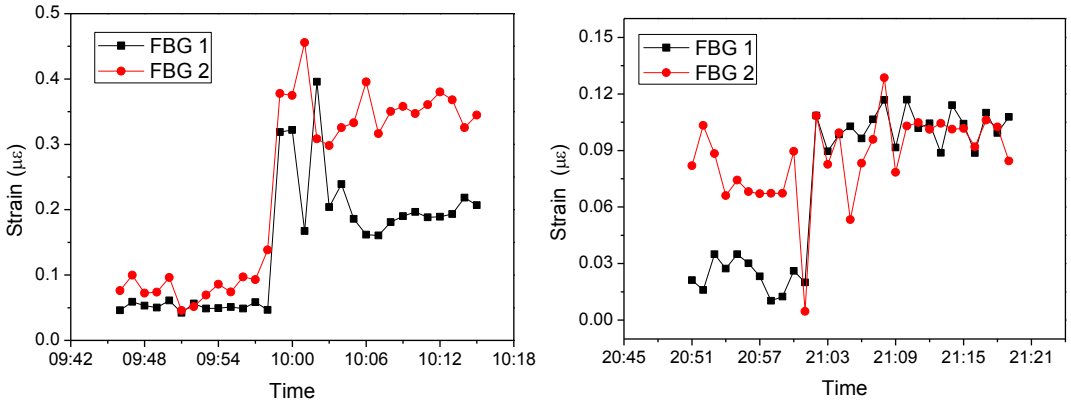

(a) (b)

Fig. 3-16 Measured strain of in situ FBG sensors around earthquakes. (a) Earthquake of M7.1, 500 km away; (b) Earthquake of M5.5, 150 km away.

3.5 Conclusion

In this chapter, practical FBG static strain sensors interrogated by narrow linewidth tunable laser is built and tested. In the initial experiments, both of the FBGs are free from strain to ascertain the ultimate resolution of the interrogation system could achieve. Ultra-high wavelength resolution corresponding to a static strain resolution of 2.6 nε is obtained. Then the systemic configuration is improved for a higher measuring speed, and a piezo-stage is employed to provide a variable strain to the sensing FBG. A strain resolution of 17.6 nε is demonstrated, mainly limited by the precision of the testing stage. The sensor is further tested in an in-door experiment to verify its performance, and the wavelength resolution is proved. Finally, the sensor is used to monitor the crustal deformation induced by oceanic tide at Aburatsubo Bay, Kanagawa, Japan. The crustal strain is clearly observed with static resolution of 10 nε, which is comparable with the resolution of 38 m long extension-meters. This is the first in situ

demomstration of 10 nε order static strain resolution with FBG sensors, providing a powerful tool for the measurement in geophysics applications.

Chapter 4.

Static strain FFPI sensors with frequency modulation technique

In our previous work, we realized an ultra-high resolution static strain sensor with a pair of FBG sensors interrogated by a narrow linewidth tunable laser. A static strain resolution down to nε order with a large dynamic range was demonstrated in experiments. According to the analysis on the resolution of this type of sensors, the sensor's performance is mainly limited by the laser's wavelength repeatability during the sweeping. The bandwidth of practical FBG falls on the range from tens to hndardes of pm, and the tunable laser has to cover the spectra of both FBGs. In our previous FBG sensors a mechanically-tuned external cavity diode laser is used as the optical source. Although this laser is suitable for multiplexed sensing with WDM technology because of its large tunable range, it is hard to further improve its wavelength repeatability.

In this chapter, we report a fiber optic static strain sensor using a pair of fiber Fabry-Perot interferometers (FFPIs) as the sensor heads. A frequency modulation (FM) technology is employed in the interrogation of the FFPIs in digital domain. The wavelength sweeping range of laser is only 5 pm, finely tuned by a piezo-stage, to scan the spectra of the FFPIs. A cross-correlation algorithm is used to extract the resonance difference between the two FFPIs with high precision. The principle and configuration of FM interrogation technology and the experimental results are discussed.

4.1 Fabry-Perot interferometer

The Fabry–Perot interferometer (FPI) is typically formed by placing two reflecting boundary such as a pair of parallel highly reflecting mirrors or two FBGs in one fiber. It is named after Charles Fabry and Alfred Perot.

4.1.1 Spectrum of FPI

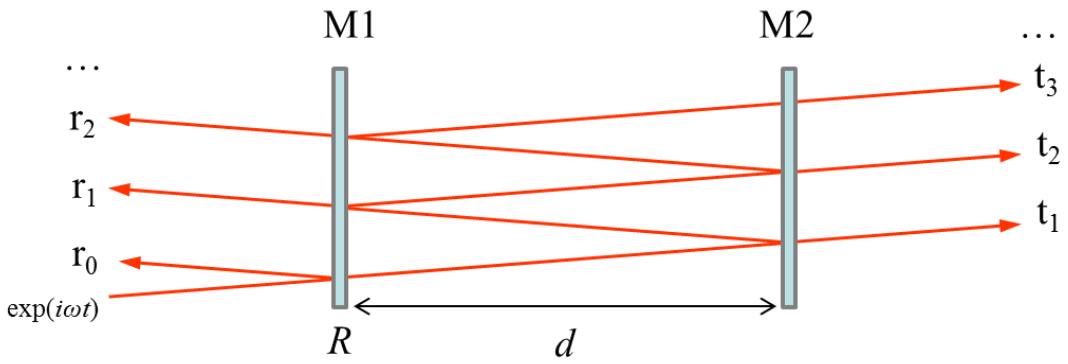

Fig. 4-1 Structure of Fabry-Perot interferometer

The structure of typical FPI is shown in Fig. 4-1. The two parallel mirrors, M1 and M2, are separated by distance of *d*. Both mirrors have light intensity reflection of *R*.

The incident lightwave has form of $e^{i\omega t}$, where ω is the radian frequency. As shown in Fig. 4-1, The beam that reflects from the FPI is actually the coherent sum of two different beams: the promptly reflected beam which bounces off the first mirror and never enters the cavity, labeled as r_0; and a leakage beam, which is the small part of the standing wave inside the cavity that leaks back through theM1, as shown the sum of r_k where $k \geq 1$.

The transmission of incident beam on M1 is expressed as $\sqrt{1-R}\cdot e^{i\omega t}$, or $\sqrt{1-R}$ by omitting the $e^{i\omega t}$ term. The promptly reflected lightwave is

$$r_0 = -\sqrt{R}, \tag{4.1}$$

where $\sqrt{R}$ is the complex amplitude reflection of M1. The negative sign describes the half-wave loss during the reflection.

The leaked light from the Fabry-Perot cavity through M1 is expressed as

$$r_k = (1-R)\cdot R^{k-0.5}\cdot e^{ik\varphi} \tag{4.2}$$

$$\varphi = \frac{2nd\omega}{c} = \frac{\omega}{v_{FSR}} \tag{4.3}$$

In the equation, n is the index of the cavity, c is the speed of light in vacuum, V_{FSR} is the free spectrum range (FSR) of the interferometer, V_{FSR} = c/(2nd), and k ($k \geq 1$) is an integer. Here φ is the phase change for the light wave-form to travel a round trip between the mirrors.

Thus we have the complex amplitude reflection of Fabry-Perot interferometer:

$$F(\omega) = \sum_{k=0}^{\infty} r_k = -\sqrt{R} + \frac{(1-R)\sqrt{R}\cdot e^{i\varphi}}{1-\mathrm{R}\,e^{i\varphi}} = \frac{\sqrt{R}\left(1-e^{i\varphi}\right)}{1-\mathrm{R}\,e^{i\varphi}}. \tag{4.4}$$

The promptly reflected beam and the leaked beam have the same frequency, and their intensities are almost the same near resonance. Their relative phase, however, depends strongly on the frequency of the laser beam. If the laser's frequency is exactly an integer multiple of the cavity's free spectral range, then the promptly reflected beam and the leakage beam have the same amplitude and are exactly 180° out of phase. In this case the two beams interfere destructively, and the total reflected beam vanishes. If the laser's frequency is not exactly an integer multiple of the free spectral range but close enough to build up a standing wave, then the phase difference between the two beams will not be exactly 180°, and they will not completely cancel each other out [35]. Some light gets reflected off the cavity and its phase depends on which side of resonance the laser is on. From Eq. (4.4) we can get the intensity reflection and phase change of light when reflected by the Fabry-Perot interferometer.

Finesse of the interferometer relates the full-width at half maximum (FWHM) of the transmission of the Fabry-Perrot cavity with its free spectrum range. It is defined as

$$\mathcal{F} = \frac{\nu_{FSR}}{\delta_{FWHM}} \approx \frac{\pi\sqrt{R}}{1-R}. \tag{4.5}$$

The approximation is satisfied for $R > 0.5$.

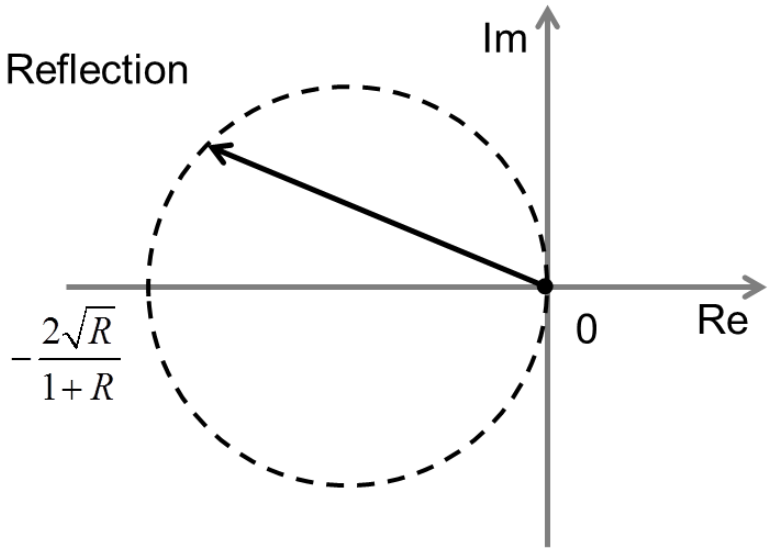

Fig. 4-2 The reflection coefficient in the complex plane.

It is helpful to study the properties of $F(\omega)$ in the complex plane. $F(\omega)$ is a circle in the complex plane, as proved by the following equation:

$$\left|F(\omega)+\frac{\sqrt{R}}{1+R}\right| = \left|\frac{\sqrt{R}}{1+R}-\frac{\sqrt{R}\left(1-e^{i\varphi}\right)}{1-Re^{i\varphi}}\right| = \left|\frac{\sqrt{R}}{1+R}\cdot\frac{e^{i\varphi}-R}{1-Re^{i\varphi}}\right| = \frac{\sqrt{R}}{1+R} \tag{4.6}$$

As shown in Fig. 4-2, $F(\omega)$ lies on a circle in the complex plane, centered on the real axis, with ω being the parameter the position of F in the circle. $|F(\omega)|^2$ gives the intensity reflection of the beam. F is symmetric around resonance, but its phase is different depending on whether the laser's frequency is above or below the cavity's resonance. As ω increases, F advances counterclockwise around the circle. This circle intersects the origin, with F=0 on resonance. Very near resonance, F is nearly on the

imaginary axis, being in the lower half plane below resonance and in the upper half plane above resonance. This graphical representation of F in the complex plane helps to understand the results of quantitative model.

4.1.2 FFPI strain sensor

The analysis on the strain/temperature sensitivity of FBG in chapter 2 also works for the FFPI. The strain induces the resonance shifts of both FBG and FFPI in the same way via the physical elongation of the fiber (also via the change of the refractive index to a much smaller extent) [36]. Just like the FBG, FFPI can also be used for ultra-high resolution strain sensing with temperature compensation. The main difference is that the FFPI has a serious of resonances with interval of V_{FSR}, and the bandwidth of resonance is much narrorer than FBG. For commom FBG, the bandwidth is in the region of 10 pm – 1 nm, but bandwidth of FFPI can be smaller than 10 fm.

The strain resolution of FFPI sensor also depends on the precision in the measurement of the resonance frequency. To measure the resonance of the FFPI, one method is to measure the reflection of the FFPI, and the frequency that has minimum reflection is the resonance, as has been done for the FBG sensor. However, because the bandwidth of FFPI falls into the region of radio frequency (RF), the FFPI can be interrogated by a more efficient frequency modulation technique using RF technique.

4.2 Frequency modulation (FM) interrogation technology

The reflection method does works as we have done on the FBG sensors. Because the bandwidth of FFPI falls into the RF region, a more effective interrogation technology to detect the resonance by measurement of phase reflection of the FFPI becomes possible via a frequency modulation (FM) configuration.

Although it is impossible yet to build electronics that can directly measure the electric field and hence the phase of a lightwave, the FM interrogation technology

provides a way of indirectly measuring the phase. The basic principle is to modulate the frequency of the laser with a RF sine function, and then compare the phase of reflected power with the RF sine function.

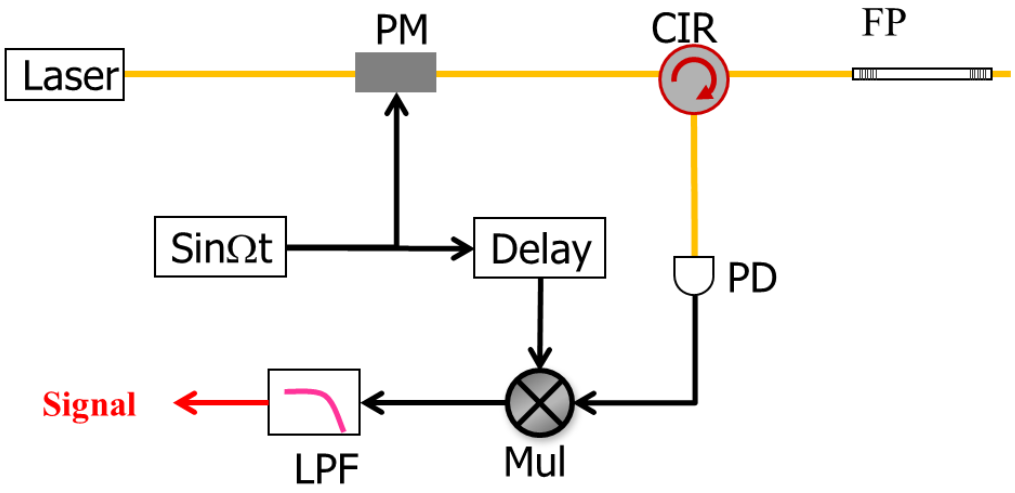

Fig. 4-3 Configuration of FM interrogation technology. PM, phase modulator; CIR: circulator; PD, photo-diode; Mul: multiplier, LPF, low pass filter.

The configuration for the FM interrogation technology is shown in Fig. 4-3. The output of narrow linewidth laser is passed through a phase modulator driven sinusoidal at RF Ω to produce a frequency modulated optical spectrum. The beam is reflected by the Fabry-Perot cavity and impinges on a fast respond photo-diode. The Fourier component of the photo-diode electrical signal at frequency of Ω is detected using a standard RF demodulator formed by a multiplier and low pass filter [37].

4.2.1 Conceptual model of FM interrogation technology

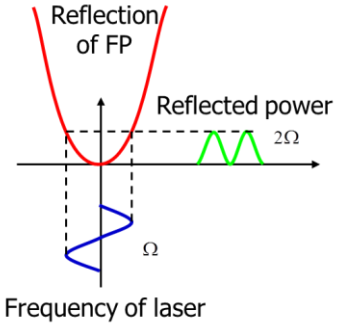

(a)

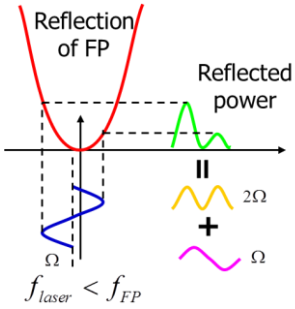

(b)

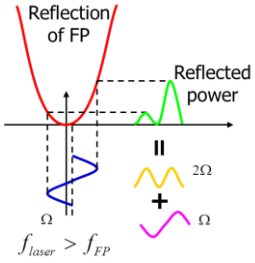

(c)

Fig. 4-4 Interrogation of FPI with FM technology. (a). Laser frequency lies at the resonance of FPI. (b). Laser frequency is smaller than the resonance frequency of FPI. (c). Laser frequency is larger than the resonance frequency of FPI.

The principle of the FM interrogation technology can be understood in the following procedure. When the laser is phase modulated with radian frequency of Ω, the instant frequency of laser also varies with the frequency of Ω. If the center frequency of laser lies exactly at the resonance of Fabry-Perot cavity as shown in Fig. 4-4 (a), the reflected optical power is modulated with frequency of 2Ω and does not consist of Ω terms. Otherwise, if the laser frequency deviates from the resonance frequency of Fabry-Perot cavity, the reflected power will consist of Ω term as well as 2Ω term, as shown by (b) and (c) in Fig. 4-4. The phase of the Ω term in reflected power is determined by whether the laser frequency is larger or smaller compared with the resonance frequency of the FPI, and the amplitude indicts the how large the laser deviates from the resonance frequency.

4.2.2 Quantitative model of FM interrogation technology

A more quantitative way of thinking about this technology is following: Modulating the laser's frequency or phase will generate new frequency components (sidebands). All of the frequency components are reflected by the FP cavity, and they experience different amplitude reflection and additional phase delay. The sum will display a beat pattern at the modulation frequency, and we can measure the phase of this beat pattern. The phase of this beat pattern will tell us the phase of the reflected carrier [12].

The lightwave after PM has additional phase change

$$E_{in} = E_0 e^{i\omega t + i\beta \sin \Omega t}, \tag{4.7}$$

here Ω is the radian frequency for phase modulator and β is the phase modulation depth. It is expanded using Bessel functions

$$E_{in} \approx E_0 \left[J_0(\beta) e^{i\omega t} + J_1(\beta) e^{i(\omega+\Omega)t} - J_1(\beta) e^{i(\omega-\Omega)t} \right]. \tag{4.8}$$

Here only the first order sidebands appear in Eq. (4.8), because the contribution of higher order sidebands has similar shape but smaller amplitude to the extracted signals

compared with the response of the first order sidebands. Besides of the carrier, two sidebands appear. All of the three lightwaves are reflected by the Fabry-Perot cavity independently. The reflected beam is

$$E_{re} = E_0\left[J_0(\beta)F(\omega)e^{i\omega t} + J_1(\beta)F(\omega+\Omega)e^{i(\omega+\Omega)t} - J_1(\beta)F(\omega-\Omega)e^{i(\omega-\Omega)t} \right]. \quad (4.9)$$

The photo-diode actually measures the power of the reflected beam, which is

$$\begin{aligned} P_{re} &= |E_{re}|^2 \\ &= P_0\left[J_0^2(\beta)\cdot|F(\omega)|^2 + J_1^2(\beta)\cdot\left(|F(\omega+\Omega)|^2 + |F(\omega-\Omega)|^2\right)\right] \\ &+2P_0\cdot J_0(\beta)\cdot J_1(\beta)\cdot \mathrm{Re}\left\{F(\omega)\cdot F^*(\omega+\Omega) - F(\omega)\cdot F^*(\omega-\Omega)\right\}\cdot\cos(\Omega t) \\ &+2P_0\cdot J_0(\beta)\cdot J_1(\beta)\cdot \mathrm{Im}\left\{F(\omega)\cdot F^*(\omega+\Omega) + F(\omega)\cdot F^*(\omega-\Omega)\right\}\cdot\sin(\Omega t) \\ &+(2\Omega\ terms), \end{aligned} \quad (4.10)$$

here $P_0=|E_0|^2$, the $F^*(\omega\pm\Omega)$ is the complex conjugate of the reflection of Fabry-Perot cavity at $\omega\pm\Omega$.

The result displays a beat pattern with two frequencies. The Ω terms arise from the interference between the carrier and the sidebands, and the 2Ω terms come from the sidebands interfering with each other. We are interested in the terms that are oscillating at the modulation frequency Ω because they sample the phase of the reflected carrier. There are two terms in this expression: a sine term and a cosine term. Usually, only one of them will be important, and the other will vanish. Which one vanishes and which one survives depends on whether the modulation frequency is lower or higher compared with the bandwidth of the Fabry-Perot cavity. In either case, the resonance frequency and laser frequency can be compared precisely.

4.2.3 Demodulation configuration

The reflected power in Eq. (4.10) is detected with a quick response photo-diode, as shown in Fig. 4-3. The output of the photo-diode consists of all terms in Eq. (4.10), while only the coefficient of sin(Ωt) and cos(Ωt) terms are useful. The demodulation of

Ω terms is achieved using a multiplier (can be replaced by a mixer in practice, but the principle is the same) and a low pass filter. When a sine signal with frequency of Ω_0 multiplies with another sine signal

$$\sin\Omega t\cdot\sin\Omega_0 t=\frac{1}{2}\left[\cos\left(\Omega-\Omega_0\right)-\cos\left(\Omega+\Omega_0\right)\right]. \tag{4.11}$$

Thus the product contains signals at both the sum ($\Omega+\Omega_0$) and difference ($\Omega-\Omega_0$) frequencies. If Ω_0 is equal to Ω, as the case for detection of the sin(Ωt) term in our configuration, the cos($\Omega-\Omega_0$) term becomes a dc signal, and can pass through the low pass filter. All other terms have high frequencies after the multiplier and are isolated by the low pass filter.

If we multiply a sine and a cosine signal instead, we get

$$\sin\Omega t\cdot\cos\Omega_0 t=\frac{1}{2}\left[\sin\left(\Omega+\Omega_0\right)t-\sin\left(\Omega-\Omega_0\right)t\right]. \tag{4.12}$$

In this case, if $\Omega_0=\Omega$, the dc signal vanishes. In order to measure the coefficient of the sinΩt term, we have to a reference signal of sin(Ωt) to the multiplier. If we want to detect the cos(Ωt) term in the reflected beam, a cos(Ωt) reference signal is necessary. In practice, a phase shifter (a tunable delay line, for example) is used in the reference signal path to adjust the phase of the reference.

4.2.4 Low modulation frequency

When the modulation frequency Ω is smaller compared with the bandwidth of the Fabry-Perot cavity, the laser frequency varies slowly enough and the standing wave in the cavity can follow the frequency of change of the instantaneous frequency for incident beam. The instantaneous frequency of modulated laser is

$$\omega(t)=\frac{d\left(\omega t+\beta\sin\Omega t\right)}{dt}=\omega+\Omega\beta\cos\Omega t. \tag{4.13}$$

The reflected power is a function of the instantaneous frequency $P_{re}=P_0|F(\omega)|^2$. It is expended as

$$\begin{aligned} P_{re} &= P_{re}\left(\omega + \Omega\beta\cos\Omega t\right) \\ &= P_{re}\left(\omega\right) + P_0 \frac{d\left|F\left(\omega\right)\right|^2}{d\omega}\Omega\beta\cos\Omega t. \end{aligned} \tag{4.14}$$

The reflected power thus is expressed as

$$P_{re} = \left(cont\right) + P_0 \frac{d\left|F\right|^2}{d\omega}\Omega\beta\cos\Omega t + \left(2\Omega\ terms\right). \tag{4.15}$$

So for low modulated frequency, only the cosine term survives in the extracted signal. The extracted signal from low pass filter is

$$S = P_0\Omega\beta\frac{d\left|F\right|^2}{d\omega} \tag{4.16}$$

In case the beam frequency is very close to the resonance of the interferometer, ω is written as

$$\omega = 2k\pi\cdot\nu_{FSR} + \delta\omega, \tag{4.17}$$

here k is an integer, and $\delta\omega$ is small value ($\delta\omega\rightarrow 0$).

Now the reflection of Fabry-Perot cavity is simplified to

$$F\left(\delta\omega\right) \approx \frac{\sqrt{R}\cdot\delta\omega\cdot i}{\left(1-\mathrm{R}\right)\nu_{FSR}}. \tag{4.18}$$

Considering Eq. (4.5), Eq. (4.18) is becomes

$$F\left(\delta\omega\right) = \frac{i\delta\omega}{\pi\cdot\delta_{FWHM}}. \tag{4.19}$$

In the complex plane, $F\left(\delta\omega\right)$ is on the imaginary axis, agreeing with the tangential line of the circle in Fig. 4-2. By putting Eq. (4.19) into Eq. (4.15), we get the extracted signal as

$$S = \frac{2P_0\beta\Omega\cdot\delta\omega}{\pi^2\delta_{FWHM}^2} \tag{4.20}$$

The same conclusion can be obtained by putting Eq. (4.19) into Eq. (4.10) with approximation of $J_0(\beta) = 1$, $J_1(\beta) = \beta/2$, in agreement with the above analysis.

According to Eq. (4.20), the extracted signal is a linear function of the $\delta\omega$ around the resonance, and intersect zero when the laser lies exactly on the resonance frequency. A typical curve of the demodulated signal is shown in Fig. 4-5.

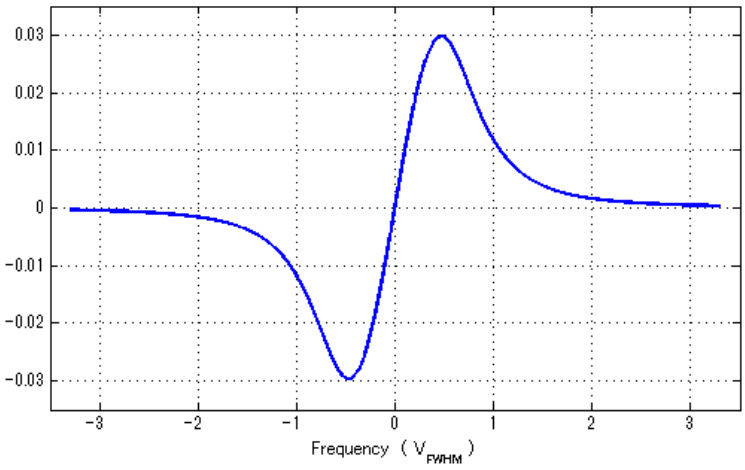

Fig. 4-5 Demodulated signal versue ω/V_{FWHM} when the modulation frequency is low. The modulation frequency is half of the V_{FWHM} of the Fabry-Perot cavity. The finesse of cavity is 300.

4.2.5 High modulation frequency

In the case that the modulation frequency Ω is high compared with the bandwidth of the Fabry-Perot cavity, the sideband frequency is outside of the bandwidth of the cavity when the carrier is near the resonance, $F(\omega \pm \Omega) \approx -1$. Then Eq. (4.10) is simplified to

$$P_{re} = (cons) - 4P_0 \cdot J_0(\beta) \cdot J_1(\beta) \cdot \mathrm{Im}\{F(\omega)\} \cdot \sin(\Omega t) + (2\Omega\ terms). \qquad (4.21)$$

Thus the cosine term is negligible, and the demodulated signal is

$$S = -4P_0 \cdot J_0(\beta) \cdot J_1(\beta) \cdot \mathrm{Im}\{F(\omega)\}. \qquad (4.22)$$

The demodulated signal is shown in Fig. 4-6.

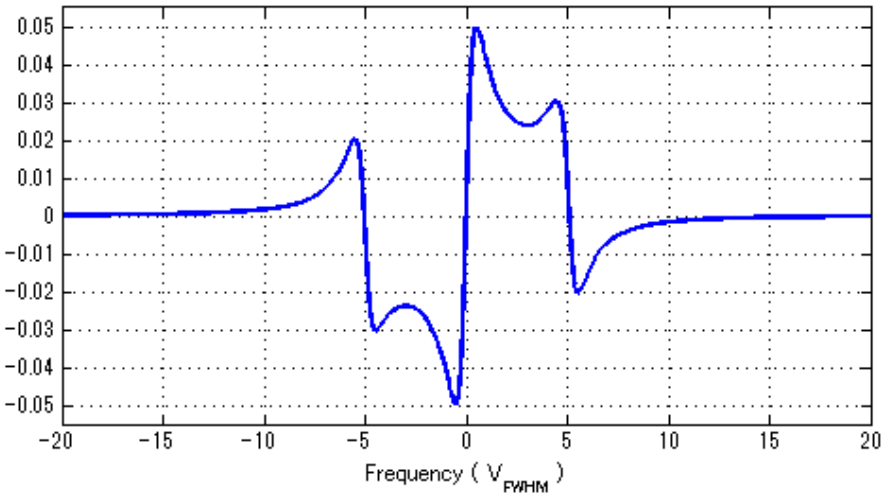

Fig. 4-6 Demodulated signal versue ω/V_{FWHM} when the modulation frequency is high. The modulation frequency is 5 time of the V_{FWHM} of the Fabry-Perot cavity. The finesse of cavity is 500.

From Fig. 4-6 it is found that the demodulated signal pass through zero at resonance, and is linear around the resonance. From Eq. (4.19) and Eq. (4.22), the demodulated signal around resonance is

$$S = -\frac{4P_0 J_0 \cdot J_1(\beta) \cdot \delta\omega}{\pi \cdot \delta_{FWHM}}. \tag{4.23}$$

4.3 Static strain FFPI sensor with FM technology

4.3.1 System configuration

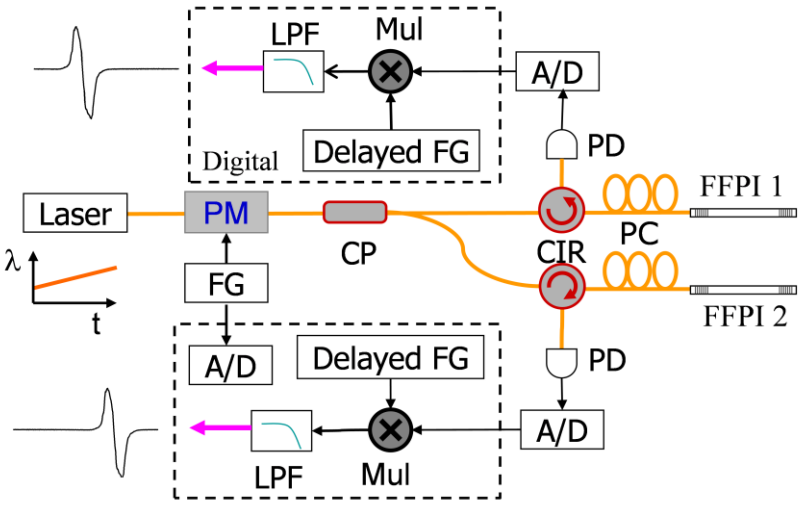

Fig. 4-7 Configuration of sensor. CP, coupler; PM, phase modulator; CIR, circulator; PD, photo diode; FG, function generator; PC, polarization controller; A/D, analog to digital convertor; Mul, multiplier; LPF, low pass filter.

The schematic configuration of the proposed sensor is shown in Fig. 4-7. It consists of a pair of identical FFPIs; one is for the sensing of strain, and the other is strain-free working as a reference and a temperature sensor for temperature compensation. This scheme is critical for quasi-static strain sensing to distinguish the resonance shift by strain from that by environmental temperature variation. Each FFPI, fabricated by Fujikura Ltd., is formed by writing two identical FBGs 20-cm distant in a single mode fiber (SMF). The parameters of the FBGs are: nominal center wavelength 1549.85 ± 0.04 nm, bandwidth 0.25 nm, and peak reflectivity 99.5%. Considering the free spectrum range (FSR) of about 4 pm, each FFPI has potential to resonate at tens of frequencies within the overlapped high reflection region of its two FBGs.

A narrow linewidth tunable fiber laser is used to interrogate the FFPIs with the FM interrogation technique. The lightwave from the laser source is phase-modulated with a phase modulator (PM) driven by a sinusoidal function generator (FG), and thus two

sidebands are generated besides the carrier. When these light-waves are reflected by an FFPI, an intensity modulation appears in the reflected light. By demodulation of this intensity modulation with a multiplier (Mul) and a low pass filter (LPF), an output signal is obtained, which is a function of the frequency deviation between the laser and the resonance of FFPI.

4.3.2 Digital demodulation configuration

The demodulation process is realized in digital domain. Both the modulation signal for PM and the reflected light power detected by photo diodes are sampled using a high speed analog to digital convertor (A/D). The demodulation is achieved using a PXIe system, with a high speed DAQ (NI, 5761R). The sampling frequency of DAQ is 250 MHz. A field-programmable gate array (FPGA) module (NI, 7965R) is used to assistant the data processing.

The data processing in the FPGA is shown in Fig. 4-8. The 5761R has 4 channels. Two channels are connected with the reflected powers from the two FFPI sensors. The reference is connected with the third channel, and is shared as the reference for both FFPIs. Then the data is processed in the FPGA module.

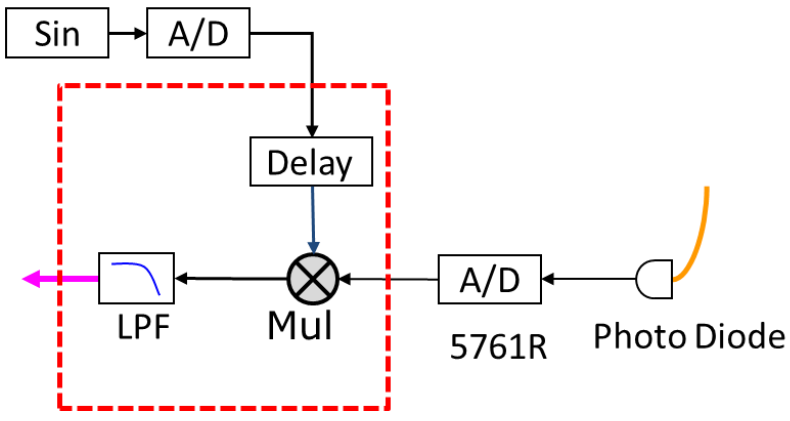

Fig. 4-8 Schematic of digitized demodulation. Mul, multiplier; LPF, low pass filter

The sampling frequency for the 5761R (A/D conventor) is 250 MHz, while the FPGA works at top-level clock of 40 MHz. A target-scope FIFO (First in first out) structure is used to transform the data between multi-clock domains, as shown in Fig. 4-9. The FPGA works continuously without stop to process the data, while 5761R will wait after each continuous sampling of about 64 us, to avoid data overflow in the FIFO. The full speed sampling of 5761R is critical for the high bandwidth of the system.

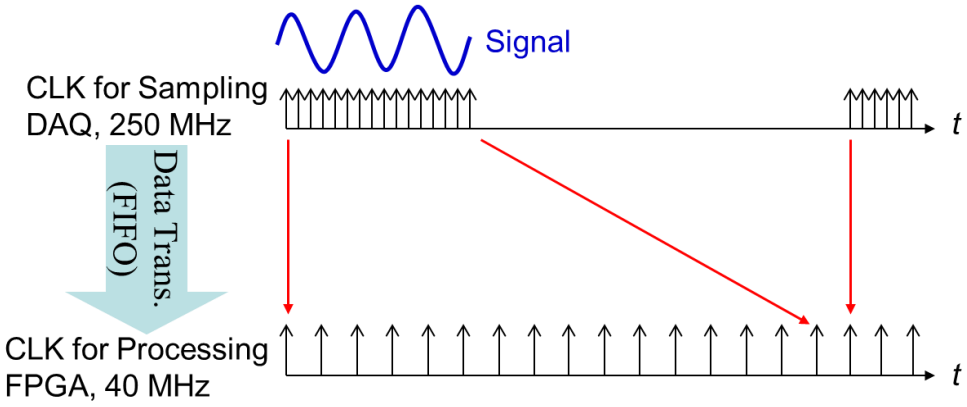

Fig. 4-9 FIFO for transmission data between multiplex clock domains.

In the digitalized realization of the demodulation, two problems have to be considered. One is that the phase of reference signal for multiplier mush be adjustable. This problem is solved by an adjustable time delay for the reference signal. The last 125 data of reference is stored in a data array structure. Then one of the delayed references multiplies with the reflected power from FFPI. The size of the array to store reference determines the range of phase adjustable range, and the sampling speed of 5761R determines the phase adjustable resolution. The other problem is to remove the offset of the reference. In the program the reference subtracts its average to eliminate the offset of the sampled reference signal.

Compared with analog circuits, the digital processing has smaller low frequency noise, finer control of the phase match for the demodulation, and flexible design of the low pass filter.

4.3.3 Experimental results

The laser wavelength sweeps within the overlapped high reflection region of the FFPIs. The tunable range is 5 pm, larger than the FSR to necessarily reveal at least one complete resonance peak for both FFPIs. A group of typical demodulated signals during one wavelength sweep are shown in Fig. 4-10. It is noticed that there are two groups of resonances for each FFPI due to the existence of two polarization modes in the SMF based FFPIs. In experiments, one group of resonance mode is suppressed (shown as the circled small peaks in Fig. 4-10) by using a polarization controller (PC), and the residual signal is digitally removed before the cross-correlation. This problem can be completely solved if polarization maintaining fiber (PMF) based FFPIs are used.

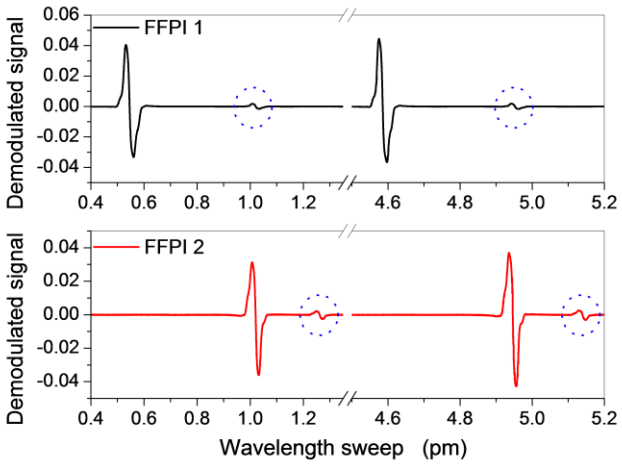

Fig. 4-10 Measured output signals from the FFPIs. The dual resonance peaks are due to the existence of two polarization-modes in the FFPI, where the circled small ones are the polarization modes suppressed by PC

In experiments, both FFPIs are strain-free packaged to ascertain the performance of the sensing system. A fiber laser (NKT, E15, linewidth 1 kHz) with integrated piezo tuner is used to interrogate the two FFPIs simultaneously via 3-dB coupler. The driver (PI, E-625) of piezo is controlled by computer directly. The laser sweeping speed is 0.3 pm/s (scanning time 17 s for 5-pm wavelength range). A function generator (Agilent,

33250A) is used to drive the PM with 2-MHz sinusoidal waveform. The lightwaves reflected by FFPIs are detected by high-speed photo diodes (New Focus, 1181) via circulators. The driving signal for PM and the outputs of photo diodes are sampled by a high speed A/D convertor (NI, 5761R). The FPGA module (NI, 7965R) is employed to assist data processing for enhancing the speed.

The evolution of the resonance difference between the two FFPIs against time is monitored and logged 2 times per minute. The program is designed to automatically select the first complete resonance peak from the demodulated signals for each FFPI, and then calculate the resonance difference using the cross-correlation algorithm. Fig. 4-11(a) plots the detected resonance wavelengths of both FFPIs, respectively. Fig. 4-11(b) shows the extracted resonance difference between the two FFPIs. The jump in the figures indicates the resonance mode switch due to the resonance frequencies slipping caused by environmental temperature change as the FFPI has similar thermal-wavelength response as FBG. The amplitude of the jump exactly equals to the FSR of FFPIs. Because the FSR can be precisely measured, and the direction of the resonances' slip can be logged, the jump can be removed in data processing. As a result, this sensing system has large dynamic range of hundreds of με, as long as the high reflection regions of all the FBGs remain overlapped under applied strain. Irrespective of the resonance mode switch, the standard deviation of the measured resonance difference between the two FFPIs is only 5.4 fm after temperature compensation as shown in Fig. 4-12. The FFPI's strain sensitivity is measured to be 0.93 ± 0.02 pm/με, so a corresponding strain resolution of 5.8 nε is achievable with the system, if the sensor head is designed properly.

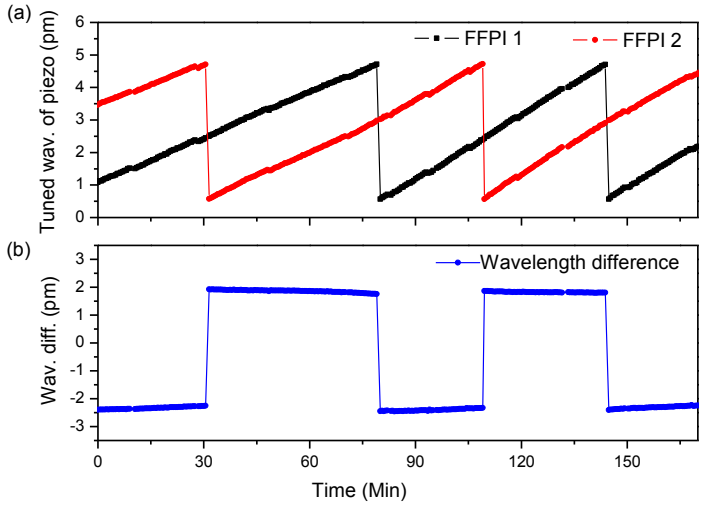

Fig. 4-11 Experimental results. (a) Detected resonance wavelengths of two FFPIs, respectively; (b) the resonance difference extracted by cross-correlation

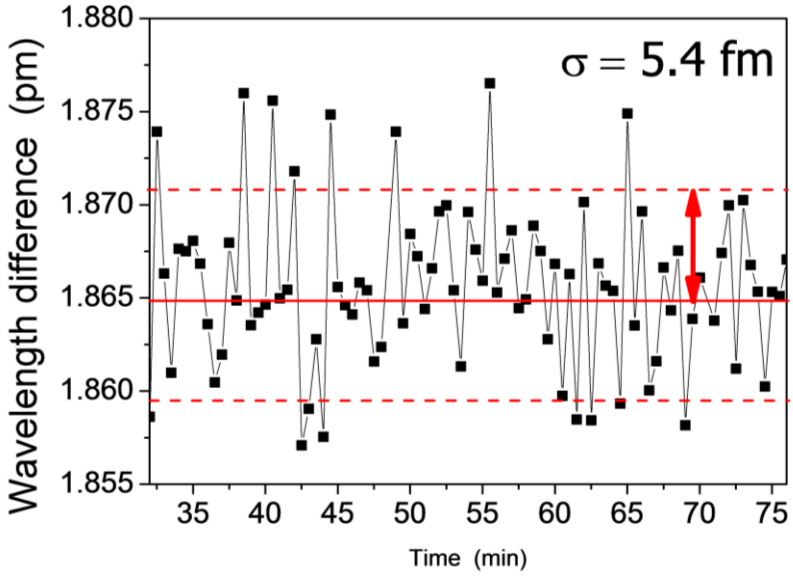

Fig. 4-12 Part of the extracted resonance difference (from Fig. 4-11(b)). The standard deviation for all measured data after temperature compensation is 5.4 fm.

4.3.4 Discussion

The realization of the nano-order static strain resolution is a combination of good wavelength accuracy of the fiber laser tuned by piezo, and the FM demodulation technique which is immune to the residual reflection from fiber components. The

cross-correlation algorithm is then used to draw the potential of the high resolution. Unlike the FBG sensors based with tunable lasers, the laser wavelength repeatability during sweeping is less significant in the proposed sensor system. Instead, the resolution is mainly limited by the nonlinearity of the voltage-wavelength response during the wavelength sweep, as the resonances of the two FFPIs are usually separated in practice. Therefore, even finer resolution is achievable with longer FFPIs. Longer FFPI has smaller FSR and requires smaller tuning range of the laser; thus, better sweeping linearity is expectable even with lower cost lasers.

4.4 Conclusion

In this chapter, the development of an ultra high resolution and large dynamic range static strain sensor using a pair of FFPIs is reported. The laser scans the FFPI sensor heads and the reflected optical signals are demodulated with a frequency modulation (FM) technique. A cross-correlation algorithm is employed to calculate the wavelength difference between the two sensor heads. Ultra-high static strain resolution down to 5.8 nε was demonstrated, and the dynamic range can be extended to hundreds of με. Together with the short sensing time down to tens of seconds, this research reveals the potential of optical fiber sensors in geophysical applications.

Chapter 5.
FFPI sensors with sideband interrogation technique

In this chapter, we developed a novel sideband interrogation technology to measure the resonance frequency difference between a pair of FFPIs. A special sideband is generated to interrogate the sensing FFPI, while the carrier interrogates the reference FFPI simultaneously. With this technique, extreme high static strain resolution of 0.3 nε is achieved. Using a special designed RF modulator, real-time strain sensing is achieved with strain resolution down to 0.05 nε. The principle of the sideband interrogation, the design of modulator, and the experimental results are discussed in detail in the following sections.

5.1 Sideband interrogation technology

5.1.1 Motivation of the research

As we pointed in the chapter 1, the static strain sensor is to measure the arbitrary (usually slowly varying) signals in a given period of time. It is easily be influenced by environment noise, and thus an extra reference is necessary. An identical sensor head but free of strain is an ideal candidate, because it can not only compensate the wavelength drift of the laser, but also the thermal drift of the sensor head itself. In the previous research, the laser sweeps to scan the resonance of the FFPIs, covering the spectra of both sensor heads. The resolution of sensor suffers from the nonlinearity of the laser during sweeping. So we wonder whether we could interrogate the two FFPIs

simultaneously instead of laser wavelength sweep. With this idea a sideband interrogation technology is invented.

5.1.2 Review of FM technology

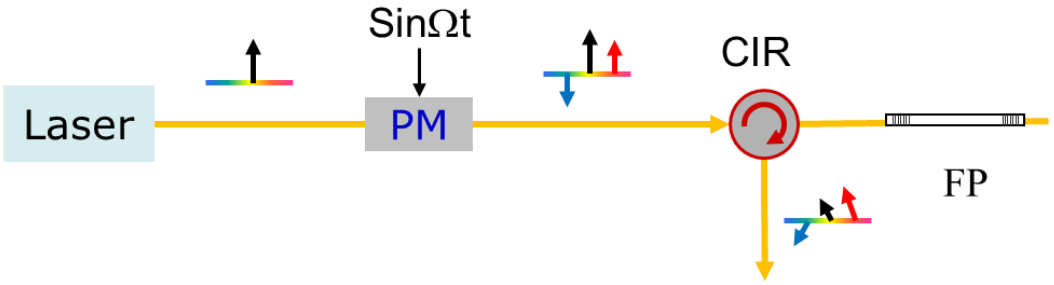

Fig. 5-1 Schematic of modulation configuration in FM technology

Let's review the principle of the FM technology for the interrogation of FFPIs in chapter 4. As shown in Fig. 5-1, a laser beam has an electric field given by $E_0 e^{i\omega t}$ is modulated by a phase modulator (PM) driven by a sine signal. After the beam passes through the PM, it electric field is

$$e^{i\omega t+\beta\sin\Omega_M t} \approx e^{i\omega t}\left(1+\frac{\beta}{2}e^{i\Omega_M t}-\frac{\beta}{2}e^{-i\Omega_M t}\right). \tag{5.1}$$

There are three different beams: a carrier with radian frequency ω, and two sidebands with frequencies (ω±Ω), respectively. Here Ω is the radian frequency of phase modulation, and β is known as the modulation depth.

All above beams impinge the FFPI and are reflected. Since the reflection of FFPI is a function of frequency, those beams experience different amplitude reflection and additional phase change. The sum of reflected beams exhibits an intensity modulation, which is demodulated to get the resonance information.

5.1.3 Sideband generation

Now we consider that a laser beam with electric field $E_0 e^{i\omega t}$ is modulated by an intensity modulator (IM) driven by a radio frequency signal. After the beam has passed through the IM, it electric field is

$$\left(1+k\cos\Omega t\right)e^{i\omega t} = e^{i\omega t} + \frac{k}{2}e^{i(\omega+\Omega)t} + \frac{k}{2}e^{i(\omega-\Omega)t}, \tag{5.2}$$

here k is the intensity modulation depth, $k \leq 1$. The modulation generates two sidebands, and eithor sideband is shifted from the carrier by the modulation signal.

If we modulate the IM using a signal as

$$F(t) = \cos\left(\Omega_S t\right) + \cos\left(\Omega_S t + \Omega_M t\right) - \cos\left(\Omega_S t - \Omega_M t\right), \tag{5.3}$$

here Ω_S and Ω_M are different radio frequencies. The electric field of modulated beam is

$$\left[1+kF(t)\right]e^{i\omega t} = e^{i\omega t} + \frac{k}{2}e^{i(\omega+\Omega_S)t}\left(1+e^{i\Omega_M t}-e^{-i\Omega_M t}\right) + \frac{k}{2}e^{i(\omega-\Omega_S)t}\left(1-e^{i\Omega_M t}+e^{-i\Omega_M t}\right). \tag{5.4}$$

Besides of the carrier, two groups of sideband appear in Eq. (5.4). Each group of sideband in Eq. (5.4) has similar form as Eq. (5.1) with the same modulation frequency of Ω_M, but their center frequencies are shifted from the carrier by Ω_S. As shown in Fig. 5-2, this characteristic enables us to utilize the sideband to interrogate the sensing FFPI, which has a resonance frequency different from the carrier frequency with the same demodulation method. According to analysis in chapter 4, the extracted signal of FM technique vanishes zero when the laser frequency goes far away from the resonance. As long as the other sidebands frequency is far from the resonance frequencies of the FFPI, it has no contribution to the extracted signal.

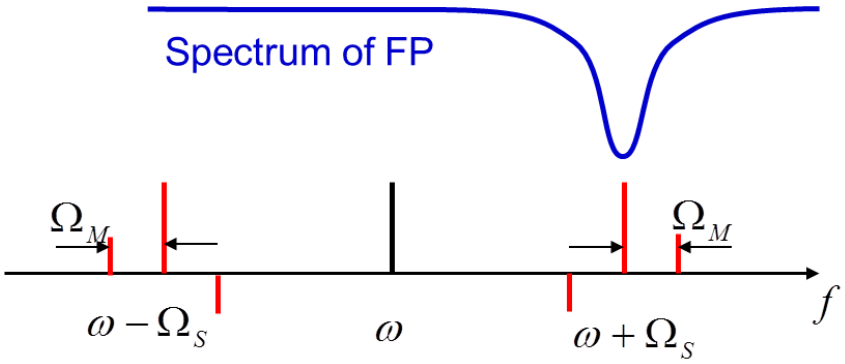

Fig. 5-2 Sideband for interrogation of FP.

It should be notice that the above method is not the only way to generate sidebands that has form as Eq. (5.1). For example, if a PM is driven by signal of Eq. (5.3) instead of the IM, the PM will produce a series of sidebands, with the sidebands intensity satisfying the Bessel function, as shown in Fig. 5-3. The first order sidebands will also have the same form as Eq. (5.1), with intensity of $J_1(\beta)$. When the modulation depth β is small ($\beta \ll 2$), $J_1(\beta) \approx \beta/2$, and the higher sidebands is negligible. However, the intensity of first order sideband is also very small, resulting in small signal-to-noise ratio of the demodulation signal. $J_1(\beta)$ becomes larger when β increases, and reachs maximum at β=1.84 , but the higher sidebands becomes stronger at meantime. Since the FFPI has many resonance frequencies with interval of FSR, when the first order sideband lies at resonance, the other sidebands likely cause interference with different resonance frequencies.

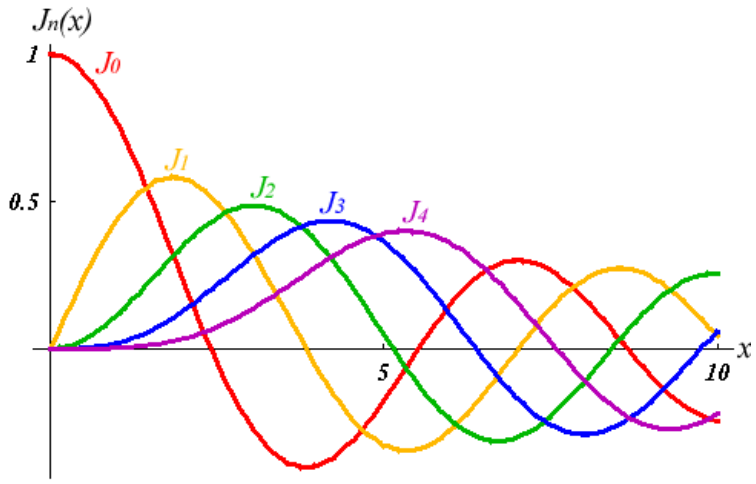

Fig. 5-3 Bessel function (the first kind)

When the light beam with form of Eq. (5.1) passes through an IM driven by frequency of Ω_S, the output light beam will be

$$\begin{aligned} e^{i\omega t}\left(1+\frac{\beta}{2}e^{i\Omega_M t}-\frac{\beta}{2}e^{-i\Omega_M t}\right).\left[1+k\cos\Omega_S t\right] &= \left(1+\frac{\beta}{2}e^{i\Omega_M t}-\frac{\beta}{2}e^{-i\Omega_M t}\right)e^{i\omega t} \\ &+\frac{k}{2}e^{i(\omega+\Omega_S)t}\left(1+\frac{\beta}{2}e^{i\Omega_M t}-\frac{\beta}{2}e^{-i\Omega_M t}\right) \\ &+\frac{k}{2}e^{i(\omega-\Omega_S)t}\left(1+\frac{\beta}{2}e^{i\Omega_M t}-\frac{\beta}{2}e^{-i\Omega_M t}\right). \end{aligned} \tag{5.5}$$

Now the sideband also has the same form as Eq. (5.1), and the high-order sidebands are avoided. The main drawback is that the carrier is also has same frequency components as the sidebands, and might cause interference when it is close to the resonance of the FFPI. Another drawback is that the intensity of each beam in the sidebands is fixed as the typical FM techniology, and thus limits the SNR of extracted signal.

5.1.4 Simultaneously interrogation with sideband and carrier

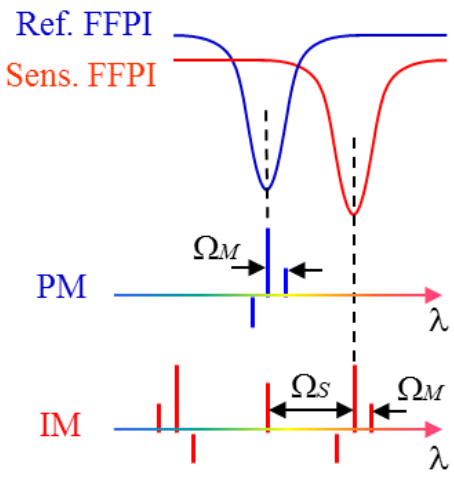

Fig. 5-4 simultaneously interrogation of FFPIs with sideband and carrier respectively.

For the static strain sensors using Fabry-Perot interferometers as sensor heads, the resonance frequencies of the Fabry-Perot interferometers are usually different in practice. The different resonance can be simultaneously interrogated, as shown in Fig. 5-4. A typical FM technique with a PM is used to interrogate the reference FFPI. At the same time, the sidebands are generated with an IM for the interrogation of the sensing FFPI. The reflected beams from both FFPIs are demodulated respectively. Because both the PM and the IM paths of light have the same modulation frequency of Ω_M, they can use the same demodulation schemes as that for the typical of FM technologies.

5.2 Static strain sensing with sideband interrogation technology

Simultaneous interrogation of two FFPIs is important for the static strain sensing, which requires the measurement of the resonance frequency difference between the sensing and reference FFPIs. A schematic configuration shown in Fig. 5-5 is used for the static sensing. The system consists of a pair of FFPIs, one for strain sensing and the other for reference. A narrow linewidth tunable laser is used as the light source. The

light is split into two paths. One path of light is modulated by a PM driven by RF1 to interrogate the reference FFPI. The other path is modulated by an IM driven by RF2 to generate sidebands for the interrogation of sensing FFPI. The laser frequency sweeps over the resonance of the reference FFPI. The RF2 is chosen to ensure that one group of sidebands sweeps over the resonance of the sensing FFPI at the same time.

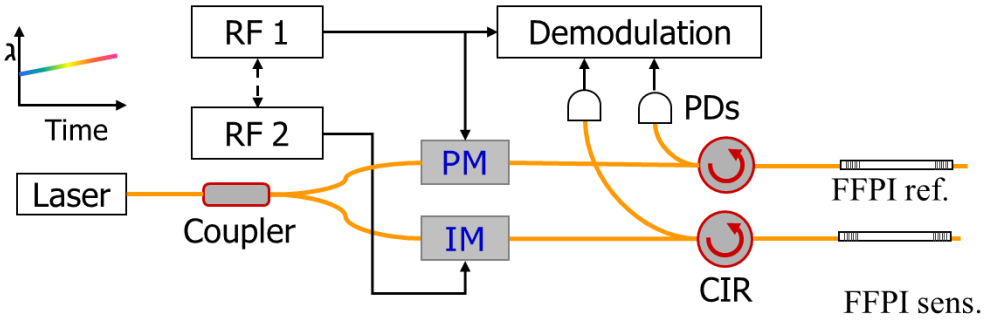

Fig. 5-5 Schematic of static strain sensing with sideband interrogation technology.

5.2.1 System configuration

The schematic setup of the sensor is shown in Fig. 5-6. It consists of a pair of identical FFPIs (fabricated by Fujikura Ltd.), the same FFPIs as used in chapter 4. The parameters of the FBGs are: nominal center wavelength 1549.85 ± 0.04 nm, bandwidth 0.25 nm, and peak reflectivity 99.5%. The free spectral range (FSR) and the bandwidth of the FFPIs are 4.1 pm and 0.9 MHz, respectively.

The frequency of the narrow linewidth laser source is tuned to sweep around the resonance of the reference FFPI, as the PM light shown in Fig. 5-4. Then the Ω_S is adjusted to approximate the resonance frequency difference between the two FFPIs. As a result, one group of sideband is shifted to sweep around the sensing FFPI simultaneously, as the IM light shown in Fig. 5-4. The other group of sideband has no contribution to the demodulated signal as long as they are far away from any resonance frequency of the sensing FFPI. This problem can be completely eliminated by replacing

the sensing FFPI with a polarization-maintaining fiber (PMF) based π-phase-shifted FBG as the sensor head, because only one resonance frequency exists in this case.

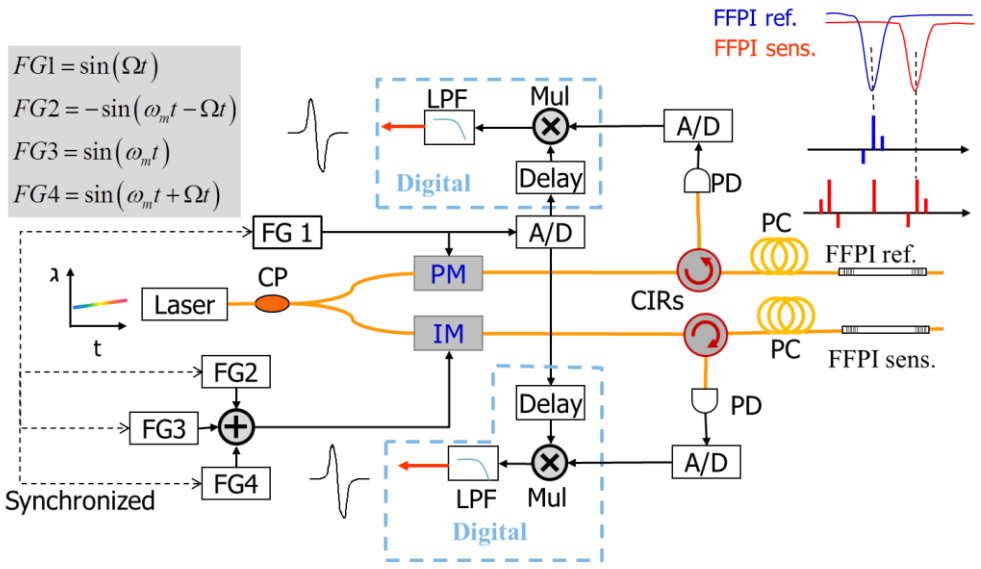

Fig. 5-6 Experimental setup. CP: coupler; PM: phase modulator; IM: intensity modulator; CIR: circulator; PD: photo-detector; FG: function generator; Mul: multiplier; LPF: low pass filter.

During one wavelength sweep of the laser, the demodulated signals from the two FFPIs are similar in shape but staggered in horizontal position, as shown in Fig. 5-7. A cross-correlation algorithm is employed to calculate the frequency difference of the demodulated signals with high resolution, which has good capability of suppressing random errors. The extracted frequency difference plus Ω_S is the actual resonance difference between the two FFPIs.

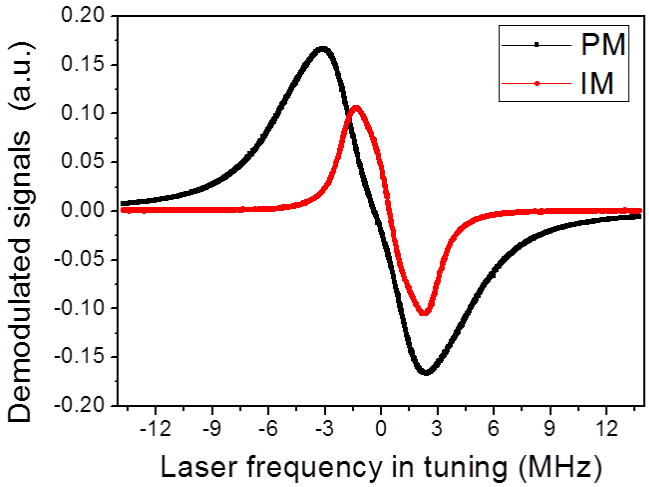

Fig. 5-7 Demodulated signals from the two FFPIs when the laser frequency is swept around the resonance of the FFPIs

In experiments, both FFPIs are placed under strain-free condition to ascertain the performance of the sensor system. A fiber laser (NKT, E15, linewidth 1 kHz) with integrated piezo tuner is used as the light source. The frequency of the laser is finely tuned via a piezo-driver (PI, E-625) directly controlled by a computer. The laser frequency sweeping speed is 37 MHz/s and the sweeping range is 46 MHz. The PM is driven by a 2-MHz RF signal from FG1 (NI, PXI-5421). In this experiment Ω_S was set to 67 MHz, and the IM is driven by the sum of three RF signals with frequencies of 65 MHz, 67 MHz and 69 MHz from FG2 to FG4 (NI, PXI-5422), respectively. All the 4 FGs are synchronized to maintain the frequency and phase relationship of the RF signals. Since two groups of resonance modes exist for each FFPI due to polarization modes in the SMF, a polarization controller (PC) is used to suppress the unwanted group of resonance modes. The light-waves reflected by FFPIs are detected by high speed photo-detectors (New Focus, 2503) via circulators. The outputs of photo-detectors together with the driving signal for PM are sampled by a high speed analog to digital convertor (NI, 5761R) and then processed in digital domain, as the demodulation method in chapter 4.

5.2.2 Experimental results

The extracted frequency difference from the demodulated signals over 2 hours is shown in Fig. 5-8. The fluctuation range (standard deviation) is 94 kHz, which also determines the frequency resolution of the sensor system because the inaccuracy in the measurement of Ω_S is negligible. The strain sensitivity of the FFPIs is tested to be 116 MHz/με; thus, a corresponding strain resolution of 0.8 nε is achievable with the sensor system, if the sensor head is designed properly.

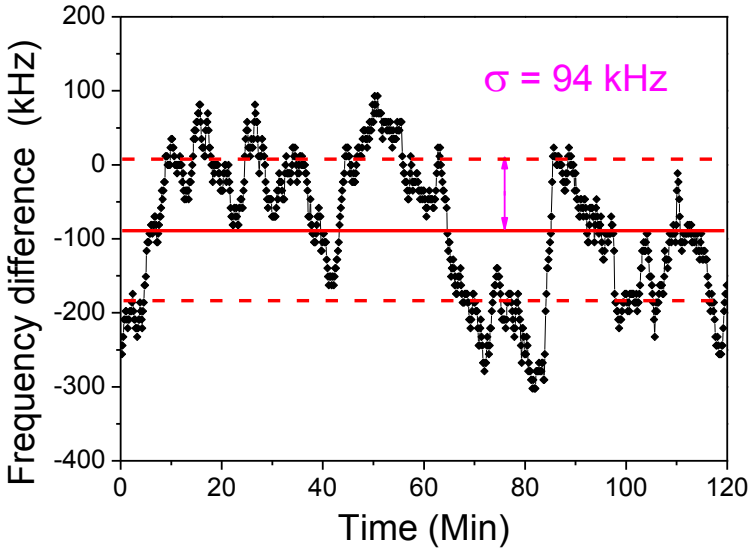

Fig. 5-8 Extracted frequency difference between demodulated signals

5.3 Improved static strain sensor with feedback control

For the practical strain sensor, the sensors experience thermal fluctuation and strain change, which result in the resonance frequencies of the FFPIs changing accordingly. The strain sensor should be able to follow the resonances change. For this reason feedback control loops are added to the sensor configuration.

5.3.1 System configuration

The system configuration is shown in Fig. 5-9. Compared with the sensor shown in Fig. 5-6, both the laser sweeping range and the wavelength shift of sideband Ω_S are automatically adjusted by feedback loops.

The first feedback loop is the laser sweeping range. As shown in Fig. 5-9, the laser from source is spilt into two paths, and one path interrogates the reference FFPI with typical FM technology. The extracted signal from this path after a complete laser wavelength sweeping is shown as the black curve in Fig. 5-10. From the demodulated curve, the resonance of the reference FFPI is determined, which is used for the center of wavelength tunable range for next wavelength sweep. This configuration ensures that the laser covers the resonance of the reference FFPI, and sweeping range could as small as possible. A small sweeping range is critical to reduce the sensing period, and more important, the strain resolution could be improved because higher wavelength linearity is much easier to realize, because the laser has better wavelength linearity in a smaller sweeping range.

It should be pointed out that, due to the limited bandwidth of FBGs of the FFPI, the finesse of the FFPI varies with different incident laser wavelength. As a result, the shape of extracted signal froml FM interrogation technology also varies. The shape difference between Fig. 5-7 and Fig. 5-10 is caused by the different finesse of the FFPI with corresponding interrogation wavelength.

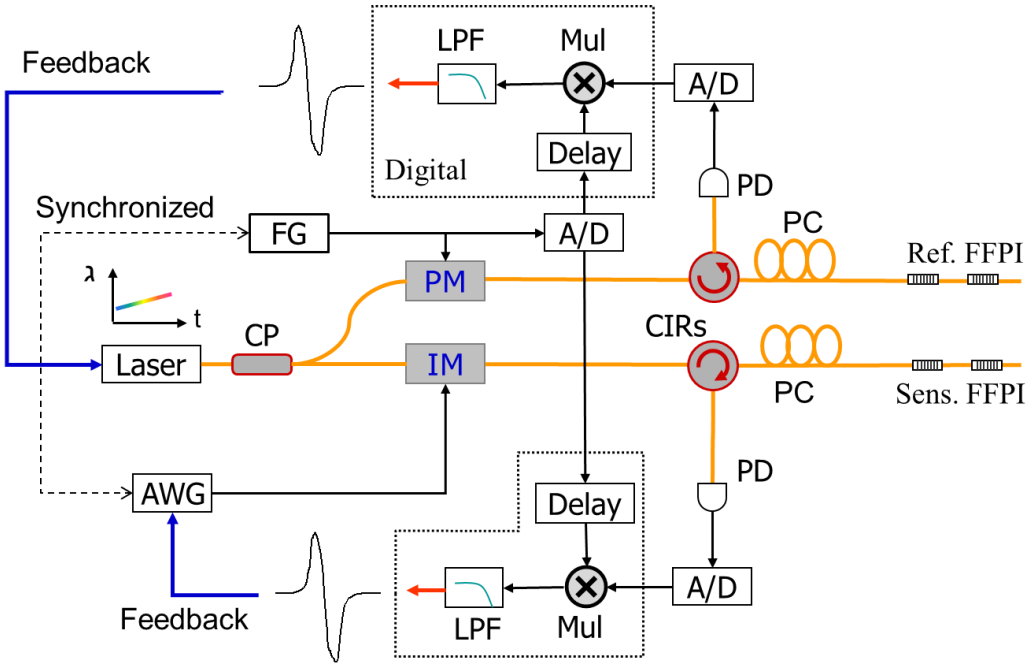

Fig. 5-9 System configuration. CP: coupler; PM: phase modulator; IM: intensity modulator; CIR: circulator; PC: polarization controller; PD: photo-detector; FG: function generator; AWG: arbitrary waveform generator; Mul: multiplier; LPF: low pass filter

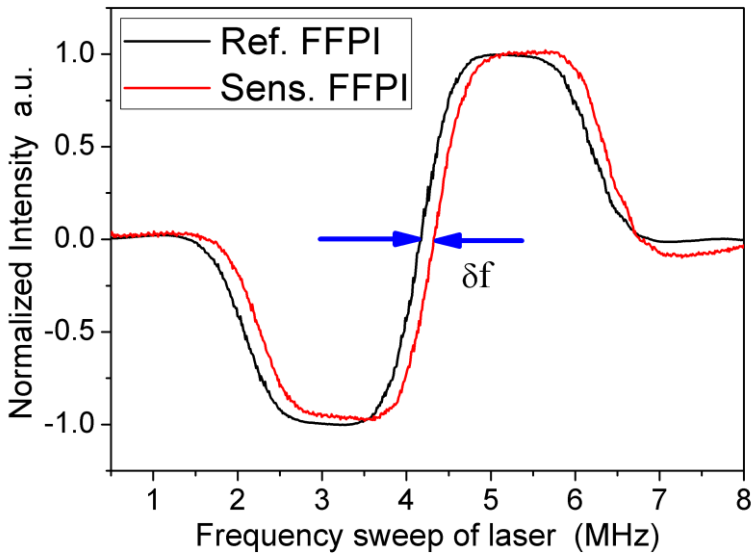

Fig. 5-10 Demodulated signals (δf is enlarged for visibility)

The other feedback loop is for the adjustment of the sideband center wavelength. The signal to drive the IM should have the form as Eq. (5.3), which is the sum of three cosine RF functions. In configuration of Fig. 5-6, three synchronized function generators (FGs) are used to generate this signal. The change of Ω_S involves the adjusting of the three FGs simultaneously. In the improved configuration, an arbitrary waveform generator (AWG) is used to generation the signal of Eq. (5.3). The adoption of AWG simplifies the system configuration. The extracted signal of the sidebands is shown as the red curve in Fig. 5-10. After each sweep, a cross-correlation algorithm is employed to calculate the stagger δf between the two extracted curves, and then adjust Ω_S to eliminate the δf in the next sweep. So Ω_S can follow the resonance difference change between the FFPIs..

5.3.2 Experimental results

In the experiment, both of the FFPIs are free of strain. The measurement of resonance difference was repeated for tens of times. Fig. 5-11 shows the resonance difference δf between the extracted signals. Fig. 5-12 is the variation of measured resonance difference between the two FFPIs, which is the sum of Ω_S and the accordingly extracted δf. During the experiment, the measured resonance difference varies with a standard deviation of 29 kHz. This value includes not only the noise level of the measuring system, but also the actual wavelength difference fluctuation due to minor environmental disturbance. As δf during the measurements fluctuates with a standard deviation of 16 kHz, and Ω_S is measured with precision better than 1 kHz, this system has resonance better than 29 kHz in the measurement of resonance frequency difference between interferometers. Considering the strain sensitivity of 116 MHz/με for the FFPIs, a corresponding strain resolution of 0.3 nε is achievable when those FFPIs are used for static strain sensing with proper sensor head design.

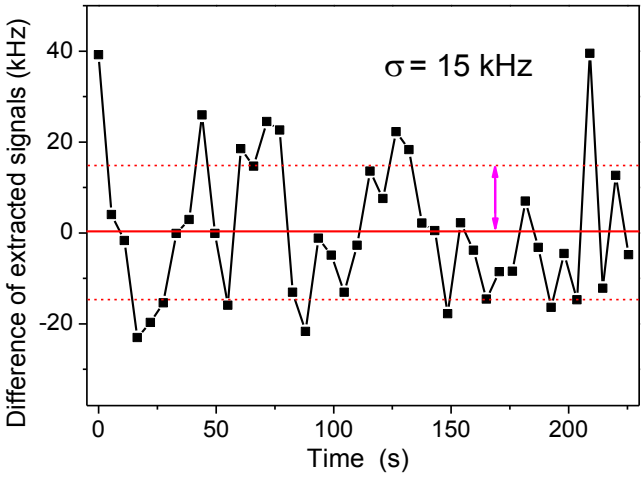

Fig. 5-11 Difference of extracted signals (δf)

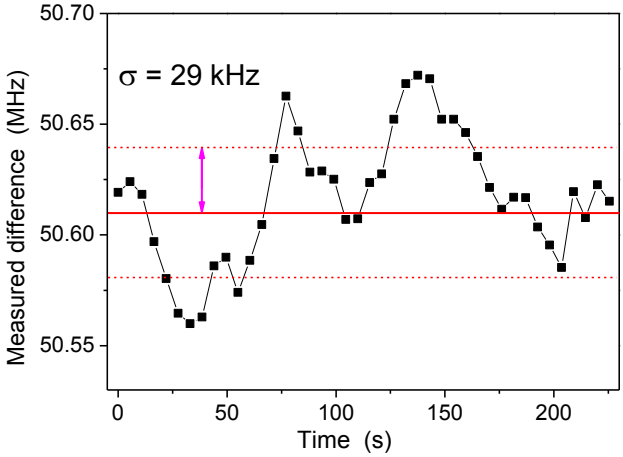

Fig. 5-12 Measured resonance frequency difference between FFPIs

5.3.3 Discussion

The realization of the sub-nε static strain resolution is based on the precise measurement of the resonance frequency difference between the two FFPIs. First, the resonance difference is approximately compensated by the frequency of accurately generated sideband. Then, the residual difference between the resonance frequencies is precisely measured with the RF demodulation technique and the cross-correlation algorithm. Currently the measurement range of the sensor is half of the FSR of the sensing FFPI. By replacing the FFPIs with π-phase-shifted FBGs, and adjusting the Ω_S

to track the variation in resonance frequency difference, much larger dynamic range is expectable without resolution degradation.

5.4 Realtime strain sensor with sideband interrogation technology

5.4.1 Real-time strain sensing

It has been a common way to catalog strain sensors into dynamic sensors (for signals above 10 Hz) for detecting rapid changes, and quasi-static sensors (for signals below 10 Hz) to measure the slowly varying signals such as temperature and seismic motion [38]. Here we'd like to look into the nature of dynamic and quasi-static strain signals.

As indicted by the name, the dynamic strain signal varies quickly, repeating itself with frequency larger than 10 Hz. The signal is self-referenced, because the complete shape of strain signal can be obtained within a short measuring time. The strain signal is evaluated by the spectrum analysis, and the Fourier transform of the measured data is enough to evalute the strain signal. The strain resolution is also described with unit of $\varepsilon/\sqrt{\text{Hz}}$, limited by the noise level of the sensing system.

On the other hand, the quasi-static strain signal varies slowly, either repeating itself with long period larger than 0.1 s, or being total arbitrary (corresponding to infinite long period). If the quasi-static strain signal is also evaluated in frequency domain, the measurement should last for infinite long time to achieve the spectrum of the signal, which is inconvenient or impossible in some applications. Instead, the quasi-static strain sensing should be evaluated in time domain, drawing the temporal profile of the strain. Since the strain does not repeat itself, an extra-standard is required to measure the strain. In the sensors that we have developed, the extra-standard is an identical sensor head free of strain. The sensing system detects the strain by measurement of the wavelength difference between the sensing sensor head and the reference sensor.

We find that, the sensor with extra-reference can also be used for measuring quick varying signals just as used for the quasi-static strain sensing. The measured data from the sensing sensor head is compared with the reference to obtain the strain signal, and then display the strain in temporal domain. Any change of strain will be reflected by the measured data, capable of both slowly and quick varying signals. This type of sensors is called real-time strain sensor. For the geophysical sensors, the interested strain signal extends from dc to about 100 Hz. It is a good example of the real-time strain sensor.

5.4.2 Sensor configuration for real-time sensing

For the geophysical research, attention is focused on the deformation information in the frequency region from dc to about 100 Hz, corresponding to the real-time strain sensor. In the previous work, we have solved the ultra-high resolution static strain sensing, and now it is time to achieve the ultra-high resolution in the real-time domain.

As the analysis in the above section, a real-time sensor requires a strain-free reference sensor head, and it is capability of quick strain varying. The sideband interrogation technology is an ideal method for the real-time sensing because of its two characteristics.

First, the capability of simultaneous interrogation of the two sensor heads. In the case that the two sensors heads are interrogated sequentially, the laser sweeping range has to cover the spectra of both sensor heads, while their resonance difference is not constant but varying as the applied strain. To follow the quick varying strain signal, the laser has to repeat the wavelength sweeping at high frequency, which is very difficult with a large sweeping range. But in the sideband interrogation technique, the two sensors heads are interrogated simultaneously with carrier and sideband, respectively. The resonance frequency difference induced by strain is compensated by the frequency shift between the carrier and sideband. When the laser works in sweeping mode sweeping over the resonances of sensor heads, the sweeping range is not influence by

the applied strain and remains small (fixed at several times of the bandwidth of FFPIs). And, the laser can also working in locked-in mode as to be introduced in the following paragraph.

The second characteristic is the ability of lock loop via feedback control. In either the typical FM or the new sideband interrogation technologies, the extracted signal crosses zero when the center wavelength lies at the resonance of the FFPI, as shown in Fig. 5-13. This characteristic is critical for the real-time feedback control to lock the carrier or sideband to the resonance frequency.

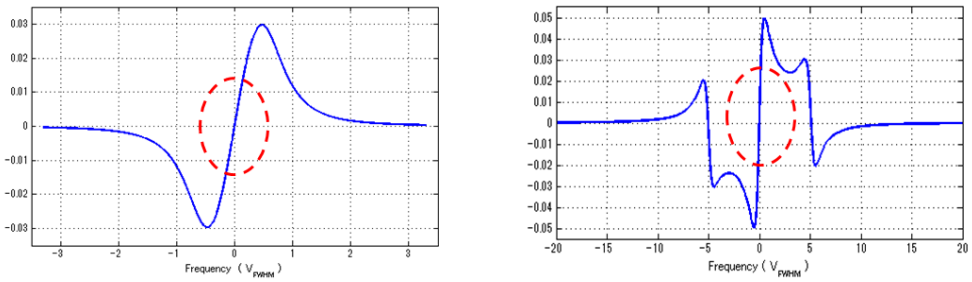

(a) (b)

Fig. 5-13 Demodulated signals of FM interrogation technology. (a) Low modulation frequency; (b) High modulation frequency

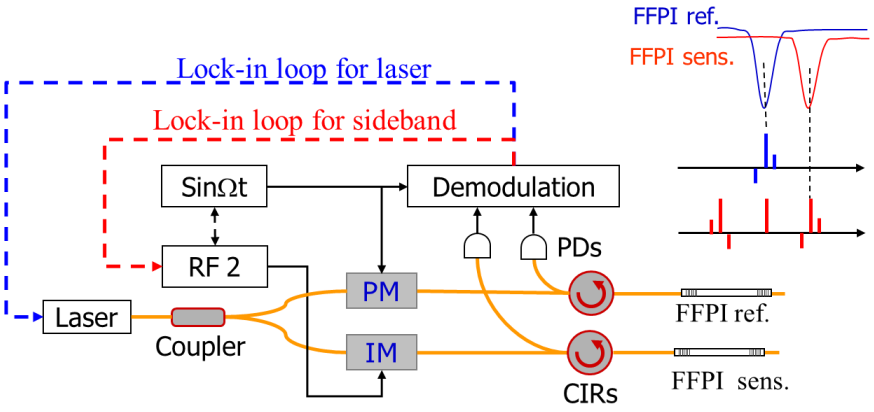

Fig. 5-14 Schematic for real-time sensor with lock loop control

5.4.3 Lock loops with PID controller

The feedback control woks in the following way (using the carrier for example): First, the laser wavelength is set to a certain value around the resonance of the reference FFPI; then the demodulated signal is obtained and its sign is used to determine the deviation of laser from the resonance of FFPI. As shown in Fig. 5-13, positive demodulated signal indicts that the laser frequency is larger than the resonance. If the demodulated signal is negative, the laser wavelength is smaller than the resonance. Then a feedback is sent to the laser to adjust the laser wavelength for compensation. The above comparison - adjusting repeats, and finally the laser frequency is corrected to exactly the resonance of the reference FFPI. The sideband is corrected to the resonance of the sensing FFPI with a similar way, as shown in Fig. 5-14.

The feedback is obtained by using PID (proportional-integral-derivative) controller. The block diagram is shown in Fig. 5-15. According to analysis in the above section, the output of demodulation is a function of the laser carrier frequency, and also used to adjust carrier frequency. It is the process varies (*PV*) of this system. The target of the controlling loop is to set the output of demodulation to zero and to maintain this status. Thus zero is the setpoint (*SP*) in this controlling loop. The difference between the *PV* and *SP* is the error signal (*e*). The current carrier frequency is the output of controller loop and is the input for the sensing system. It is called moving varies (*MV*).

The block diagram of PID controller is shown in Fig. 5-15. The output is given by

$$u(t) = K_p e(t) + K_i \int_0^t e(\tau) d\tau + K_d \frac{d}{dt} e(t) \tag{5.6}$$

where K_p is the proportional gain, K_i is the integral gain, K_d is the derivative gain, and e is the error, $e = SP - PV$. The output is the sum of three parts: the proportional term, the integral term, and the derivative term.

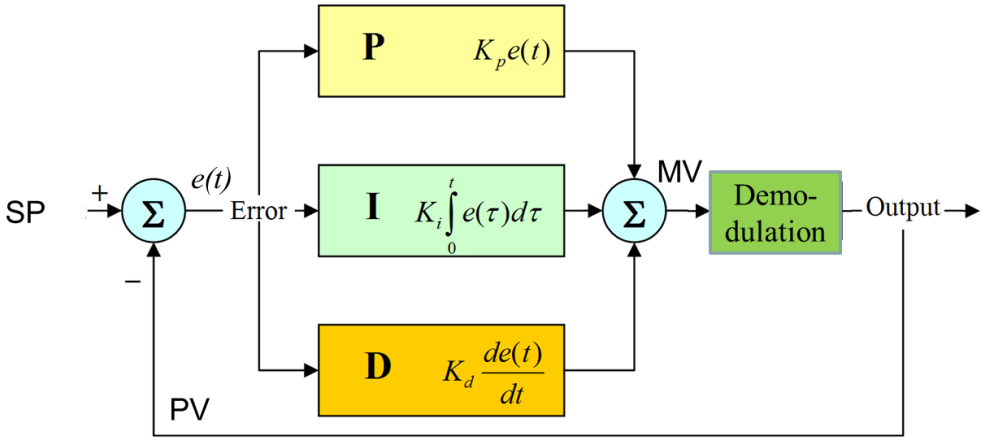

Fig. 5-15 Block diagram of PI controller. SP, setpoint; PV, process variable; MV, manipulated variable, e, error signal [39].

The proportional term usually plays the dominant role. The $K_p e(t)$ term makes a change to the output that is proportional to the current error value. The proportional response can be adjusted by multiplying the error by a constant K_p, called the proportional gain. The optimized proportional gain is the slope of the response of the demodulation signal.

The contribution from the integral term $K_i \int_0^t e(\tau)d\tau$ is proportional to both the magnitude of the error and the duration of the error. The integral in a PID controller is the sum of the instantaneous error over time and gives the accumulated offset that should have been corrected previously. The accumulated error is then multiplied by the integral gain (*Ki*) and added to the controller output. The integral term accelerates the movement of the process towards setpoint and eliminates the residual steady-state error that occurs with a pure proportional controller. However, since the integral term responds to accumulated errors from the past, it can cause the present value to overshoot the setpoint value.

The derivative term $K_d \cdot de(t)/dt$ slows the rate of change of the controller output. Derivative control is used to reduce the magnitude of the overshoot produced by the integral component and improve the combined controller-process stability. However, the

derivative term slows the transient response of the controller. Also, differentiation of a signal amplifies noise and thus this term in the controller is highly sensitive to noise in the error term, and can cause a process to become unstable if the noise and the derivative gain are sufficiently large. In some case, the derivative term is disabled by setting $K_d = 0$. The lack of deviative action makes the system steadier in the steady state in the case of noisy data.

In the experiments, the K_p is set to inverse of the slop for the demodulated curve, the integral gain K_i is set to 0.01, and the derivative gain K_d is set to 0.

5.4.4 Design of modulator

In the previous sensors, the signal to drive IM is either generated by the sum of three FGs or an AWG. They are easy to operate, buth high cost, especially at frequency up to hundreds of MHz or even higher. In our research a RM sideband modulator is designed to drive the IM.

The signal to drive IM is written as

$$\begin{aligned} F(t) &= \cos(\Omega_S t) + \cos(\Omega_S t + \Omega_M t) - \cos(\Omega_S t - \Omega_M t) \\ &= \cos(\Omega_S t) - 2\sin(\Omega_S t)\cdot\sin(\Omega_M t). \end{aligned} \tag{5.7}$$

This waveform can be generated using quadrature amplitude modulation (QAM). The QAM has been widely used in communication, and the modulator is commercial available at low cost. In the experiments, we developed a modulator based on a quadrature modulator ADL5386 chip (Analog Devices Inc.).

The sideband modulator is shown in Fig. 5-16. The ADL5386 is a quadrature modulator, operates over a frequency range of 50 MHz to 2200 MHz. It takes signals from two differential baseband inputs and modulates them onto two carriers in quadrature with each other. The two internal carriers are derived from a single-ended, external local oscillator (LO) input signal at twice the frequency as the desired output. The LO interface generates two LO signals at 90° of phase difference to drive two

mixers in quadrature. The ADL5386 has two double-balanced mixers: one for the in-phase channel (I channel) and one for the quadrature channel (Q channel). The outputs of the mixers are combined in the differential-to-single-ended amplifier, which provides a 50 Ω output interface.

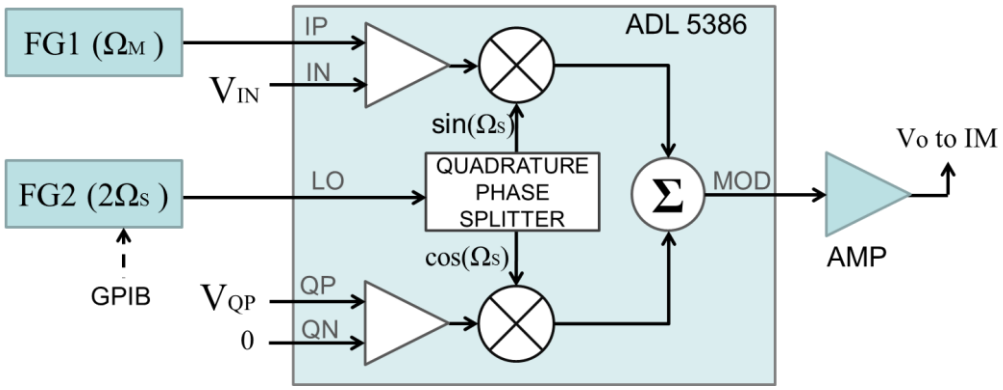

(a)

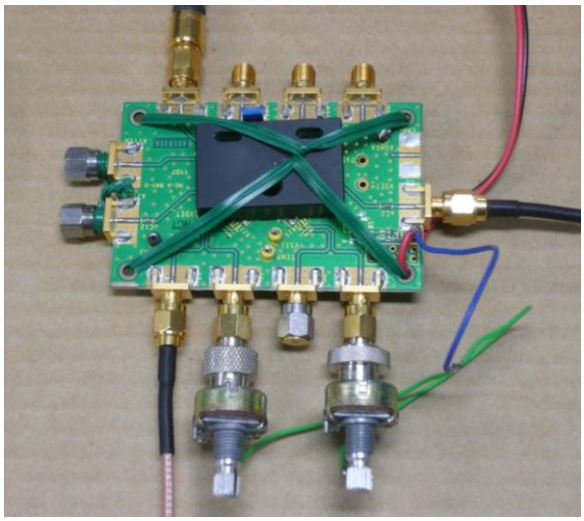

(b)

Fig. 5-16 Sideband modulator. (a) Schematic configuration. FG1, Agilent 32250A; FG2, Agilent 8644A; AMP, RF power amplifier. (b), Photo of the modulator

The LO signal is a sine function generated from a function generator (HP 8644A, 0.26 ~1030MHz). The frequency of the signal is controlled by computer via GPIB

interface. The inputs for I and Q channels are both differential configured, and they only accept positive voltage. The modulation frequency Ω_M is on the positive connector of I channel (IP). It is a sine function with $V_{p\text{-}p}$ of 1V and a biased voltage of 0.5 V generated from a function generator (Agilent 33250A). The negative connector of I channel (IN) is provided a bias voltage of 0.5 V by a resister circuits. The Q channel is also provided a tunable voltage by a register circuit.

The output power from ADL 5386 is too small to drive the IM directly. Its amplitude is amplified to about 3V ($V_{p\text{-}p}$) by a RF power amplifier (APM). Since the bandwidth of ADL 8536 is 50 ~ 2200 MHz, and the frequency range of HP 8644A is 0.26 ~ 1030 MHz, the output frequency range is thus 50 ~ 515 MHz.

5.4.5 Real-time sensor configuration

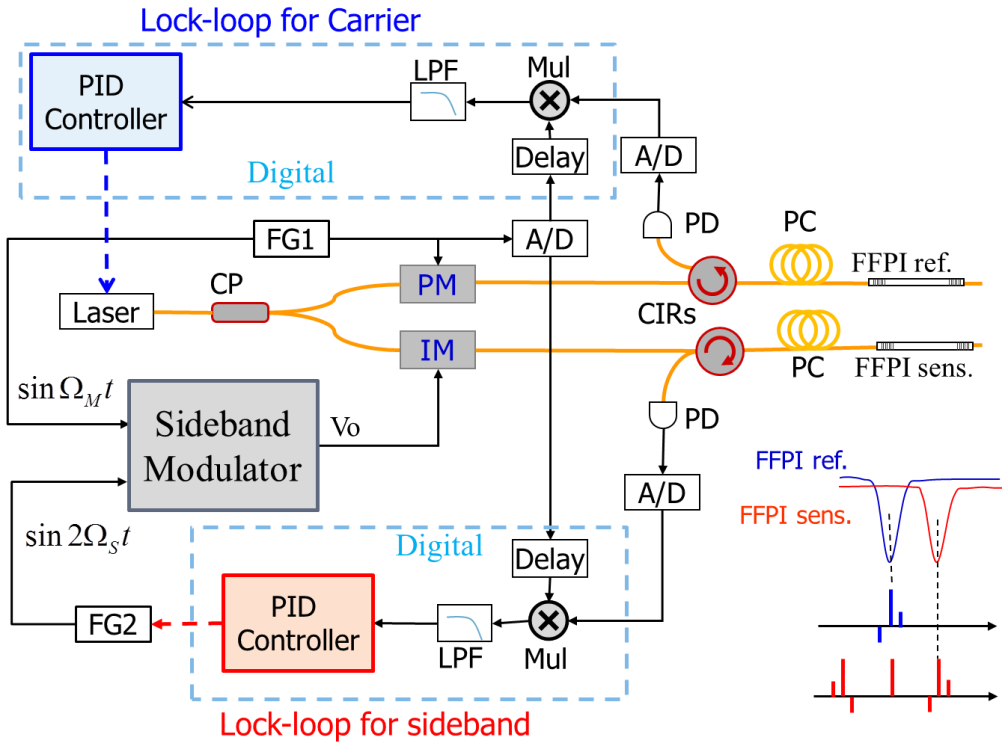

Fig. 5-17 Schematic configuration of real-time strain sensor with sideband.

The system configuration is shown in Fig. 5-17. Compared with previous configuration, the IM is driven by the signal from the sideband modulator. With this modulator, the sideband frequency shift range from carrier is 50 ~ 515 MHz. Corresponding the strain-frequency coefficient of 116 MHz/με of the FFPI under test, a sensing range of 4 με is available. This dynamic range can be significantly improved in practice by switching between different resonances, because the FFPI is capable of resonating at tens of frequencies.

The modulating frequency from FG1 is set to a high frequency of 5 MHz, larger than the bandwidth of the FFPIs. When the sideband is set close to the resonance difference between the FFPIs, the demodulated signals for both FFPIs during laser frequency sweeping is shown in Fig. 5-18. There are two reasons for choosing high modulation frequencies in the real-time sensing configuration. First, compared with low modulation frequency in the previous experiments, the high modulation frequency provides a broader range where the error signal (demodulated signal) has correct sign for feedback control. Second, the demodulated signal has a relative sharp slope with high modulation frequency around resonance, which is helpful to achieve the high SNR in demodulated signals and thus better strain resolution. In Fig. 5-18, the slope for the reference FFPI is 54/MHz, and the slope for sensing FFPI is 71/MHz.

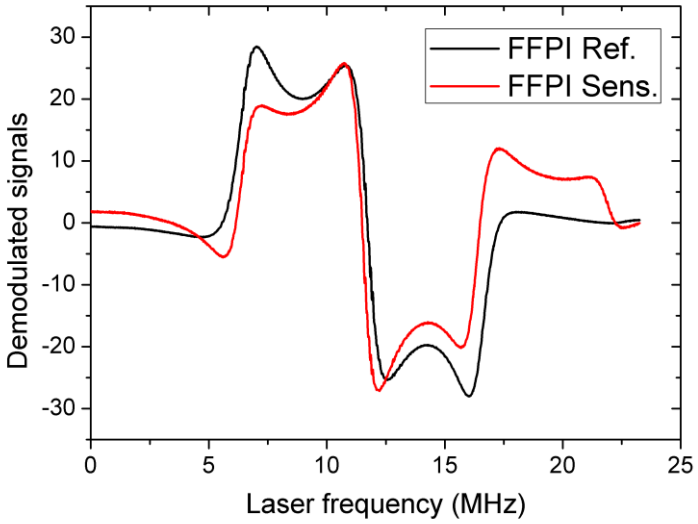

Fig. 5-18 Demodulated signals from FFPIs during laser frequency sweeping with a high modulation frequency, Ω_M = 5 MHz. (Ω_S = 115.8 MHz)

5.4.6 Experimental results

At the beginning, the laser frequency sweeps to find the resonances for both FFPIs. Then, the resonance frequency difference is roughly calculated and Ω_S is set to it. Next, the laser carrier is set to the resonance of the reference FFPI, and the lock loop for carrier is enabled to lock the laser to the resonance. Finally, the lock loop for sideband is enabled to lock the sideband to the resonance frequency of the sensing FFPI. The frequency of Ω_S is equal to the resonance difference between the FFPIs if both lock loops work perfectly.

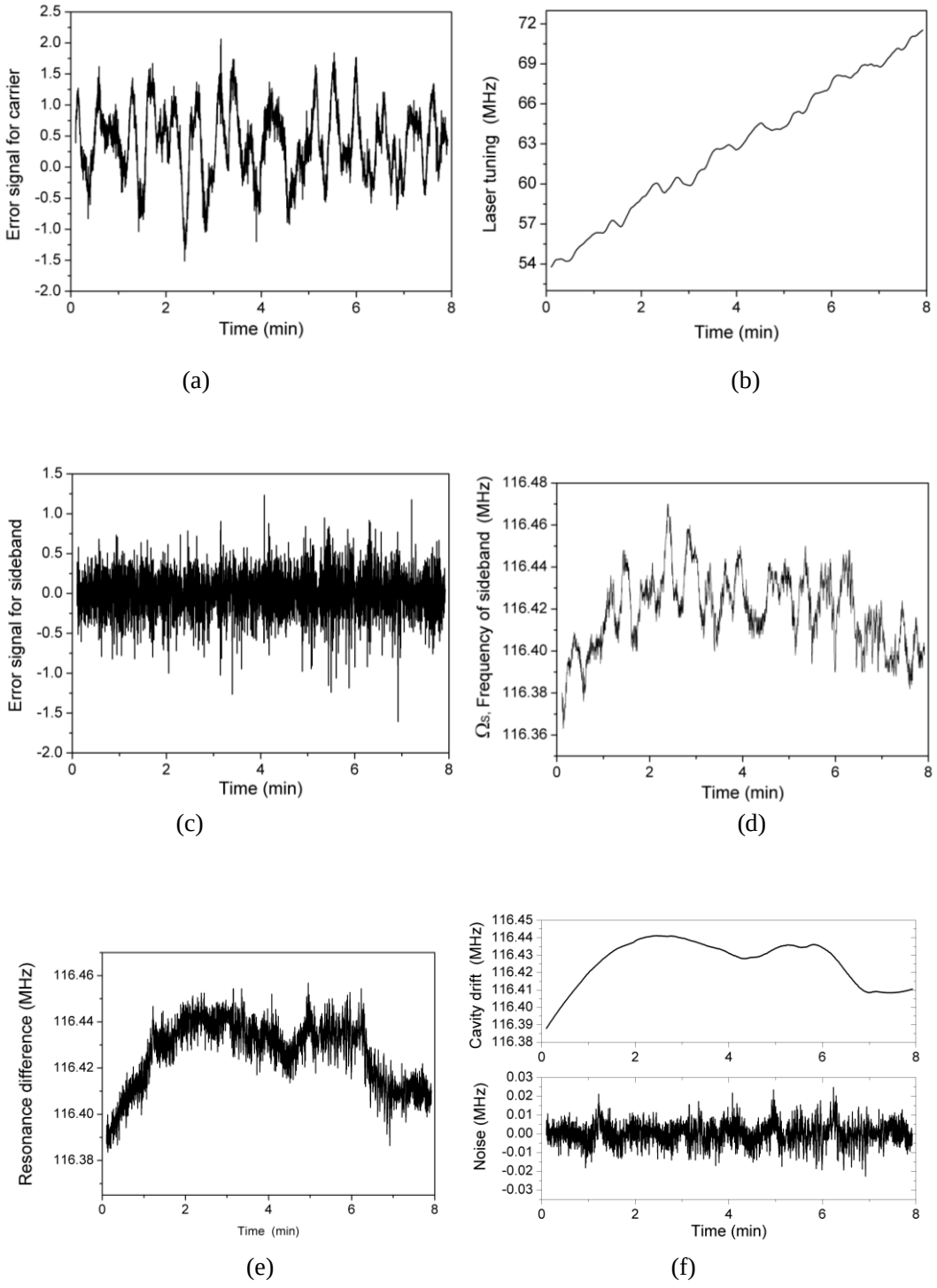

Fig. 5-19 Experimental results. (a). Error signal for the interrogation of reference FFPI interrogated by carrier; (b). Tuning frequency of laser; (c). Error signal for the interrogation of sensing FFPI; (d). Sideband frequency shift from carrier, $\Omega_{S;}$ (e) Calculated resonance difference between the sensing and reference FFPIs; (f). The calculated resonance difference is divided into actual resonance difference and the random error.

Experimental results after both lock loops are enabled are shown in Fig. 5-19. (a) is the demodulated signal from the interrogation of reference FFPI with carrier; i.e., the error signal for the carrier lock loop control. Due to the thermal fluctuation of the FFPIs, as well as the active thermal control of the fiber laser, there are always quick nonlinear frequency fluctuations between the laser and the FFPIs. The detuning is unavoidable for the lock loop to trace these frequency fluctuations. However, this detuning range could be further suppressed using a lock loop with fine adjusted PID parameters. According to the coefficient of 54/MHz, the frequency detuning between the laser and reference FFPI has standard deviation of 10.5 kHz.

(b) is the tuning frequency of laser, reflecting the resonance frequency drift of reference FFPI and/or the wavelength drift of the fiber laser. A relative quick drift with average speed of 2.5 MHz/min is observed from the figure. This is probably induced by thermal fluctuation of the FFPI. On the other hand, the periodical rolling in the wavelength is believed to be induced by the active thermal controller inside the fiber laser. Although the carrier frequency fluctuates quickly, the locking loop successes to track this fluctuation.

(c) is the demodulated signal from interrogation of sensing FFPI, and also the error signal for the feedback lock loop. The small value and random distribution of the error signal indicts that the sideband is well locked to the resonance of the sensing FFPI. The detuning is calculated to have a standard deviation of 4.0 kHz.

(d) is the sideband frequency shift from carrier, i.e., Ω_S. It is not smooth, with low frequency structures inside in the figure. Compared with (a), we can find that the structures in (a) is similar with (d) but opposite in phase. The reason is analyzed as following: Although the sideband is perfectly locked to the sensing FFPI, the carrier detunes from the reference FFPI sometimes, as indicted by figure (a). The sideband frequency Ω_S thus adjust accordingly to compensate the detuning of the carrier. So Ω_S exhibits the same structure as the detuning of carrier. As we have the slope coefficient of

the demodulated signal of the carrier, the detuning of carrier can be compensated, and subtract it from Ω_S to get the resonance difference between FFPIs. The calculated resonance difference is shown in (e).

This curve in (e) could be divided into two curves: a smooth curve and a random error curve, as shown in (f). The random error curve is deduced by the noise of the sensing system and the ambient disturbance. The standard deviation of the error curve is 6.0 kHz. The smooth curve which has a drifting range of 63 kHz, however, is impossible to be caused by the testing system error. In fact, the precision of all the RF signals is better much than 1 kHz, and they are negligible in this system. The laser linewidth is 1 kHz and is also negligible. The carrier is locked to the reference FFPI with error of 10 kHz (it can be compensated as we have done), and the sideband is locked to the sensing FFPI with error no larger than 4.0 kHz. So the error in the sensing system is no larger than 16 kHz. The drifting range of 63 kHz can only be the actual resonance difference drift of the FFPIs, corresponding to thermal difference of 5.0×10^{-5} ℃. The sensor is capability of measuring resonance frequency change of 6.0 kHz, corresponding to a strain resolution down to 51 pε if the FFPIs are properly packaged as a strain sensor head.

In the experiments, the updating frequency of the lock loop is about 7 Hz, only limited by the response speed of the FG (HP 8644A) while adjustin its frequency via GPIB interface. Much higher measuring frequency is possible with a high response FG. According to the sampling speed and data length in data processing, the updating frequency can reach 10 kHz.

5.5 Conclusion

In this chapter, we developed a novel sideband interrogation technology to measure the resonance frequency difference between a pair of FFPIs. The principle of the

sideband interrogation, the design of modulator, and the experiments are discussed in detail. With this technique, extreme high static strain resolution of 0.3 nε is achieved. Using a special designed sideband modulator, real-time strain sensing is achieved with strain resolution down to 0.05 nε. With the extreme-high resolution, this sensor meets the strictest standard for geophysical research.

Chapter 6.
Multiplexed FFPI sensors with dual-modulation technique

Multiplexed sensing is one of the unique advantages for optical sensors. In this chapter, we proposed a dual-modulation technology to realize multiplexing sensing using identical FFPIs wita a novel dual-modulation technology. The principle of the dual-modulation and the demodulation configuration are discussed, and verified by numerical simulation. The modulator design and driving signal are also discussed.

6.1 Multiplexed optical fiber sensors

An optical fiber sensing system is defined as multiplexed system if the number of souces or detectors is smaller than that of the sensor heads [18]. In a location-multiplexed strain sensing system, each sensor is normally designed to detect the strain of only one position, so that we require recovering both the strain and position signals of each sensor. Multiplexing sensor is different from the distributed sensor, which has only one sensing element, and the system can recover the strain as a function of position along the sensing element.

The key work for multiplexing sensor is to distinguish the signals of each sensing element. At least one parameter of lightwave is divised corresponding to each sensing element. The multiplexing technology is cataloged by the parameter of lightwave for division, including time, frequency, wavelength, coherence and polarization.

The wavelength division multiplexing (WDM) is the most common technique for multiplexed fiber sensor [40-43]. The sensors have to be different in wavelength, which making the fabrication of sensors heads a little difficult. The laser has to cover all the spectra of the sensor heads using a large range tunable narrow linewidth laser. The time consumed during wave sweeping limits the measure speed, and the cost is high. The time division multiplexing (TDM) technology uses pulses to interrogate the sensor heads, and the reflected lightwave for each sensor head is different in time because of the different distance [44-47]. It is capable of very long sensor distance, and each sensor could be identical, but the resolution is relative low. The coherence and polarization division techniques are also reported in literature [48, 49], but they do not exhibits advantages for the high resolution sensors.

The FFPI sensors have realized ultra-high strain resolution in our previous work. Together with multiplexing technology, they provide an ideal tool for geophysical measurements. The frequency division multiplexing technology is employed in our research, with which multiplexed sensing is obtained using identical FFPIs as sensor heads. As the interrogation technology for FFPI already involves a frequency modulation, the commen frequency division technique such as optical frequency domain reflectometry (OFDR) cannot be used directly. A dual-modulation technique is developed for multiplexing FFPI sensors.

6.2 Multiplexed FFPI sensors with dual-modulation technology

6.2.1 Review on the FM configuration

Fig. 6-1 is a configuration of FFPI sensors using frequency modulation technology. Compared with the typical setup in chapter 4, there are two identical FPs cascaded in one fiber. Let’s have a look on the response of the system again.

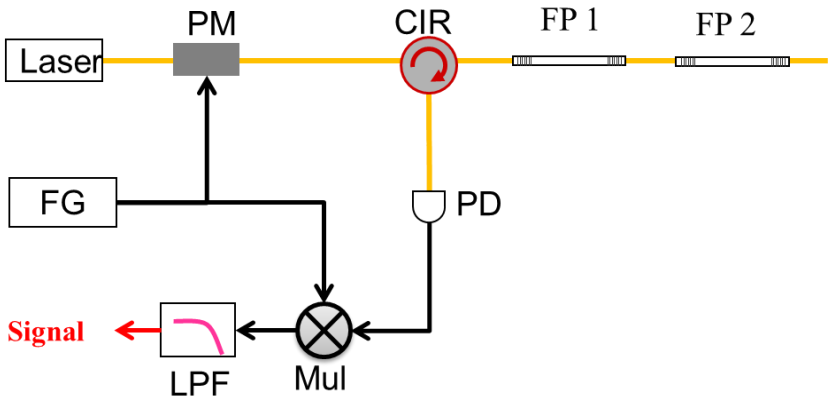

Fig. 6-1 Interrogation of multiple FPs with FM technology

The response of FFPI when the laser is close to the resonance is given by Eq. (4.19) in chapter 4. It is further simplified to be

$$F(\delta\omega) \approx ik \cdot \delta\omega, \tag{6.1}$$

where the k is a constant determined by the finesses and V_{FSR} of the FP cavity. The laser after the phase modulator has the form as

$$E_1 = J_0 e^{i\omega t} + J_1 e^{i(\omega+\Omega)t} - J_1 e^{i(\omega-\Omega)t} \tag{6.2}$$

The reflected beam by FP1 has the form as following

$$E_{FP1} = ik\left(J_0 e^{i\omega t}\cdot\delta\omega_1 + J_1 e^{i(\omega+\Omega)t}\cdot(\delta\omega_1+\Omega) - J_1 e^{i(\omega_1-\Omega)t}\cdot(\delta\omega_1-\Omega)\right), \tag{6.3}$$

here $\delta\omega_1$ is the deviation between the laser and the resonance, and Ω is the modulation frequency of the phase modulator, smaller than the bandwidth of the FP cavity. In the case that the laser and sidebands are all close to the resonance of the FFPIs, the refection is small and the transmission is close to 1. In this case, the incident light to FP2 is almost the same as for the FP1, and the reflected lightwave by FP2 can also pass through FP1 with very small disturbance. The reflected beam arriving at photo-diode is

$$E_{FP2} = ik\left(J_0 e^{i\omega t}\cdot\delta\omega_2 + J_1 e^{i(\omega+\Omega)t}\cdot(\delta\omega_2+\Omega) - J_1 e^{i(\omega-\Omega)t}\cdot(\delta\omega_2-\Omega)\right) \tag{6.4}$$

here $\delta\omega_2$ is the deviation between the laser and the resonance of FP2. So the detected power at photo-diode is

$$\begin{aligned} I &= \left(E_{FP1} + E_{FP2}\right)\left(E_{FP1} + E_{FP2}\right)^* \\ &= k^2\left((\text{constant terms}) + 4J_0J_1\left(\delta\omega_1 + \delta\omega_2\right)\Omega\cos\Omega t + (2\Omega \text{ terms})\right). \end{aligned} \tag{6.5}$$

It is found that the demodulated signal is the sum of frequency detuning for both FFPIs, and it is impossible to detect the detuning of each FFPI. In other words, the demodulated signal would be the sum of applied strain to all the FFPI sensor heads if it is used as strain sensing. Modification to the configuration is necessary to achieve multiplexed sensing.

The above analysis also reveals that, the frequency detuning information is coded in the complex amplitude of the carrier when it is reflected by the FFPI. If two identical FFPI is cascaded in one fiber, the total reflected carrier is the sum of the two FFPI. In order to achieve multiplexed sensing, FFPIs from different position must be distinguished. An effective method is to code the signal from different FFPIs at different frequency, instead of a dc signal.

6.2.2 Dual-modulation technology

As shown in Fig. 6-2, two sidebands are generated as well as the original sidebands generated by the phase modulator. The electric field of the beam is

$$E_0 = J_0e^{i\omega t} + J_1e^{i(\omega+\Omega)t} - J_1e^{i(\omega-\Omega)t} + ge^{i(\omega+\Theta)t} + ge^{i(\omega-\Theta)t} \tag{6.6}$$

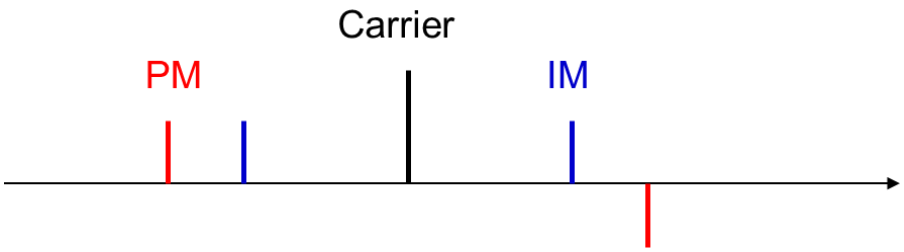

Fig. 6-2 The spectrum of dual modulated signal

First we only consider the reflected beam by FP1 which is

$$\begin{aligned} E_{FP1} &= ik\cdot[J_0 e^{i\omega t}\cdot\delta\omega_1 + J_1 e^{i(\omega+\Omega)t}\cdot(\delta\omega_1+\Omega) - J_1 e^{i(\omega-\Omega)t}\cdot(\delta\omega_1-\Omega) \\ &+ ge^{i(\omega+\Theta)t}\cdot(\delta\omega_1+\Theta) + ge^{i(\omega-\Theta)t}\cdot(\delta\omega_1-\Theta)] \end{aligned} \tag{6.7}$$

So the detected power at photo-diode is

$$\begin{aligned} I_{FP1} &= k^2[(\text{constant terms}) + 4J_0J_1\delta\omega_1\Omega\cos\Omega t + 4J_0 g(\delta\omega_1)^2\cos\Theta t \\ &+ 2J_1 g(\delta\omega_1+\Omega)(\delta\omega_1+\Theta)\cos(\Omega-\Theta)t - 2J_1 g(\delta\omega_1-\Omega)(\delta\omega_1-\Theta)\cos(\Omega-\Theta)t \\ &+ 2J_1 g(\delta\omega_1+\Omega)(\delta\omega_1-\Theta)\cos(\Omega+\Theta)t - 2J_1 g(\delta\omega_1-\Omega)(\delta\omega_1+\Theta)\cos(\Omega+\Theta)t \\ &+ (2\Omega\text{ terms}) + (2\Theta\text{ terms})]. \\ &= k^2[(\text{constant terms}) + 4J_0J_1\delta\omega_1\Omega\cos\Omega t + 4J_0 g(\delta\omega_1)^2\cos\Theta t \\ &+ 2J_1 g\delta\omega_1(\Theta+\Omega)\cos(\Omega-\Theta)t + 2J_1 g\delta\omega_1(\Theta-\Omega)\cos(\Omega+\Theta)t \\ &+ (2\Omega\text{ terms}) + (2\Theta\text{ terms})] \end{aligned} \tag{6.8}$$

There are several frequency components in the demodulated, including Ω, Θ, Ω – Θ, Ω + Θ and the second harmonic frequencies. The target of our configuration is to determine the value of $\delta\omega_1$. The term of frequency Θ is negligible because it is much smaller than other terms as $\delta\omega_1$ closing to zero. Although $\delta\omega_1$ can be detected from the any of the remaining 3 terms, it should be pointed out that the term with frequency of Ω – Θ is the most suitable. Compared with the Ω + Θ term, it has larger coefficient which results in higher signal-to-noise ratio, and lower frequency reducing the difficulty for demodulation. As for the Ω term, all FFPIs have contribution to this term and cannot be distinguished, as we have analyzed in the above section.

Now we consider the total beam reflected from both FP1 and FP2. In order to distinguish the demodulated signals of the two FFPIs, both Ω and Θ are modulated vary with time. The electric field of the reflected beam is

$$\begin{aligned} E_{tot} &= ik\cdot[J_0 e^{i\omega t}\cdot\delta\omega_1 + J_1 e^{i(\omega+\Omega_1)t}\cdot(\delta\omega_1+\Omega_1) - J_1 e^{i(\omega-\Omega_1)t}\cdot(\delta\omega_1-\Omega_1) \\ &+ ge^{i(\omega+\Theta_1)t}\cdot(\delta\omega_1+\Theta_1) + ge^{i(\omega-\Theta_1)t}\cdot(\delta\omega_1-\Theta_1) \\ &+ J_0 e^{i\omega t}\cdot\delta\omega_2 + J_1 e^{i(\omega+\Omega_2)t}\cdot(\delta\omega_2+\Omega_2) - J_1 e^{i(\omega-\Omega_2)t}\cdot(\delta\omega_2-\Omega_2) \\ &+ ge^{i(\omega+\Theta_2)t}\cdot(\delta\omega_2+\Theta_2) + ge^{i(\omega-\Theta_2)t}\cdot(\delta\omega_2-\Theta_2)]. \end{aligned} \tag{6.9}$$

Here the value of Ω and Θ are different for the two FPs because they have different distance from the laser. The detected power at photo-diode is

$$
\begin{aligned}
I_{tot} = k^2 \cdot [&(\text{constant terms}) \\
&+ 4J_0 J_1 (\delta\omega_1 + \delta\omega_2)(\Omega_1 \cos\Omega_1 t + \Omega_2 \cos\Omega_2 t) \\
&+ 4J_0 g\left((\delta\omega_1)^2 + (\delta\omega_2)^2\right)(\cos\Theta_1 t + \cos\Theta_2 t) \\
&+ 2J_1 g\delta\omega_1(\Theta_1 + \Omega_1)\cos(\Omega_1 - \Theta_1)t \\
&+ 2J_1 g\delta\omega_1(\Theta_1 - \Omega_1)\cos(\Omega_1 + \Theta_1)t \\
&+ 2J_1 g\delta\omega_2(\Theta_2 + \Omega_2)\cos(\Omega_2 - \Theta_2)t \\
&+ 2J_1 g\delta\omega_2(\Theta_2 - \Omega_2)\cos(\Omega_2 + \Theta_2)t \\
&+ 4J_1^2(\delta\omega_1\delta\omega_2 + \Omega_1\Omega_2)\cos(\Omega_1 - \Omega_2)t \\
&- 4J_1^2(\delta\omega_1\Omega_2 + \delta\omega_2\Omega_1)\cos(\Omega_1 + \Omega_2)t \\
&+ 4kg(\Omega_1\delta\omega_2 + \Theta_2\delta\omega_1)\cos(\Omega_1 - \Theta_2) \\
&- 4kg(\Theta_2\delta\omega_1 - \Omega_1\delta\omega_2)\cos(\Omega_1 + \Theta_2) \\
&+ (2\Omega \text{ terms}) + (2\Theta \text{ terms})]
\end{aligned}
\tag{6.10}
$$

Now we have several frequency components listed in Eq.(6.10). The terms only related to $\delta\omega_1$ or $\delta\omega_2$ can be used for demodulation of the sensor. Terms that satisfies this requirement are $2k^2J_1g\delta\omega_1(\Omega_1+\Theta_1)\cdot\cos(\Omega_1-\Theta_1)$, $2k^2J_1g\delta\omega_1(\Omega_1-\Theta_1)\cdot\cos(\Omega_1+\Theta_1)$, $2k^2J_1g\delta\omega_2(\Omega_2+\Theta_2)\cdot\cos(\Omega_2-\Theta_2)$, and $2k^2J_1g\delta\omega_2(\Omega_2-\Theta_2)\cdot\cos(\Omega_2+\Theta_2)$. If the Ω and Θ are modulated properly, those terms have identical frequency compared with other terms and can be distinguished without cross-talk. Among those components, the first and third term can be chosen for the demodulation of the $\delta\omega_1$ and $\delta\omega_2$, respectively. They have the advantages of large value and lower frequency compared with the other two terms.

The other terms become noises in the interrogation. The frequencies of Ω and Θ and demodulation methods have to be well configured to achieve a high signal to noise ratio, and finally a high strain resolution.

6.2.3 Modulation function configuration

A possible modulation configuration is a linear sweep of the frequency for Ω and Θ. Considering a modulation functions with instant frequency of

$$\Omega_1 = 15\text{-}10t,\ \Omega_2 = 15\text{-}10(t+\Delta t) \tag{6.11}$$

$$\Theta_1 = 5+10t,\ \Theta_2 = 5+10(t+\Delta t) \tag{6.12}$$

here the unit of frequency and time is omitted for simple, $0 < t < 1$, and Δt is the time delay for light reflected by the two FFPIs. Now we have the frequency components in the detected power at photo-diode, listing as

$$\Omega_1 - \Theta_1 = 10 - 20t \tag{6.13}$$

$$\Omega_2 - \Theta_2 = 10 - 20t - 20\Delta t \tag{6.14}$$

$$\Omega_1 + \Theta_1 = \Omega_2 + \Theta_2 = 20 \tag{6.15}$$

$$\Omega_1 + \Omega_2 = 30 - 20t - 10\Delta t \tag{6.16}$$

$$\Theta_1 + \Theta_2 = 10 + 20t + 10\Delta t \tag{6.17}$$

$$\Omega_1 - \Omega_2 = 10\Delta t \tag{6.18}$$

$$\Theta_1 - \Theta_2 = -10\Delta \mathrm{t} \tag{6.19}$$

$$\Omega_1 + \Theta_2 = 20 + 10\Delta t \tag{6.20}$$

$$\Omega_2 + \Theta_1 = 20 - 10\Delta t \tag{6.21}$$

$$\Omega_1 - \Theta_2 = \Omega_2 - \Theta_1 = 10 - 20t - 10\Delta t \tag{6.22}$$

The frequency components is shown in Fig. 6-3 when $\Delta t = 0.1$. The thick blue and red lines indict the Eq. (6.13) and (6.14), respectively. Their frequencies are unique from all the other components, and so it is possible to be demodulated correctly. However, their frequencies are not a constant but varying with time. Simple Fourier transform or the lock-in amplifier cannot deal with this type of signals. A cross-correlation algorithm is used for the demodulation.

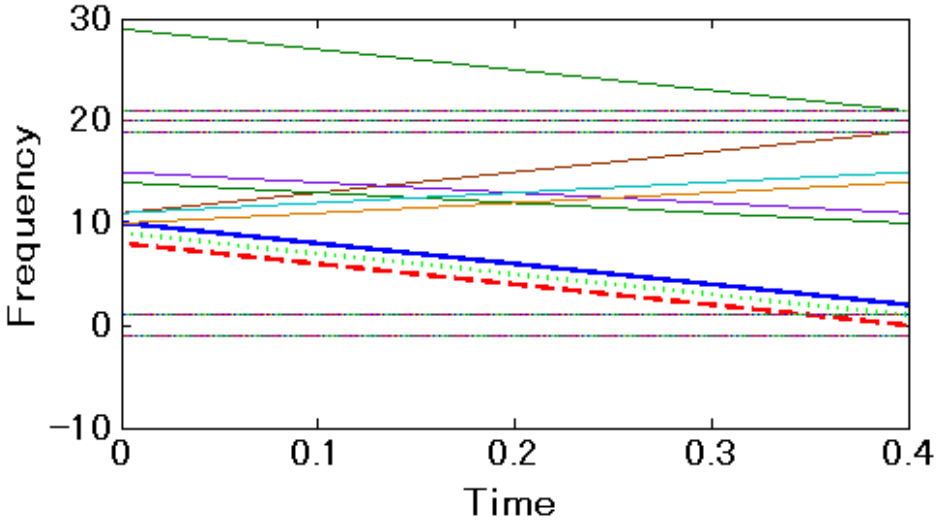

Fig. 6-3 Frequency components at photo-diode. The thick blue and red lines are the signals to be retrieved.

6.2.4 Demodulation with cross-correlation algorithm

The cross-correlation algorithm has been introduced in chapter 2. The reflected power of the photo-diode has the entire frequencies listed by Eqs. (6.13) to (6.22). It is sampled with a high speed A/D convertor. A reference signal is generated as

$$f(t) = \cos\left(10t - 10t^2\right) \tag{6.23}$$

The instant frequency is the same as Eq.(6.13), and has a time delay compared with Eq. (6.14). The cross-correlation product between the sampled power I_{tot} and the reference signal $f(t)$ is calculated as

$$C(\tau) = \int I_{tot}(t) \cdot f(t+\tau) dt. \tag{6.24}$$

The cross-correlation production has peak at τ = 0, and theintensity of the peak reveals the value of $\delta\omega_1$. Another peak appears at τ = -2Δt, with intensity of $\delta\omega_2$. It should be noticed that Eq. (6.22) also has the same slope of frequency, but with different frequency shift between Eq. (6.13) and Eq. (6.14). This term also has a peak in the cross-correlation production.

6.3 Numerical simulation

Numerical simulation is carried out to verify the demodulation using cross-correlation algorithm.

6.3.1 Simulation configuration

Matlab programs are used for the simulation of demodulation. The modulation frequencies linearly sweep, as shown Eq. (6.11) and Eq. (6.12). The frequency is set to lower value due to the calculation ability of computer. The frequency of modulation is linear chirped, so all the calculation has to be done numerically. The sample frequency should be much larger than the signal frequency to reduce the error. Δt = 0.1 in the simulation, and the time range of t is from 0 to 0.4. The unit of frequency is set with different values in different simulation.

As shown in Fig. 6-3, the interested frequencies lie in the range of 0 and 10. The higher frequencies can be suppressed by a low pass filter before the analog-to-digital converter. The low frequencies of $\pm 10\Delta t$, given by Eqs. (6.18) and (6.19), are constant so that they can also be removed with band stop filter. In the simulation, it is supposed that only three frequencies remain, given by Eqs. (6.13), (6.14) and (6.22). The first two components contain the information of frequency detuning between the laser and the FFPIs, i.e. the strain information. The work of the demodulation is to recover the coefficient of the two terms.

6.3.2 Simulation results

First, the frequency unit of the modulation Eqs. (6.11) and (6.12) is set to 100 Hz. With the instant frequencies given at above sections, the detected power at photo-diode after the low pass filter and band-stop filter is

$$\begin{aligned} I_{sim1} = &\cos\left[\left(10-10t\right)t\cdot 200\pi\right]+\cos\left[\left(8-10t\right)t\cdot 200\pi\right] \\ &+\cos\left[\left(9-10t\right)t\cdot 200\pi\right] \end{aligned} \tag{6.25}$$

With the reference signal, we get the cross-correlation product as

$$C(\tau)=\int_0^{0.4}\cos\left[\left(10-10\left(t+\tau\right)\right)\cdot\left(t+\tau\right)\cdot 200\pi\right]\cdot I_{sim1}\cdot dt \tag{6.26}$$

The demodulated cross-correlation production is shown in Fig. 6-4 (a). The horizontal axis is the time delay of τ. A peak appears at τ = 0, corresponding to the term of Eq. (6.13). The amplitude of the peak is determined by the value of $\delta\omega_1$. The peak at τ = 0.1 indicts the term of Eq. (6.14). The horizontal position of this peak is exactly the time delay of Δt that we set. The distance of FFPI and the applied of strain can be obtained simultaneously using this configuration. The peak at τ = 0.1 is shown in further shown in Fig. 6-5 (a).

Different modulation frequency unit is also tested and compared under the same configuration, including 100 Hz, 500 Hz and 1 kHz. Fig. 6-4 shows that the modulation frequency almost has no influence on the sensitivity of the sensor. Fig. 6-5 indicts that higher modulation could improve the special resolution, i.e. the distance of FFPIs could be smaller.

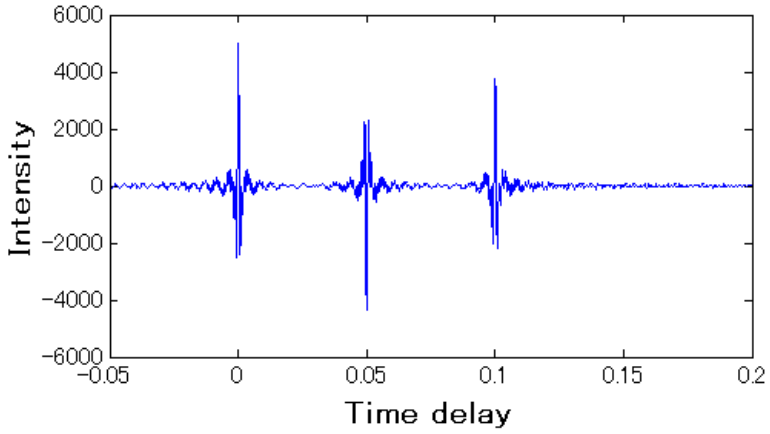

(a) Frequency unit: 100 Hz.

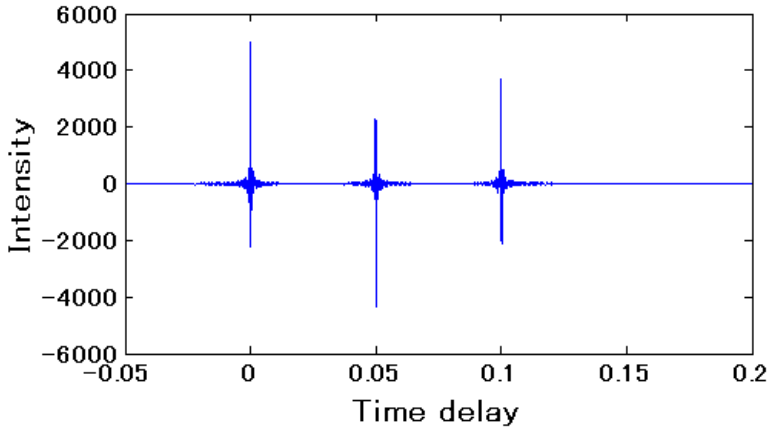

(b) Frequency unit: 500 Hz.

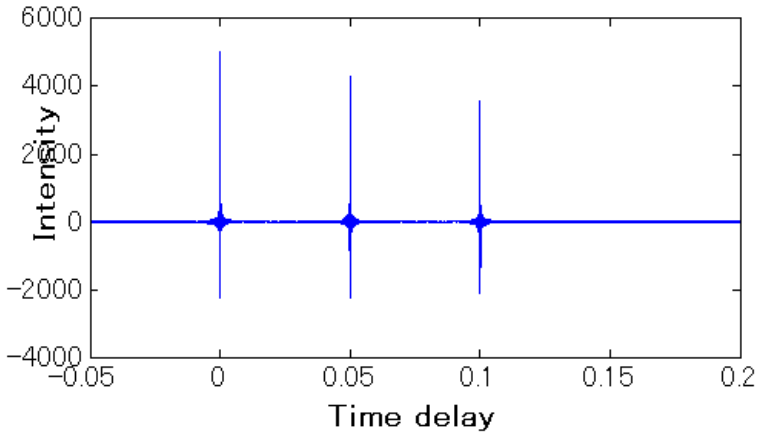

(c) Frequency unit: 1 kHz.

Fig. 6-4 Demodulated signal by cross-correlation algorithm with different modulation frequency.

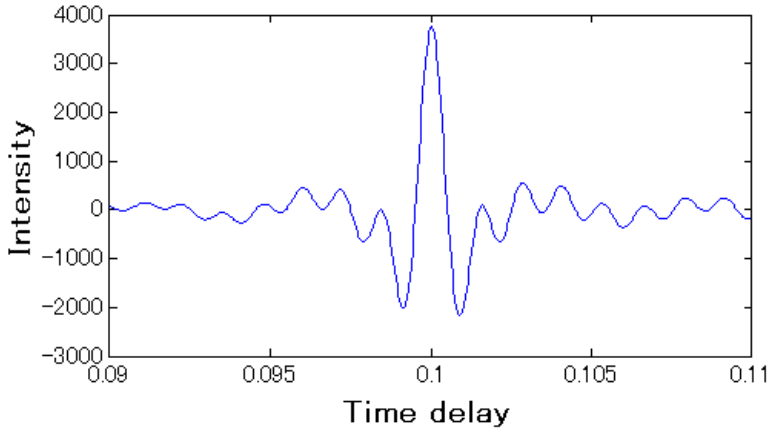

(a) Frequency unit: 100 Hz.

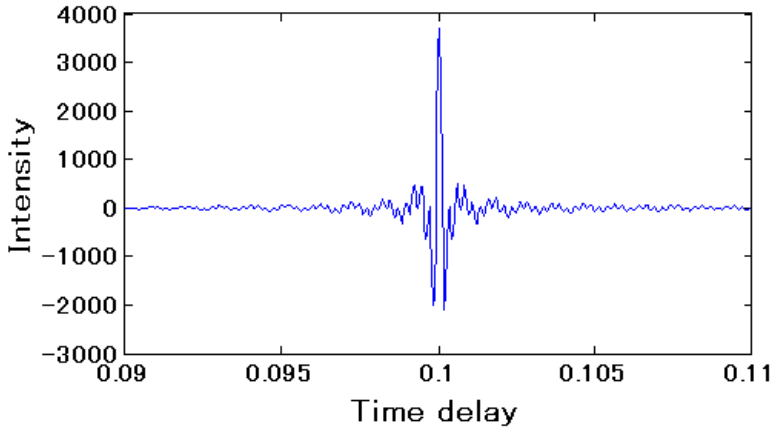

(b) Frequency unit: 500 Hz.

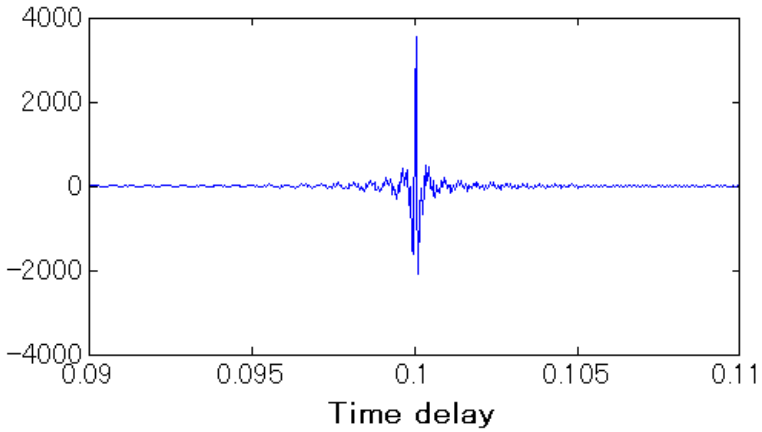

(c) Frequency unit: 1 kHz.

Fig. 6-5 The peak around τ = 0.1with different modulation frequency.

6.3.3 Limintation of sensor head number

As the number of sensor increases, the frequency components at the photo-diodes become more complicated. As shown in Fig. 6-3, when there are two FFPIs, a fake peak will appear together with the two peaks for the two FFPIs, with the amplitude of the sum for the two peaks. When there are three FFPIs in the system, there will be four fake peaks together with the three ture peaks for the three FFPIs. These fake peaks will cause cross-talk problems if the distance of the FFPIs are not proper arranged. This problem becomes more serious as the number of the FFPI sensor head increases. So the capability of multiplexing is limited to 3 sensor heads with this dual- modulation technique.

6.4 Modulator for dual-modulation

The modulation configuration to generate lightwave with form as Eq. (6.6) is discussed in this section.

6.4.1 Modulator design

The proposed modulator uses a commercial available differential quadrature phase shift keying (DQPSK) modulator (Thorlabs, LN86S). The LN86S is a Dual-Parallel, Titanium-indiffused, x-cut Lithium Niobate modulator. The front end of the LN86S is a phase modulator which allows for the required phase control in the signal channel. The back end of the modulator consists of two Mach–Zehnder interferometers (MZI)s in parallel as shown in Fig. 6-6.

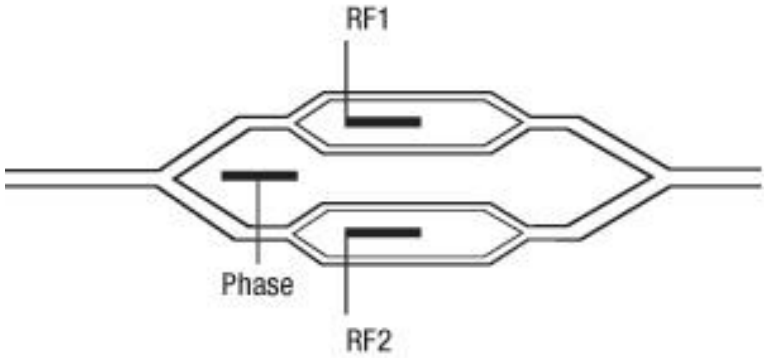

Fig. 6-6 Structure of DQPSK modulator LN86S

In this dual-parallel modulator, the incoming signal is equally split into two legs and sent through a low speed phase modulator, as shown in Fig. 6-6. The phase modulator serves the purpose of applying a phase delay between the legs. The signals in each leg are then sent through separate intensity modulators. The outputs of each intensity modulator's legs are re-combined to form the output signal of the dual-parallel modulator. This resultant re-combined signal forms a DQPSK signal through the interference effects.

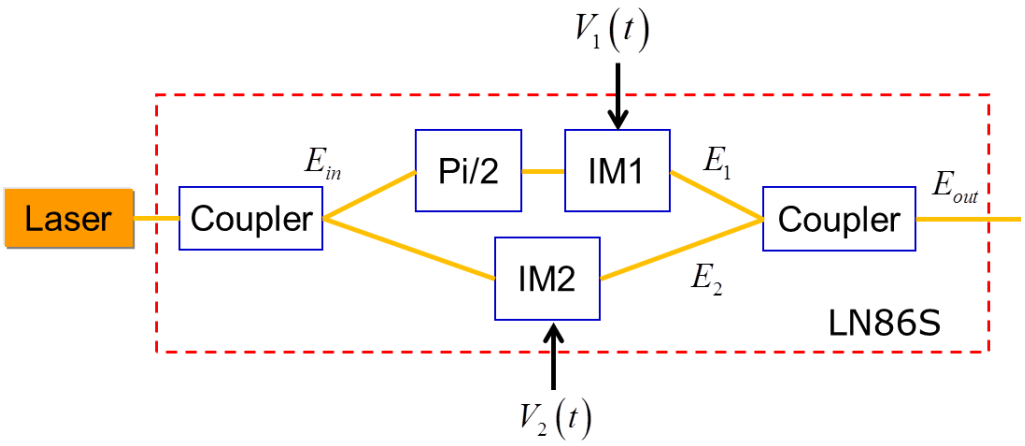

Fig. 6-7 Modulation configuration using DQPSK modulator

The proposed modulator is shown in Fig. 6-7. The transmission of the two IMs in the figure are $T_1(t)$ and $T_2(t)$, respectively. The re-combined electric field of light is

$$E_{out} = T_1 e^{i\omega t} + T_2 e^{i\omega t + i\pi/2} = \left(T_1 + iT_2\right) e^{i\omega t}. \tag{6.27}$$

The output of light should have the same formation as Eq. (6.6), which is written as

$$E = \left(J_0 + i2J_1 \sin\Omega t + 2g\cos\Theta t\right) e^{i\omega t}. \tag{6.28}$$

Comparing the two equations, we get

$$T_1 = J_0 + 2g\cos\Theta t \tag{6.29}$$

$$T_2 = 2J_1 \sin\Omega t \tag{6.30}$$

From these equations we can design the signal to drive the IMs in the modulator.

6.4.2 Driving signal for modulator

The signal of $V_1(t)$ to drive IM1 is simple. The transmission of MZI is near to linear if it is proper biased and the modulation voltage is small. The driving signal of $V_2(t)$, however, is difficult because it is a pure sine function with zero-bias. The simple solution is that the driving voltage is a linear function of time, $V_2(t) = \Omega t/V_\pi$, where V_π is the parameter of IM2. Then the transmission of IM2 is a sine function. However, $V_2(t)$ cannot increase too high in pracitse.

Instead of a linear increasing line, the $V_2(t)$ can be a triangle waveform as shown in Fig. 6-8. The voltage of for the IM increases from $-V_{pi}$ to V_{pi} in the first half period, and then decreases to $-V_{pi}$ in the next half period. Because the transmission of the IM is periodical, the transmission of IM2 will has the form as Eq. (6.30).

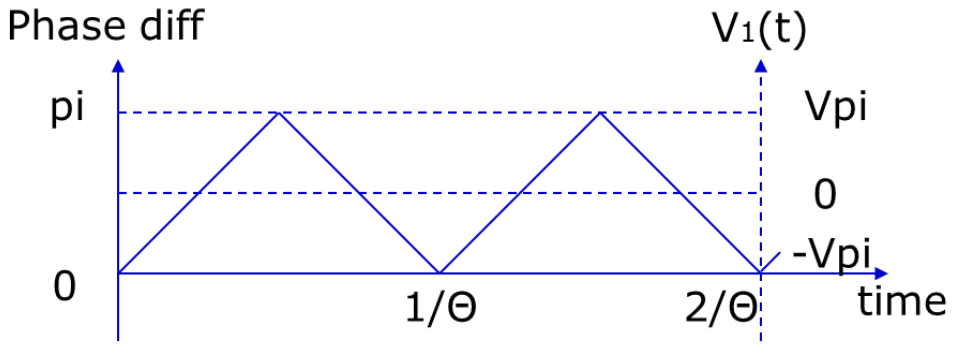

Fig. 6-8 Driving signal for IM2 using triangle waveform.

6.5 Conclusion

In this chapter, we proposed a dual-modulation in order to achieve multiplexed strain sensing using identical FFPIs as sensor heads. The principle and configuration of the dual-modulation is introduced. The demodulation is achieved by using a cross-correlation algorithm. Numerical simulation verifies that the amplitude of strain and the position of FFPI sensor can be obtained simultaneously. A modulator is designed to realize the dual-modulation to the lightwave based on a commercial available DQPSK modulator. The analysis and simulation in this chapter provides sufficient introduction for the development of high resolution multiplexed optical fiber sensors with identical FFPIs.

Chapter 7.
Conclusion

Risk of seismic and volcanic event prevention is one of the most important issues for the life quality improvement in highly populated areas. Those large-scale natural phenomena, however, cannot be simply studied with physical models. The research on the complex phenomena such as earthquakes, eruptions and landslides, is based upon an accurate monitoring on the deformation of the earth. A large mass of strain sensors with an ultra-high strain resolution in the static to low frequency region are required for the geophysical measurements.

Optical fiber sensors are very attractive to the geophysical applications due to their unique advantages such as light weight, small size, low cost, immune to electromagnetic interference, etc. Common optical fiber sensors have static strain resolution on the order of με, and have been widely adopted in applications like structure health monitoring and smart materials, but the strain resolution has to be improved by 2 or 3 orders of magnitude for the geophysical applications. In our research, we have developed a series of ultra-high strain resolution optical fiber sensors aiming at geophysical applications. Lots of effort has been paid to the realization of ultra-high static strain resolution and large measurement range.

Chapters 2 and 3 focus on the FBG static strain sensor interrogated by a narrow linewidth tunable laser. The sensor consists of a pair of FBGs, one for strain sensing and the other for temperature compensation. The Bragg wavelength difference between the two FBGs is evaluated utilizing a cross-correlation algorithm. We theoretically studied the performance of the sensor. The main noise sources are analyzed, and the expression

of resolution is presented. The theoretical prediction agrees well with our experimental result, and well describes the numerical simulations results. With this expression, the guidelines for the optimization of the sensor are discussed in detail. Then we developed a pracitcal FBG strain sensor based on the analysis. A wavelength resolution of 3.1 fm was obtained without strain applied, corresponding to a static strain resolution up to 2.6 nε. With a variable strain applied by a piezo-stage, a resolution of 17.6 nε was demonstrated, mainly limited by the precision of the testing stage. Currently the sensor is put into field test to measure the crustal deformation induced by tide at Aburatsubo Bay, kanagawa, Japan. The deformation induced by oceanic tide is clearly recorded by the FBG sensor with resolution about 10 nε. Compared with the 38m-long extension-meter, the FBG sensor provides a comparable resolution with a much smaller size (1m) and lower cost, providing a powerful tool for geophysical research.

In chapter 4, FFPIs are used as the strain sensing compoenets instead of FBGs, to overcome the wavelength repeatability problem that limits the resolution of FBG sensors. Frequency modulation technology is used to measure the phase reflection of the FFPI instead of the intensity reflection. A digitalized demodulation technique is employed to extract the detuning between the laser frequency and the resonance of FFPIs; then a cross-correlation algorithm is used to calculate the resonance difference between the two FFPIs. An ultra-high static wavelength resolution corresponding to strain resolution down to 5.8 nε was demonstrated in experiment, with dynamic range large than 100 με. The sweeping range of laser is only 5 pm, much smaller than the sweeping range in the FBG sensors.

In chapter 5 we invented a novel sideband interrogation technology, for the simultaneous interrogation of the sensing and reference FFPIs, respectively. A special RF signal is used to drive an intensity modulator to generate a sideband, which is used to interrogate the sensing FFPI, while the laser carrier is used to interrogate the reference FFPI with typical frequency modulation technology. Experiments of static

strain sensing were carried out using a tunable laser, and a cross-correlation algorithm is employed to calculate the resonance difference. With a sweeping rang of only 0.1 pm and measuring period of a few seconds, a standard deviation of measured resonance difference of 29 kHz was obtained, corresponding to a strain resolution of 0.3 nε. Real-time sensing is also achieved by locking the laser carrier and sideband to the two FFPIs, respectively. Strain resolution down to 0.05 nε is demonstrated in experiments with updating frequency of 7 Hz.

In chapter 6, we designed a multiplexed sensor with identical FFPIs using a dual-modulation technology. The principle of dual-modualtion, the demodulation algorithm, and the modulator design are introduced. Numerical simulation results proved that, the strain and the position of FFPI sensor could be measured simultaneously with the dual-modulation technique. The analysis and simulation in this chapter provides sufficient introduction for the development of high resolution multiplexed optical fiber sensors with identical FFPIs.

In this thesis, four types of optical fiber strain sensors have been studied; they are: FBG sensors, FFPI sensors with FM technology, FFPI sensors with sideband interrogation, and multiplexed FFPI sensors with dual-modulation techniques. Each type of sensors has its unique characteristics, and a comparison is list below.

The FBG sensors are simple in configuration. They require a large wavelength sweeping range of laser, and have large dynamic range meanwhile. Multiplexed sensing with WDM technique is easy to realize as we have demonstrated at in situ experiments. The drawback is that it is difficult to further improve the strain resolution.

FFPI sensor with FM technique has good static strain resolution on nε order. The wavelength sweeping range of laser is quite small, so the laser cost can be reduced. They have a large dynamic range up to hundards of με. Although the configuration is a

little complicated compared with the FBG sensors, they are very attractive for some applications.

The FFPI sensor with sideband interrogation technology has extremely high resolution down to sub-nε, because the wavelength nonlinearity during laser sweeping is avoided in this configuration. And it is the only technique for real-time sensing to measure both static and dynamic strain signals. The drawbacks are the complexity and relative small dynamic range. They are suitable for applications that extreme strain resolution is required with a reasonable cost.

The multiplexed FFPI sensors can reduce the cost for applications that lots of sensors are required. The simulation results proved the feasibility for the proposed configuration.

A direct comparison of the sensors is list in Table 3.

Table 3 Comparison of developed optical fiber sensors

Comparison	Resolution	Dynamic range	Both Static & Dynamic	Multiplexed sensing
FBG + Tunable laser	○	◎	×	◎
FFPI + FM technology	○	◎	△	△
FFPI + Sideband interrogation	◎	○	○	△
FFPI + dual-modulation	○	△	△	○

◎: Good; ○: Fair; △: With difficulty; ×: Very difficult .

Acknowledgement

I wish to acknowledge my debt of gratitude to those who have helped me along the way. In particular, I wish to express to the ulmost gratitude to my supervisor, Prof. Zuyuan He, for his continuous and invaluable guidance, support, criticisms and encouragement during the research. I am also grateful to Prof. Kazuo Hotate, Prof. Shinji Yamashita and Mr. Masato Kshi for inspring discussions and support. I am also deeply indebted to Prof. Tomochika Tokunaga and Mr. Katuro Mogi for the cooperation and support in the field experiments.

I am appreciated to all the people at Hotate, Yamashita and He's Lab. I would like to thank our secretaries, Mrs. Masuhara, Mrs. Machida, Mrs. Sayama, Mrs. Wakabayashi, and Mrs. Mizuno for their kind help in various aspects; I would thank Dr. Amos Martinez, Dr. Weiwen Zou, Dr. Yosuke Mizuno, Dr. Koji Kajiwara, Dr. Xijing Wang and Dr. Huilian Ma, for shaing their experiences and the assiatance on the research. Support from many others in this lab is also recognized and greatly appreciated.

Finally, I would to thank my family, especially my parents and wife. Their endless love and unconditional support is the power source for me to complete this research.

Reference

1. “Strain”, retrieved http://en.wikipedia.org/wiki/Deformation_(mechanics).
2. Y. J. Rao, “In-fibre Bragg grating sensors,” *Meas. Sci. Technol.* **8**(4), 355-375 (1997).
3. A. Laudati, F. Mennella, M. Giordano, et al., “A fiber-optic Bragg grating seismic sensor,” *IEEE Photonics Technol. Lett.* **19**(21-24), 1991-1993 (2007).
4. M. T. Gladwin and R. Hart, “Design parameters for borehole strain instrumentation,” *Pure Appl. Geophys.* **123**(1), 59-80 (1985).
5. K. Yamamura, O. Sano, H. Utada, et al., “Long-term observation of in situ seismic velocity and attenuation,” *Journal of Geophysical Research-Solid Earth* **108**(B6)(2003).
6. J. Berger and R. H. Lovberg, “Earth strain measurements with a laser interferometer,” *Science* **170**(3955), 296-303 (1970).
7. S. Takemoto, A. Araya, J. Akamatsu, et al., “A 100 m laser strainmeter system installed in a 1 km deep tunnel at Kamioka, Gifu, Japan,” *Journal of Geodynamics* **38**(3–5), 477-488 (2004).
8. “Capacitive Position Sensors”, retrieved http://www.capacitance-sensors.com/.
9. M. Suster, G. Jun, N. Chaimanonart, W. H. Ko, and D. J. Young, “A High-Performance MEMS Capacitive Strain Sensing System,” *Microelectromechanical Systems, Journal of* **15**(5), 1069-1077 (2006).
10. B. Culshaw and A. Kersey, “Fiber-optic sensing: A historical perspective,” *J. Lightwave Technol.* **26**(9-12), 1064-1078 (2008).
11. B. Lissak, A. Arie, and M. Tur, “Highly sensitive dynamic strain measurements by locking lasers to fiber Bragg gratings,” *Opt. Lett.* **23**(24), 1930-1932 (1998).
12. J. H. Chow, D. E. McClelland, M. B. Gray, and I. C. M. Littler, “Demonstration of a passive subpicostrain fiber strain sensor,” *Opt. Lett.* **30**(15), 1923-1925 (2005).
13. G. Gagliardi, M. Salza, P. Ferraro, and P. De Natale, “Fiber Bragg-grating strain sensor interrogation using laser radio-frequency modulation,” *Opt. Express* **13**(7), 2377-2384 (2005).

14. I. C. M. Littler, M. B. Gray, J. H. Chow, et al., "Pico-strain multiplexed fiber optic sensor array operating down to infra-sonic frequencies," *Opt. Express* **17**(13), 11077-11087 (2009).

15. G. Gagliardi, M. Salza, S. Avino, et al., "Probing the Ultimate Limit of Fiber-Optic Strain Sensing," *Science* **330**(6007), 1081-1084 (2010).

16. M. Majumder, T. K. Gangopadhyay, A. K. Chakraborty, et al., "Fibre Bragg gratings in structural health monitoring - Present status and applications," *Sens. Actuator A-Phys.* **147**(1), 150-164 (2008).

17. G. Meltz, W. W. Morey, and W. H. Glenn, "Formation of Bragg gratings in optical fibers by a transverse holographic method," *Opt. Lett.* **14**(15), 823-825 (1989).

18. B. T. M. K. T. V. Grattan, *Optical Fiber Sensor Technology* (1998), Vol. 2.

19. F. M. Haran, J. K. Rew, and P. D. Foote, "A strain-isolated fibre Bragg grating sensor for temperature compensation of fibre Bragg grating strain sensors," *Meas. Sci. Technol.* **9**(8), 1163-1166 (1998).

20. M. G. Xu, J. L. Archambault, L. Reekie, and J. P. Dakin, "Discrimination between strain and temperature effects using dual-wavelength fiber grating sensors," *Electron. Lett.* **30**(13), 1085-1087 (1994).

21. T. Allsop, L. Zhang, D. J. Webb, and I. Bennion, "Discrimination between strain and temperature effects using first and second-order diffraction from a long-period grating," *Opt. Commun.* **211**(1-6), 103-108 (2002).

22. S. K. Mondal, U. Tiwari, G. C. Poddar, et al., "Single fiber Bragg grating sensor with two sections of different diameters for longitudinal strain and temperature discrimination with enhanced strain sensitivity," *Rev. Sci. Instrum.* **80**(10), 103106 (2009).

23. Z. C. Zhuo and B. S. Ham, "A temperature-insensitive strain sensor using a fiber Bragg grating," *Opt. Fiber Technol.* **15**(5-6), 442-444 (2009).

24. O. Frazao, S. F. Silva, J. Viegas, et al., "A hybrid Fabry-Perot/Michelson interferometer sensor using a dual asymmetric core microstructured fiber," *Meas. Sci. Technol.* **21**(2), 025205 (2010).

25. A. D. Kersey, T. A. Berkoff, and W. W. Morey, "High resolution fiber-grating based strain sensor with interferometer wavelength-shift detection," *Electron. Lett.* **28**(3), 236-238 (1992).

26. A. D. Kersey, T. A. Berkoff, and W. W. Morey, "Multiplexed fiber Bragg grating strain-sensor system with a fiber Fabry-Perot wavelength filter," *Opt. Lett.* **18**(16), 1370-1372 (1993).

27. M. A. Davis and A. D. Kersey, "All-fibre Bragg grating strain-sensor demodulation technique using a wavelength division coupler," *Electron. Lett.* **30**(1), 75-77 (1994).

28. A. Arie, B. Lissak, and M. Tur, “Static fiber-Bragg grating strain sensing using frequency-locked lasers,” *J. Lightwave Technol.* **17**(10), 1849-1855 (1999).

29. Q. Liu, T. Tokunaga, and Z. He, “Realization of nano static strain sensing with fiber Bragg gratings interrogated by narrow linewidth tunable lasers,” *Opt. Express* **19**(21), 20214-20223 (2011).

30. A. Ezbiri, S. E. Kanellopoulos, and V. A. Handerek, “High resolution instrumentation system for fibre-Bragg grating aerospace sensors,” *Opt. Commun.* **150**(1-6), 43-48 (1998).

31. C. Huang, W. C. Jing, K. Liu, et al., “Demodulation of fiber Bragg grating sensor using cross-correlation algorithm,” *IEEE Photonics Technol. Lett.* **19**(9-12), 707-709 (2007).

32. Q. Liu, Z. He, T. Tokunaga, and K. Hotate, "An Ultra-high-resolution FBG Static-strain Sensor for Geophysics Applications," in *Proc. of SPIE, 4th EWOFS*, 2010), 97-100.

33. “Fibre-reinforced plastic”, retrieved http://en.wikipedia.org/wiki/Fibre-reinforced_plastic.

34. “気象庁震度階級関連解説表”, retrieved http://www.jma.go.jp/jma/kishou/know/shindo/kaisetsu.html.

35. E. D. Black, “An introduction to Pound-Drever-Hall laser frequency stabilization,” *American Journal of Physics* **69**(1), 79-87 (2001).

36. D. Chen, W. Liu, M. Jiang, and S. He, “High-Resolution Strain/Temperature Sensing System Based on a High-Finesse Fiber Cavity and Time-Domain Wavelength Demodulation,” *J. Lightwave Technol.* **27**(13), 2477-2481 (2009).

37. R. W. P. Drever, J. L. Hall, F. V. Kowalski, J. Hough, G. M. Ford, A. J. Munley, and H. Ward, “Laser Phase and Frequency Stabilization Using an Optical-Resonator,” *Appl. Phys. B-Photo* **31**(2), 97-105 (1983).

38. T. T. Y. Lam, J. H. Chow, D. A. Shaddock, et al., “High-resolution absolute frequency referenced fiber optic sensor for quasi-static strain sensing,” *Appl. Optics* **49**(21), 4029-4033 (2010).

39. “PID_controller”, retrieved http://en.wikipedia.org/wiki/PID_controller.

40. N. Takahashi, K. Yoshimura, S. Takahashi, and K. Imamura, “Characteristics of fiber Bragg grating hydrophone,” *IEICE Trans. Electron.* **E83C**(3), 275-281 (2000).

41. Y. J. Rao, X. K. Zeng, Y. Zhu, et al., “Temperature-strain discrimination sensor using a WDM chirped in-fibre Bragg grating and an extrinsic Fabry-Perot,” *Chinese Physics Letters* **18**(5), 643-645 (2001).

42. L. Talaverano, S. Abad, S. Jarabo, and M. Lopez-Amo, “Multiwavelength fiber laser sources with Bragg-grating sensor multiplexing capability,” *J. Lightwave Technol.* **19**(4), 553-558 (2001).

43. P. Childs, “An FBG sensing system utilizing both WDM and a novel harmonic division scheme,” *J. Lightwave Technol.* **23**(1), 348-354 (2005).

44. C. C. Chan, W. Jin, H. L. Ho, and M. S. Demokan, “Performance analysis of a time-division-multiplexed fiber Bragg grating sensor array by use of a tunable laser source,” *IEEE J. Sel. Top. Quantum Electron.* **6**(5), 741-749 (2000).

45. M. Zhang, C. C. Chan, D. N. Wang, et al., “Time division multiplexed strain sensing system by the use of dual-wavelength fiber Bragg gratings,” *Sens. Actuator A-Phys.* **100**(2-3), 175-179 (2002).

46. W. H. Chung, H. Y. Tam, P. K. A. Wai, and A. Khandelwal, “Time- and wavelength-division multiplexing of FBG sensors using a semiconductor optical amplifier in ring cavity configuration,” *IEEE Photonics Technol. Lett.* **17**(12), 2709-2711 (2005).

47. B. Dong, S. He, S. Hu, et al., “Time-division multiplexing fiber grating sensor with a tunable pulsed laser,” *IEEE Photonics Technol. Lett.* **18**(21-24), 2620-2622 (2006).

48. B. Lee, “Review of the present status of optical fiber sensors,” *Opt. Fiber Technol.* **9**(2), 57-79 (2003).

49. B. J. C. Schmidt, Z. Zan, L. B. Du, and A. J. Lowery, “120 Gbit/s Over 500-km Using Single-Band Polarization-Multiplexed Self-Coherent Optical OFDM,” *J. Lightwave Technol.* **28**(4), 328-335 (2010).

Publication List

A. Journal Papers

1. Q. Liu, T. Tokunaga, and Z. He, “Ultra-high-resolution large-dynamic-range optical fiber static strain sensor using Pound-Drever-Hall technique”, *Optics Letters*, 36(20), 4044-4046 (2011)
2. Q. Liu, T. Tokunaga, and Z. He, “Realization of nano static strain sensing with fiber Bragg gratings interrogated by narrow linewidth tunable lasers”, *Optics Express*, 19(21), 20214-20223 (2011)
3. Q. Liu, T. Tokunaga, and Z. He, “Sub-nano resolution static strain fiber sensor using a sideband interrogation technique”, *Optics Letters*, 37(3), 434-436 (2012)
4. Q. Liu, T. Tokunaga, *et. al*, “In situ demonstration of ultra-high staticstrain resolution FBG sensor,” *Optics Express*. (Submitted)

B. International Conferences

5. Z. He, Q. Liu, and T. Tokunaga, “Realization of nano-strain-resolution fiber optic static strain sensor for geo-science applications”, *CLEO 2012*, San Jose, May 2012. (Invited)
6. Q. Liu, Z. He, T. Tokunaga, and K. Hotate, “An Ultra-high-resolution Large-dynamic-range Fiber Optic Static Strain Sensor Using Pound-Drever-Hall Technique,” *2011 CLEO Pacific Rim Conference*, pp.130-132, Sydney, Aug. 2011. (Invited)
7. Q. Liu, Z. He, T. Tokunaga, and K. Hotate, “An Ultra-high-resolution FBG Static-strain Sensor for Geophysics Applications,” *Proc. SPIE 7653*, 76530W, Porto, Sep. 2010.
8. Q. Liu, Z. He, T. Tokunaga, and K. Hotate, “Realization of nano-order static strain resolution in FBG sensors using narrow linewidth tunable laser sources: Theoretical analysis,” *Proc. SPIE 7753*, 77537P, Ottawa, May 2011.
9. Q. Liu, Z. He, T. Tokunaga, and K. Hotate, “Resonance Difference Measurement of Fabry-Perot Interferometer with Sub-fm Resolution,” *2011 IEEE Photonics Conference*,ThEE3, Arlington, Oct. 2011.

10. Q. Liu, T. Tokunaga, *et. al*, “Field Demonstration of 10-nano Static Strain Resolution Multiplexed FBG Sensor for Geophysical Applications”, *3rd Asia-Pacific Optical Sensors Conference 2012*, APO12-143, Sydney, Jan. 2012.

11. Q. Liu, T. Tokunaga, and Z. He, “Sub-Nano Resolution Static Strain Fiber Sensor Using a Novel Sideband Interrogation Technique,” *OFC/NFOEC 2012*, Los Angeles, Mar. 2012.

C. 国内研究会

12. 劉慶文, 何祖源, 徳永朋祥, 保立和夫, “相互相関処理を用いた静的歪測定のための超高分解能 FBG センサ”, 電子情報通信学会光ファイバ応用技術研究会, OFT2009-77, 石垣島, 1 月, 2010.

13. 劉慶文, 何祖源, 徳永朋祥, 保立和夫, “波長可変狭線幅レーザを用いた超高分解能静的歪 FBG センサ”, 応用物理学会光波センシング技術研究会, LST46-27, 東京, 12 月, 2010.

14. 劉慶文, 何祖源, 徳永朋祥, 保立和夫, “波長可変狭線幅レーザを用いた地球物理研究用ナノストレーン分解能 FBG 静的歪センサ”, 応用物理学会光波センシング技術研究会, LST47-2, 東京, 6 月, 2011.

15. 劉慶文, 何祖源, 徳永朋祥, 保立和夫, “Pound-Drever-Hall 復調法を用いた超高分解能広ダイナミックレンジ光ファイバ歪センサ”, 電子情報通信学会光ファイバ応用技術研究会, OFT2011-28, 帯広, 8 月, 2011.

D. 国内大会

16. 劉慶文, 何祖源, 徳永朋祥, 保立和夫, “Analysis on the Resolution of FBG Sensors Using Narrow Linewidth Tunable Laser”, 日本光学会年次学術講演会, 10PG4, 東京, 11 月, 2010.

17. 劉慶文, 何祖源 等, “Ultra-high-resolution FBG Static-strain Sensor for Geophysics Applications,” 電子情報通信学会 2011 年総合大会, B-13-34, 3 月, 2011.

18. 劉慶文, 何祖源, 徳永朋祥, 保立和夫, “Sub-Nano Resolution Optic Fiber Static Strain Sensor Using a Novel Sideband Interrogation Technique,” 電子情報通信学会 2011 年ソサイエティ大会, B-13-16, 9 月, 2011.